Politecnico di Torino

Corso di Laurea Magistrale in Ingegneria Biomedica

A.A. 2021/2022

Sessione di Laurea Luglio 2022

Laser Surface Treatment on Titanium and Ti6Al4V Alloy Samples for Enhanced Fibroblasts Adhesion and Improved Bacteriostatic Effect

Relatrici:

Prof. Silvia Spriano

Ing. Sara Ferraris

Candidata:

Paola Soncin

Ai miei nonni Luciana, Andrea e Carolina

A mio nonno Domenico

Summary

1 Introduction

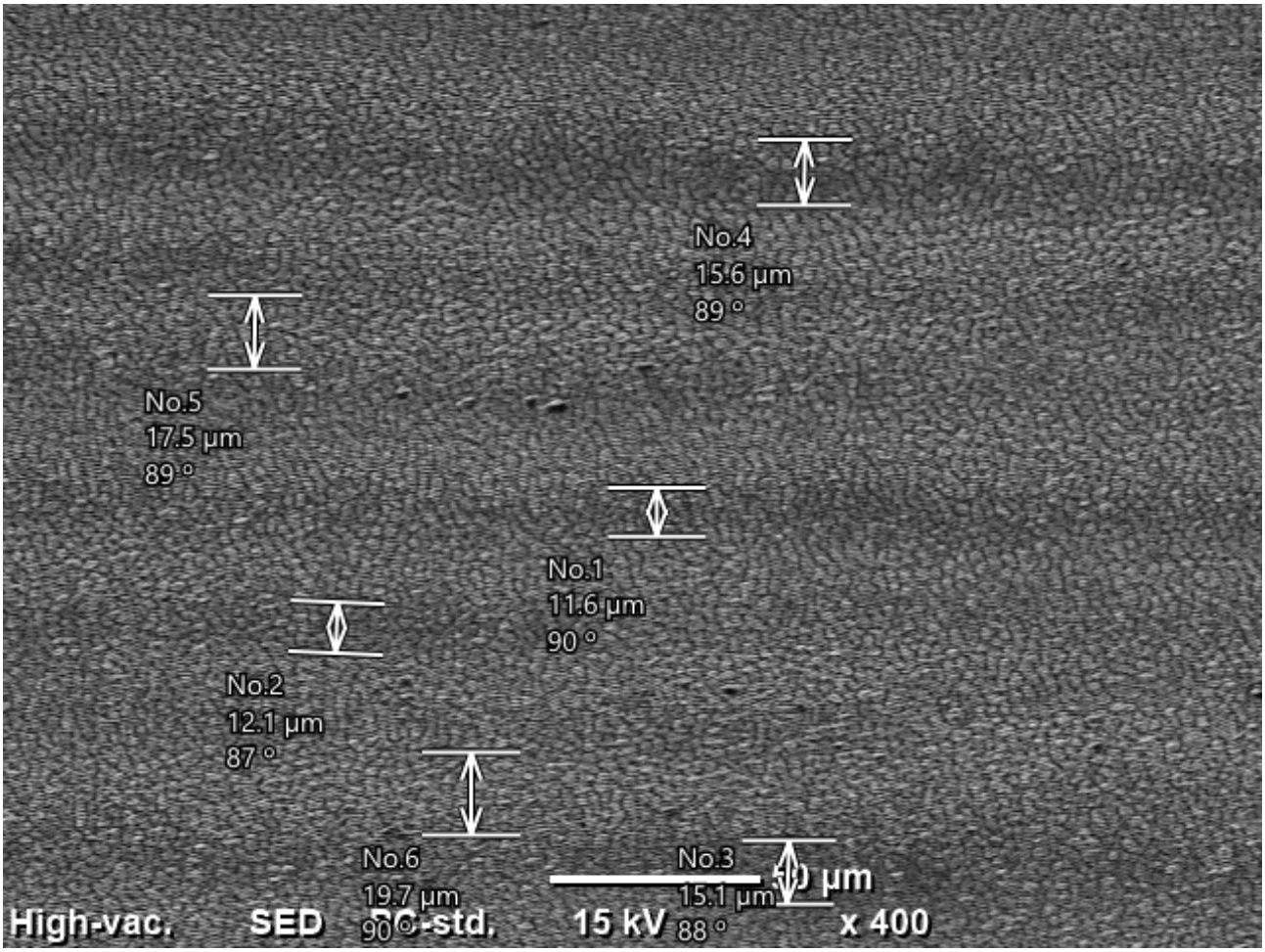

Figure 1-1. SEM image of a grade 2 pure titanium sample obtained from the treatment carried out during this thesis. Grooves are visible and the approximate widths of the grooves are shown.

A topic that is the subject of debate in recent times concerns soft tissue adhesion to titanium implants. This problem primarily involves the sector of dental implants and percutaneous devices. An interesting strategy to overcome the problem turns out to be the study of surface topography and how it affects adhesion. It is desirable that fibroblasts and cells that allow healthy tissue growth adhere properly to the surface, minimizing the implant rejection and the bacterial adhesion. Control of cells via contact guidance can help avoid problems related to encapsulation, a phenomenon in which the body reacts to an implant to encase it in a fibrous cellular growth that can lead to implant loosening and failure.

This thesis aims to study an innovative laser surface treatment carried out on the surfaces of grade 2 pure titanium and titanium alloy Ti6Al4V specimens. An example of a laser-treated specimen is shown in *Fig. 1 – 1*. The treatment should allow for proper soft tissue adhesion and is designed to be applied to the abutment area of a dental implant. This area is indeed very critical for the success of the implantation, and there are not many specific treatments on the market and in the literature for enhancing fibroblasts adhesion.

The laser treatment was carried out at *Osai Automation Systems S.p.A.* located in Parella (TO), whereas all surface characterization analyses were carried out at *Politecnico di Torino*. Biological characterizations, on the other hand, were carried out at the *Biomedical Materials Lab* of the *University of Piemonte Orientale*, located in Novara.

Since laser technology is widely used in the field of Additive Manufacturing, which is a crucial technique for producing biomedical devices such as prostheses and implants, a brief introduction to this topic was covered. Then, as several types of surface treatments are carried out to improve the properties and cell adhesion on implants, various surface modification techniques were investigated. The thesis continues with an in-depth physiology study on the behavior of cells and bacteria on implanted surfaces. Therefore, the experiment, materials, and methods used to perform the chemical, physical, and biological analyses were described, and finally, the results obtained were reported.

2 Additive Manufacturing of Titanium and Titanium Alloys

2.1 Introduction to Additive Manufacturing

Additive manufacturing (AM) is a nontraditional manufacturing process that is rapidly increasing and is being integrated into manufacturing and also our day-to-day lives. Conceptually, AM is an approach where 3D design can be built directly from a computer-aided design (CAD) file. Additive manufacturing is widely known by other terms like 3D printing or rapid prototyping (RP).

All AM technologies are defined by the ASTM F42 as processes of assembling materials to make a new object, layer upon layer following the sliced model data using a heat source (laser, electron beam, electric arc, ultrasonic energy, etc.) and feedstock (metal powder, wire or thin metal sheet, etc.).

AM methodologies are capable of creating almost any possible shape. This, coupled with the fact that 3D printing enables low waste of material, contributed to the large distribution and request of these techniques in different types of industries, including the biomedical one. 3D printing has enabled the fabrication of biomaterials and advanced biological tissues for all biomedical applications. This branch of additive manufacturing is called "bioprinting" and has the added advantage of being able to manufacture low-volume parts, critical implants, and custom-made organs and tissues. [14] The bioprinting process begins with the image acquisition of the interested organ or tissues through imaging techniques such as magnetic resonance imaging (MRI), computed tomography (CT), X-ray, or ultrasound. The next stage is image processing, where the image is segmented with a mesh and a CAD 3D model is developed. The successive phase is the printing, and it depends on the type of the printer, the material, and the technology used.

According to the ASTM F2792-12a, there are 7 categories of AM technologies: binder jetting, directed energy deposition (DED), material extrusion, material jetting, powder bed fusion (PBF), sheet lamination, and vat polymerization. [2] In this thesis, I'll focus on DED, PBF, and, to a lesser extent, sheet lamination because those are the ones involving titanium and its alloys.

The *workhorse* of titanium alloys is Ti6Al4V alloy, also known as Ti64, which is an $\alpha + \beta$ titanium alloy with an excellent combination of mechanical properties, superior biocompatibility compared to other alloys, and outstanding corrosion behavior. In the last half a century, Ti64 is increasing its application field in the biomedical industry: it can be used for implants and bridges owing to its biocompatibility, high corrosion resistance, and strength. The main boundary of Ti6Al4V is related to a challenging production due to its chemical reactivity to oxygen and nitrogen, the low thermal conductivity, and the tendency to strain hardening, which causes greater fragility. As mentioned before, another issue of the traditional manufacturing methods is a large amount of material waste, high manufacturing cost, and long lead time. [4]

AM processes include a wide range of technologies, among which stand out those based on metal powder melting such as Directed Energy Deposition, Selective Laser Melting, and Electron Beam Melting. In these processes, a laser or electron source heats the feedstock, producing a melt pool. Consequently, rapid melting and resolidification take place.

In this chapter, I will describe AM techniques, raw materials, and mechanical characteristics of titanium and titanium alloy Ti6Al4V products obtained by additive manufacturing, to understand if these non-traditional technologies can take the place of the traditional ones, especially in the biomedical field. It is important to consider many properties to evaluate the quality of the manufacture, among which of primary importance there is the response of the organism to the implanted organ or tissue.

Research in this field is constantly developing to improve the quality of human life.

2.2 Raw Materials for Additive Manufacturing of Titanium

Most additive manufacturing technologies use powder as the main starting material, but there are few exceptions, such as DED methods which can use both metal wire and powder, and Ultrasonic Additive Manufacturing (UAM) which exploits the melting of metal sheets.

The successful use of titanium powder in AM technologies is related to accurate control of the feedstock production process. In this discussion, greater emphasis will be placed on the powder characteristics and its application in AM.

2.2.1 Powder Characteristics

The final product is influenced by the quality of the powder, not only for the one that is added layer-by-layer but also for the one reused from the previous AM cycle.

The better shape of the powder grains which ensures great mechanical properties is the spherical one, but also the convex and the star-like shape. The last one has weaker performance compared to the others. The excellent flowability is a highly sought-after feature that is closely related to the performance of the powder, which, to meet this requirement, needs to have a spherical shape and reasonably large size. However, it must be considered that the grains' shape and dimension can alter after repeated use in AM build cycles due to the partial melting of the particles, and this is the reason why reused particles should pass through an 80 μm sieve. [5] Furthermore, the powder could undergo chemical-physical changes because of numerous AM cycles.

Of whatever morphology the powder is, close control of the production and proper handling of the powder are necessary to have a successful use in metal AM. Key factors related to powder feedstock that influence the quality of AM products include the powder morphology, the size, and size distribution, which should be as regular as possible. Finer powder, with a more uniform size distribution, lead to a more homogeneous melt pool, but they require more expensive methods, due to the challenging atomization of the feedstock. Depending on the AM process, powder grains have a minimum size, which is also related to the smallest buildable feature size and surface finish. PBF method allows the manufacture of 15-45 μm powder particles, whereas EBM and DED methods make use of larger particles (about 50-150 μm). [9]
It is also crucial to consider the chemical composition of the titanium particles since the level of oxygen is strictly imposed under 0.2 wt.%. [15] The low oxygen content is inversely proportional to particle size.

Other significant powder features that must be considered are the powder density – depending on the powder composition methods and the gas used, particles may have porosities, which result in porosities in the 3D-printed metal products – powder contamination, and environment condition.

As noted earlier, the spherical shape is the most preferred one for metal additive manufacturing today and a few processing methods will be briefly illustrated below.

The typical spherical powder production method is gas atomization (GA), which provides that the feedstock is melted in a closed furnace under air or inert gas blanket, or under a vacuum (*Fig. 2 – 1 a*). The molten metal is then fed through a delivery nozzle, in which the liquid metal is subjected to a high-speed air – N2, He, or Ar gas – that impacts the flowing melt and breaks it up into small droplets. However, currently, several atomizers are based on the principle of gravity rather than forced gas feed [9]. The finer spherical powder can be gained through GA, with a narrower size distribution compared to other techniques. [15] The main issues regarding GA include the difficulty in avoiding the satellite formation and the possibility that argon remains trapped in the particles.

Other methods to obtain spherical grains are plasma atomization (PA) (*Fig. 2 – 1 c*) and plasma rotating electrode process (PREP) (*Fig. 2 – 1 b*).

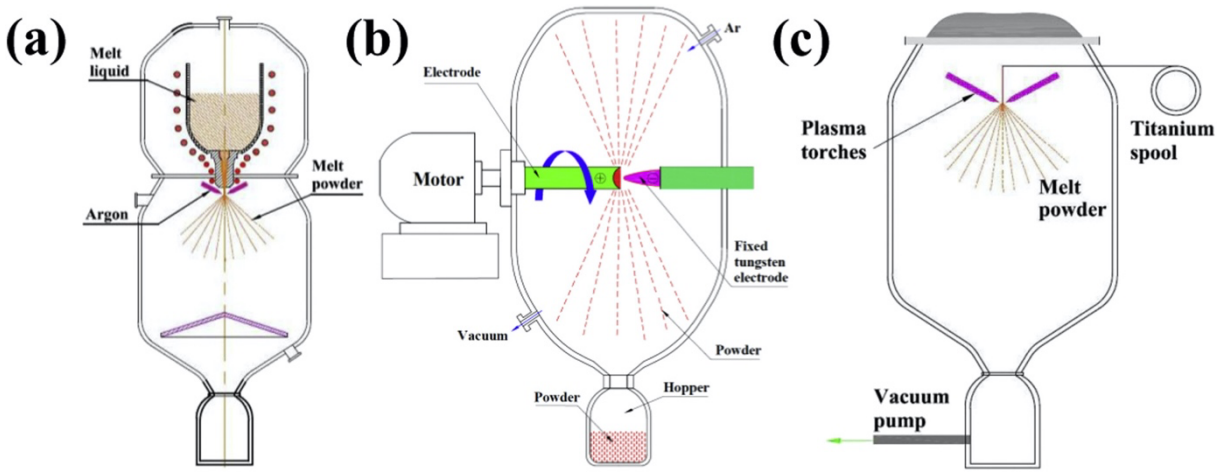

Figure 2-1 Schematic representation of the atomizing processes (a) GA, (b) PREP, (c) PA. [16]

The high cost associated with the manufacture of spherical metal powders is the major barrier to the successful commercialization of metal AM. Oh the other hand, the powder characteristics are essential to product quality parts through metal AM. Therefore, several low-cost techniques are becoming of interest: these allow to obtain an angular-shaped powder that can be used raw or subsequently processed to a spherical morphology.

2.3 Additive Manufacturing Technology

As mentioned before, there are three main categories of Additive Manufacturing used for processing titanium and its alloys: DED, PBF, and sheet lamination. Under each category, there are several technologies branded by different manufacturing companies. [3]

2.3.1 Powder Bed Fusion

The basis of powder bed fusion techniques consists of a layer-by-layer melting of the powder bed area following the geometry provided by the CAD data. A thick metal powder laying on the built platform, which is generally composed of the same material as the powder, is melted or sintered by the heat source (laser or electron beam) following the path; consequently, a process of solidification and bonding occurs during the cooling phase. The build platform then moves down in the z-direction equal to the thickness of a layer, and the process is repeated. As the heat source is enough to penetrate deeper than the thickness of a single layer, each layer becomes welded to the previous, ensuring a dense component at completion. [12]

The chamber is typically heated to keep up the powder just below the melting temperature.

There are four powder bed fusion mechanisms: solid-state sintering, chemically induced sintering, partial melting, and full melting. Full melting is the method commonly used for metals: it has an excellent bonding since the laser heats the particles all the way through and past the current printed layers.

The main steps of PBF are [3]:

- A substrate is placed on the build platform.
- It is generated an inert atmosphere inside the chamber if the heat energy source is a laser, whereas the electron beam operates under high vacuum conditions.
- A thin layer of metal powder (20-200 μm) is positioned and smoothed on the substrate.
- The bed powder is scanned by an energy source, following the geometry provided by the CAD file.
- As shown in *Fig. 2 – 2*, the process is repeated with the next layer until the final 3D object is printed.

The ability to produce complex geometries with high-resolution internal porosities is the greater advantage of PBF processes. On the other hand, it is still challenging to shift the processed material and obtain a higher build envelope. [5] Other limitations related to PBF technology include the difficulties in repairing damaged pieces and the hard use of multiple materials.

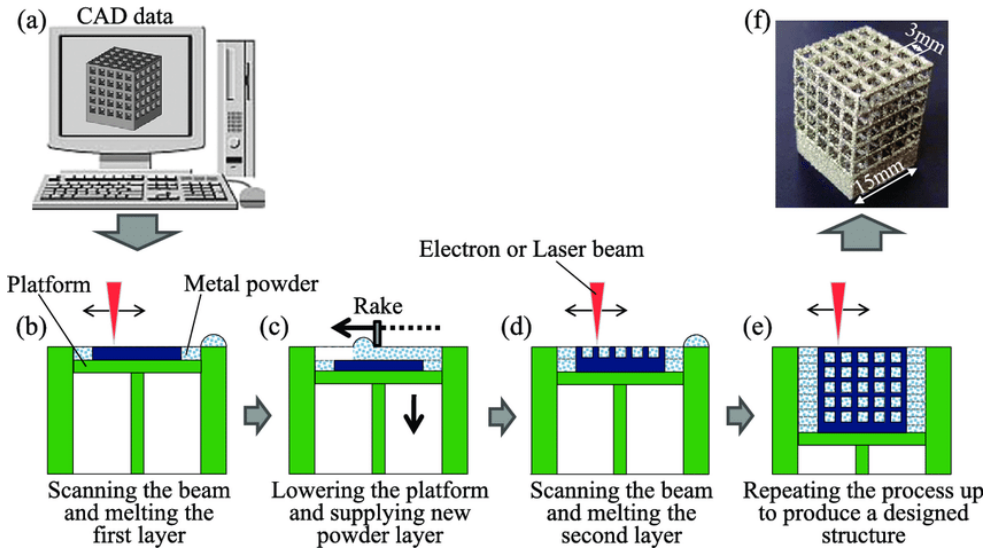

Figure 2-2. Schematic diagram showing powder bed fusion (PBF) technology, used in fabricating a metal lattice structure. [13]

There are two main technologies based on the fusion of a thick powder layer, layer-by-layer: selective laser melting and electron beam melting, which differ in the energy source (laser or electron beam).

2.3.1.1 Selective Laser Melting

The SLM process is characterized by having a colder powder bed compared to EBM and a high power-density laser as the energy source, which melts and fuses metal powder under an inert chamber, usually filled with an inert gas like N_2 or Ar, depending on the reactivity of the metal powder to be used. The parts fabricated by SLM tend to show improved mechanical, tribological, and corrosion properties compared to their cast counterparts [17]. In addition, through SLM building organized geometries with complex internal features and passages is possible.

The powder is heated at 250°C to better manage thermal gradients and lessen the adverse effects of thermal stresses. The cooling rate is very high, varying between 10^4 - 10^6 K/s [5],[17]. SLM can be used for a broad assortment of metallic alloys. It is regarded as the most versatile AM process, because it can process several materials including alloys based on Al, Ti, Fe, Ni, Co, and their composites [17].

2.3.1.2 Electron Beam Melting

An electron beam is used as the energy source in EBM, and this technology operates under a vacuum and generally with a hot powder bed (the powder is heated to a temperature higher than 600°C [5], [17]). Under such conditions, the solidification cracking phenomenon can be decreased. The high-vacuum environment provides an optimal contamination-free area for processing those materials that react easily with oxygen and nitrogen, such as Ti6Al4V. [4]

Only limited metals are employed in EBM [17], such as Ti grade 2, Ti6Al4V, Inconel 718, and CoCrMo.

2.3.2 Directed Energy Deposition

The main difference between the DED process compared to PBF is that the first produces 3D objects using material injection into the melt pool from nozzles instead of scanning on a powder bed. The metal material (powder or wire) is melted through a concentrated heat source (laser or electron beam) and, in the meanwhile, it is deposited on a substrate.

DED methods have a larger application window since a high degree of control and process capability is possible. The ability to repair or modify already existing items with a minimum waste, the capability to increase deposition rate, and the production of objects with a higher degree of freedom in design and geometry as it can process simultaneously different materials, are just a few of the benefits DED methods can offer. [5]

On the other hand, the fabrication of finer geometries is extremely restricted: DED techniques are limited to a fairly coarse resolution since the design rules are constrained by the nozzle diameter, ranging from 1-3 mm.

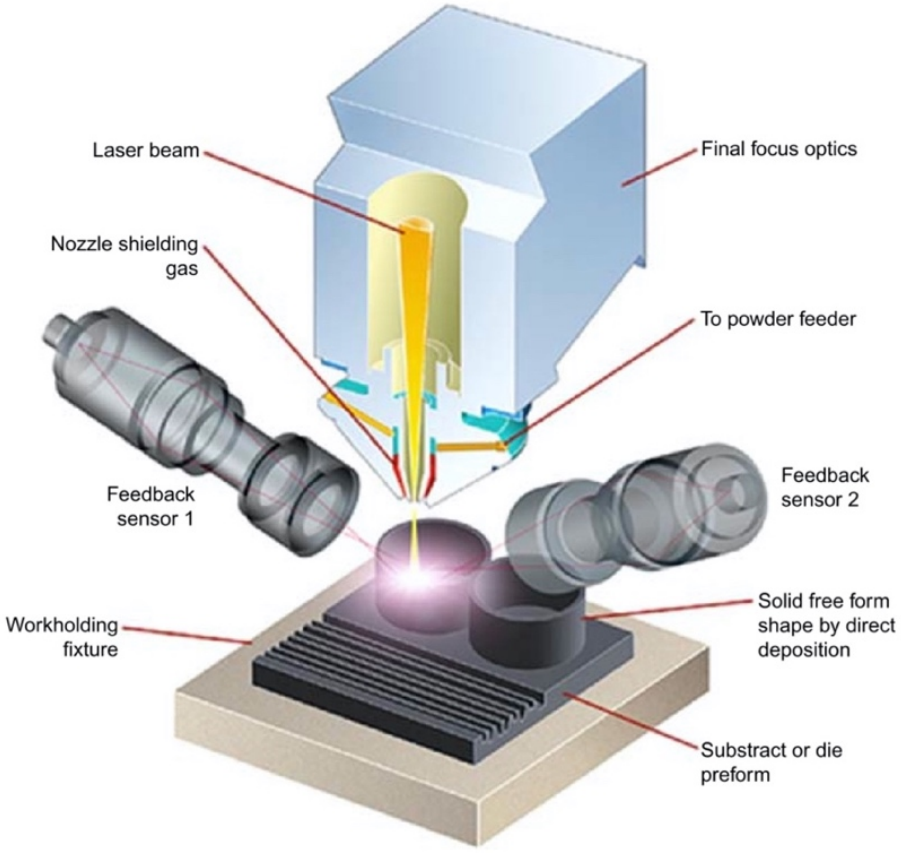

Figure 2-3 Schematic showing direct metal deposition technology. [8]

The process steps for DED are:

- A substrate is located on the worktable.
- If the energy source is a laser, the machine chamber is closed and filled with inert gas, whereas if an electron beam processing is used, the machine chamber is evacuated to reduce the oxygen level to the desired level.

- The feedstock comes out from the nozzle, and it's immediately melted by the laser beam or electron beam. The nozzle moves at a constant speed, following the toolpath provided by the CAD file.
- A melt pool is generated. As the nozzle moves away, the melt pool solidifies forming a layer of metal.
- Successive layers follow the same principle and build up the part layer by layer until competition.

2.3.3 Sheet lamination

The main technology under the sheet lamination category is Ultrasonic Additive Manufacturing (UAM). This method implies the use of ultrasound radiation to weld a succession of metal tapes into a 3D shape. Typically, the ultrasonic frequency is about 20 kHz.

The UAM process described in *Fig. 2 – 4* involves building up solid metal objects through ultrasonic welding of a succession of metal tapes into a three-dimensional shape, with periodic machining operations to create the detailed features of the resultant object. [8]

During the build, periodic machining operations add features to the part, such as removing excess material. [3] The rolling ultrasonic welding system is comprised of an ultrasonic transducer, a booster, a welding horn, and a "dummy" booster. [8].

The transducer emits vibrations in the ultrasound frequency, which are transmitted, through the booster, to the disk-shaped welding horn. A solid weld is formed between the thin metal tape and the base plate. The 3D object is manufactured by the welding consecutive tapes: first a tape alongside the other, then one over the other.

The possibility of using multiple materials in different layers is the main benefit related to UAM technology. By contrast, this method admits the usage of just a few materials with lower melting points and has a limited overhang capability.

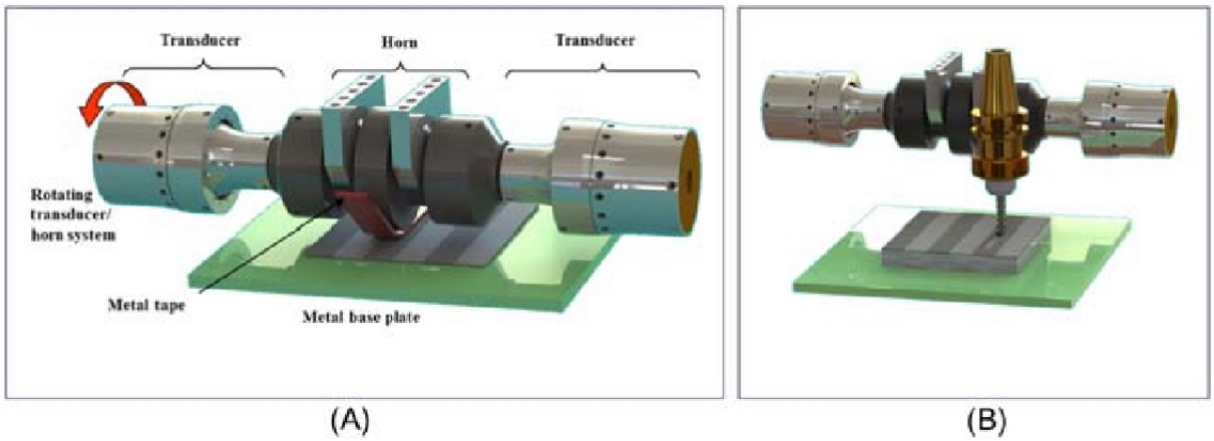

Figure 2-4. Ultrasonic additive manufacturing (UAM) technology: (A) ultrasonic welding of aluminum and titanium tape; (B) periodic machining operations. [8]

2.4 AM challenges

2.4.1 Current state of AM

The origin of Additive Manufacturing and 3-D printing technology comes from rapid prototyping, which rapidly developed in the early 1980s, allowing for the first time the manufacturing of complex geometries, ensuring the maintenance of structural properties.

Nowadays, AM methods have reached such technological success that they can be applied in various fields, manufacturing a large number of materials, and they have even been defined as the third industrial revolution by *The Economist*. [7]

The main technology which deals the metal manufacturing used worldwide is Powder Bed Fusion, however, it is estimated that during the next decade other methods such as DED and sheet lamination techniques will soar in the AM market.

The modeling phase, which precedes the layers manufacturing, is of paramount importance in AM, as it shapes the product geometry. Since the equipment and the experiments are costly, further unsuccessful attempts must not be made, so it is required a priori knowledge about modeling. Empiric modeling techniques become a key issue in this field, which are based on different potential computational intelligence methods, including artificial neural networks, fuzzy logic, and genetic programs, to name but a few.
AM engineering has two main possibilities to start: the virtual model or the physical model. [6] The virtual model is created by CAD software, and it can be a surface or a solid model, whereas the data acquisition to obtain the physical one requires a struggling method called *reverse engineering*: 3D data is generated by making a series of measurements and reducing that information into a 3D model of some nature. The model is then reproduced thanks to computer-aided design software. [10]

2.4.2 Application in the Biomedical Industry

Figure 2-5. Example examples of applications in orthopedics produced through additive manufacturing. [18]

Additive Manufacturing has opened the doors to a new concept of medical implant based on an improved and custom-made model, allowing the design of patient-matching implants for specific problems, as *Fig. 2 – 5* shows. Prosthetic, orthopedic, and dental industries are the earliest medical fields in which AM technologies have found a successful application space, [6], especially concerning metal AM technologies.

The model, whether it is dental or bone, is generated from a medical imaging technology (CT exam, magnetic resonance, echography, intraoral scanning, intraoral impression, etc.) and then processed through a computer-aided design (CAD) software.

AM titanium implants submit an engineered tridimensional structure with porosities and holes, which are aimed at mimicking the trabecular structure of the natural bone. This can result in a stiffness decrease of the design to better match the mechanical properties and promote bone ingrowth. Furthermore, the protective and stable oxides on the titanium surface act in parallel with the porous structure providing osseointegration, which is essential for the success of the implant. [11] AM Ti6Al4V implants guarantee other properties that should not be underestimated such as high strength, durability, and relatively low density. In addition, AM methods became of key importance since they allow the production of a patient-specific custom product in a relatively short time. However, the most serious complication that can occur downstream of an implant is a bacterial infection, which can take place immediately upon the surgery or after years. As a consequence, implant surface functionalization can represent an effective strategy to decrease the risk of infection, improving the body's response. The next chapter will deal with surface treatments that are performed on titanium and Ti6Al4V alloy implants and that improve the properties of the material.

2.4.3 Advantages and Disadvantages

The greater advantage of AM technology is the cost-efficient short-run production. Thanks to these unconventional methods, almost total design freedom became possible, which has a crucial implication for the biomedical industry: the possibility of easily customizing implantable objects.

Additive Manufacturing and 3-D printing ensure a machine and waste products reduction, giving the possibility of repair, reconfiguration, and remanufacturing.

The mechanical properties following an AM process may, however, decrease. For instance, porous titanium structures manufactured by EBM [19] are light and have isotropic mechanical properties, which makes them ideal for biomedical applications. Bone tissue can in grow into porosity and osseointegrate to the material surface. Porous titanium can be easily produced via AM and presents an acicular microstructure, which consists mainly of α' martensite and a small amount of β phase. This microstructure leads to structures that are normally more brittle than their solid bulk [19]. However, such disadvantages can be removed by heat treatments.

On the other hand, AM methods are still in a development phase since it is a relatively recent technology. The main drawbacks are related to limited scalability, including a restricted choice of material. In addition, the high cost associated with the manufacture of powders is one of the major barriers to the successful commercialization of metal AM.

However, researchers and industries are daily committed to solving these limitations and improving the process and the quality of the product object.

2.4.4 Future trends

Among the major future developments, there are the design of specialized lattice structures able to promote osseointegration and avoid stress shielding effects, and the manufacturing of multiple materials implants, which can lead to functionalized superficial coating capable of counteracting inflammatory effects and increasing biocompatibility. Moreover, the progression of additive and subtractive manufacturing processes is still an issue, as well as the improvement of new metal alloys.

Research concerning titanium and its alloys deals with preventing potentially toxic elements, such as Vanadium and Aluminum. Furthermore, the achievements of the best mechanical requirement, i.e., a balance between strength and ductility while maintaining an elastic stiffness comparable to that of a human bone, and a longer fatigue limit of AM processed metals are still under study. To achieve a lower stiffness, beta alloys are considered. [11]

References

[1] Bandyopadhyay A., Bose S. "Introduction to Additive Manufacturing." *Additive Manufacturing, Second Edition*. CRC Press, 2020.

[2] Dutta B., Froes F.H. "The Additive Manufacturing of Titanium Alloys." Additive Manufacturing of Titanium Alloys, State of the Art, Challenges, and Opportunities. Elsevier, 2016.

[3] Dutta B., Froes F.H. "Additive Manufacturing Technology." Additive Manufacturing of Titanium Alloys, State of the Art, Challenges, and Opportunities. Elsevier, 2016.

[4] Liu S., Shin Y.C. "Additive manufacturing of Ti6Al4V: A review." *Elsevier Ltd Materials and Design*. Vol.164, 2019, 107552.

[5] Bandyopadhyay A., Bose S. "Additive Manufacturing of Metals Using Powder Bed-Based Technologies." *Additive Manufacturing, Second Edition*. CRC Press, 2020.

[6] Badiru A.B., Valencia V., Liu D. "Additive Manufacturing Technologies: State of the Art and Trends." *Additive Manufacturing Handbook – Product Development for the Defense Industry*. CRC Press, 2017.

[7] Markillie P. *A third industrial revolution*, The Economist April 21st, 2012, https://www.economist.com/special-report/2012/04/21/a-third-industrial-revolution, accessed on 15th April 2021.

[8] Dutta B., Babu S., Jared B. "Additive Manufacturing Technology." *Science, Technology and Applications of Metals in Additive Manufacturing*. Elsevier Science & Technology, 2019.

[9] Dutta B., Babu S., Jared B. "Raw Materials for Metal Additive Manufacturing." *Science, Technology and Applications of Metals in Additive Manufacturing*. Elsevier Science & Technology, 2019.

[10] Macy B. "Reverse Engineering for Additive Manufacturing." *Handbook of Manufacturing Engineering and Technology*. Springer, 2015

[11] Zang J., Jung Y.G. "Additively Manufactured Metals for Medical Applications." *Additive manufacturing: Materials, Processes, Quantifications and Applications*. Butterworth-Heinemann, 2018.

[12] Zang J., Jung Y.G. "Additive Manufacturing of Metallic Materials." A*dditive manufacturing: Materials, Processes, Quantification and Applications*. Butterworth-Heinemann, 2018.

[13] Nakano T., Ishimoto T. "Powder-based Additive Manufacturing for Development of Tailor-made Implants for Orthopedic Applications." *KONA Powder and Particle Journal.* Vol. 32, 2015, p. 75-84.

[14] Kalaskar D.M. "Introduction to 3D Printing in Medicine." *3D Printing in Medicine.* Woodhead Publishing, 2017.

[15] Sun P., Fang Z.Z., Xia Y., Zhang Y., Zhou C. "A novel method for production of spherical Ti-6Al-4V powder for additive manufacturing." *Powder Technology*. Vol. 301, 2016 p. 331-335

[16] Chen G., Zhao S.Y., Tan P., Wang J., Xiang C.S. Tang H.P. "A comparative study of Ti-6Al-4V powders for additive manufacturing by gas atomization, plasma rotating electrode process and plasma atomization." *Powder Technology*. Vol. 333, 2018, p. 38-46.

[17] Gokuldoss P.K., Kolla S. Eckert J. "Additive Manufacturing Processes: Selective Laser Melting, Electron Beam Melting and Binder Jetting-Selection Guidelines." *Materials*. Vol. 10(6), 2017, p. 672.

[18] https://www.lincotekmedical.com/products-services/additive-manufacturing/, accessed on: 23th May 2022.
[19] Zhang L.C., Liu Y., Li S. Hao Y. "Additive Manufacturing of Titanium Alloys by Electron Beam Melting: A Review." *Advanced Engineering Materials Journal*. Vol. 20, 2018, 1700842.

3 Surface Modification of Titanium and Titanium Alloys

The structural and functional integration of the surface of the implant with the surrounding environment is crucial for the long-term success of the device. Collectively with the physical and chemical aspects, surface roughness determines the biological properties of the material. Within seconds of implantation, biological environments interact with the biomaterial surface, and this interaction is inevitably affected by chemical composition, surface energy, roughness, and topography. These parameters play a role during implant integration, therefore for osteointegration.

The amount of bone-to-implant contact (BIC) is a crucial factor in the long-term success of an implant. BIC must be maximized by extending the area of contact through the optimization of surface roughness. [1] As a consequence, roughness is closely related to bone anchorage and biomechanical stability.

The main challenge in implantology is the design of biomaterials that actively promotes a faster and more improved cells-adhesion process while avoiding undesirable tissue response, looking for a surface with controlled and standardized topographies. The superficial topography has a relevant effect on the morphology of the cells, as long as it impacts the cell orientation, behavior, and activity.

Fibroblasts, along with Mesenchymal stem/stromal cells (MSCs), intervene in conditions of inflammation and stress, sending signals that help the surrounding tissue to adapt. They play a key role in providing the majority of the structural framework of almost all types of tissues, as fibroblasts secrete extracellular matrix molecules [29]. It is particularly important to ensure that fibroblasts can change their shape on the implant surface by elongating themselves and growing extensions, an aspect that is responsible for creating a proper gingival attachment between soft tissue and titanium implant surface [30] in the case of periodontal implantation.

Structural modifications of the implant surface, especially at the nanoscale level, induce the modulation of osteoblasts' adhesion and spreading, phenomena particularly related to the enhancement of bone formation at the bone-implant interface. [4]

It is indeed recognized that interactions between the biomaterial and human tissue occur at the nanoscale and are controlled by nanoscale properties.

In this chapter I'll focus on specific surface treatment for titanium and its alloys, since implant topography needs to be improved to optimize the cell adhesion on the surface, lower the bacterial attack and ensure long-term implant success.

3.1 Common methods for Topography Modification

The application of standard methods for topography modification to titanium implants deals with many different arrangements. For instance, surface topographies could assume an organized and isotropic pattern or an unorganized and anisotropic pattern. The latter type of topography is produced when applying common treatments for surface modification such as plasma spraying, anodization, blasting, and acid etching.

3.1.1 Titanium Plasma Spraying

The Titanium Plasma Spraying (TPS) technique consists of injecting titanium powders into a plasma torch at a high temperature, then the titanium particles are projected onto the target implant surface, where they condense and fuse, forming a film of variable thickness around several tens of µm. The titanium particle layer obtained by Lee et al. [31] on a Ti6Al4V alloy surface was about 150 µm thick for preventing the elution of toxic element (Al, V) ions in the human body. However, it is possible to achieve lower film thicknesses of around 40 – 50 µm [2], but even higher of about 300-500 µm if the desired final roughness is very high [3].

The resulting surface after the TPS treatment is very porous, with a porosity average percentage between 15 – 35 % [3], [32], [33].

The literature shows that the range of roughness R_a of titanium plasma spray-coated surfaces is very wide. Some studies [2] demonstrate lower roughness of about 7 µm, whereas others highlight roughness between 18 – 60 µm [3],[33], but it is possible to observe maximum height roughness R_z of 145.3 ± 22.9 µm, which evidences sharp level jumps alternating with smoother surface sections [33].

Due to the high affinity of titanium to oxygen, a thin layer of TiO_2 (5-10 nm) is formed immediately on its surface when exposed to the air and gives it a passive character [33].

In a preclinical study on pigs, the bone-to-implant interface with a TPS surface is formed much faster than smooth-surface implants, since an increase in the tensile strength was observed [2].

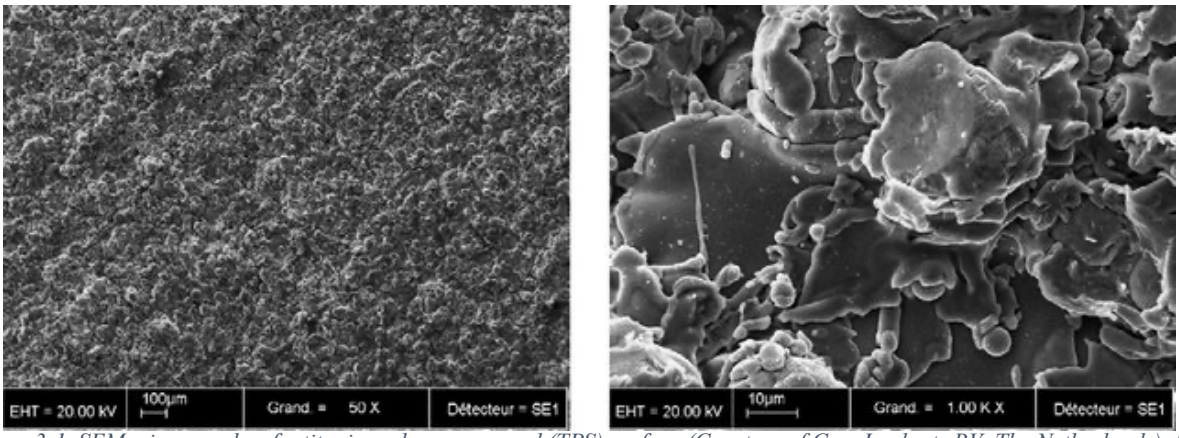

Figure 3-1. SEM micrographs of a titanium plasma-sprayed (TPS) surface (Courtesy of Cam Implants BV, The Netherlands). [2]

However, the metal ions release could be a source of concern, together with the fact that such high roughness doesn't have too many clinical advantages since there are greater advantages in using more moderate roughness and as shown in *Fig. 3 – 1* the roughness hasn't a reproducible pattern. The bone-implant contact percentage is lower in a TPS implant rather than in a hydroxyapatite plasma-sprayed coated implant, which represents a good bioresorbable substitute to titanium powder. Despite that, *in vivo* studies [19] showed that TPS implants exhibit comparable pull-out strength compared to the hydroxyapatite-coated implants because of the weak coating-substrate interface.

TPS coating is still a widely used technology in the orthopedic field since, when considering the prepared samples for bone augmentations particularly loaded in compression, plasma spraying provided desirable properties [33].

3.1.2 Grit Blasting

The technique behind this method is based on particles that collide on the surface through a high-speed nozzle. This generates a rough layer but does not produce pores.

The possible materials used are different: usually, they consist of hard ceramic particles, and they must be biocompatible, osteoconductive, and resorbable. Materials include ceramic, alumina, titanium oxide, CaP, and apatite powder. The size and granulometry of particles determine respectively the surface roughness and the thickness of the layer. [1]

The range of roughness, between 4 and 10 μm [34], has a close correlation with grit blasting conditions such as the distance of the nozzle from the surface, the blasting pressure, angle, and time of exposure.

We now have evidence [10] of the fact that grit-blasted implants with titania (TiO_2) or alumina (Al_2O_3) particles have an altered topography which resulted in an enhancement of bone formation at the interface and an increase of biomechanical properties measured with a torque device.

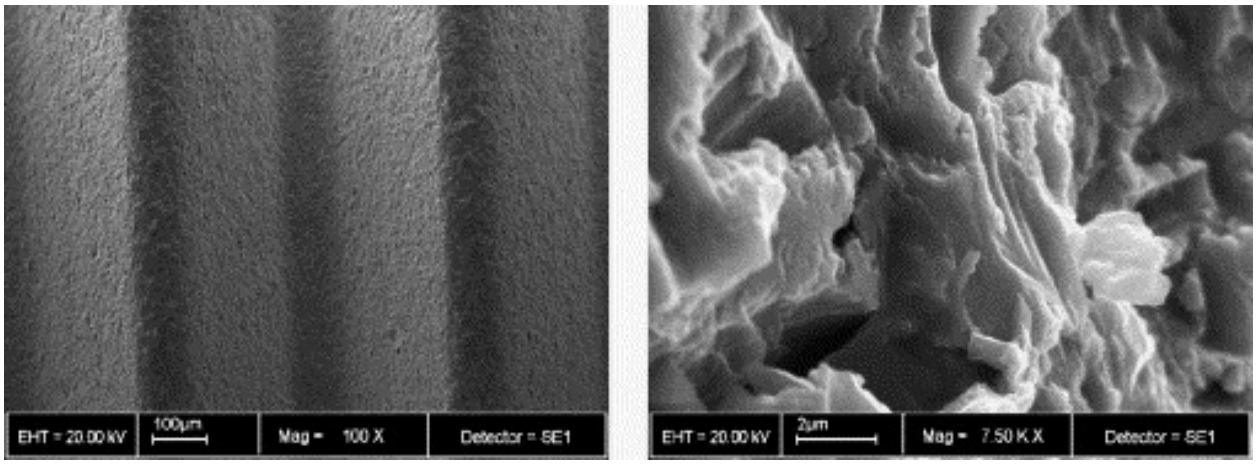

Figure 3-2. SEM micrographs of a TiO_2 blasted surface (Courtesy of Astratech TiOblast™, France). [2]

The most used material for blasting titanium surfaces is alumina Al_2O_3, also because it allows to easily adjust the levels of roughness by changing the grain size. Alumina blasting creates randomized surface textures, increasing the surface area. However, this method can give rise to the development of random bone cell orientations that may contribute to scarring tissue formation [6]. In addition, the main problem concerning alumina blasting is related to residual particles on the surface which persist on the surface despite ultrasonic washing, acid passivation, and sterilization and can cause inflammatory reactions. Titania, zirconia, and hydroxyapatite are often used to prevent this phenomenon.

As shown in *Fig. 3 – 2*, with this technique more reproducible patterns are realizable at the microscale, but an ordered structure at the nanoscale is not observed. However, random roughnesses are designed for bone contact as osteoblasts are roughophilic. The grit blasted rough surface has indeed been demonstrated to stimulate osteoblast adhesion, therefore enhancing osteointegration. Despite an associated inflammatory response observed, the overall success rate of this technique is satisfactory [11].

3.1.3 Acid Etching

The etching process involves selectively dissolving away metal using an oxidizing reagent. Strong acids such as HCl, H_2SO_4, HNO_3, and HF are used in this chemical modification technique, which leads to the growth of thin grids of nanopits with a diameter between 0.5-2 µm [2], [35] as displayed in *Fig. 3 – 3*. Acids can be used singly or in mixed solutions.

The coarse surface was characterized by its peaks and valleys-like structure, but several flat facets could be observed. The facets also had small irregularities such as pits and stripes [35].

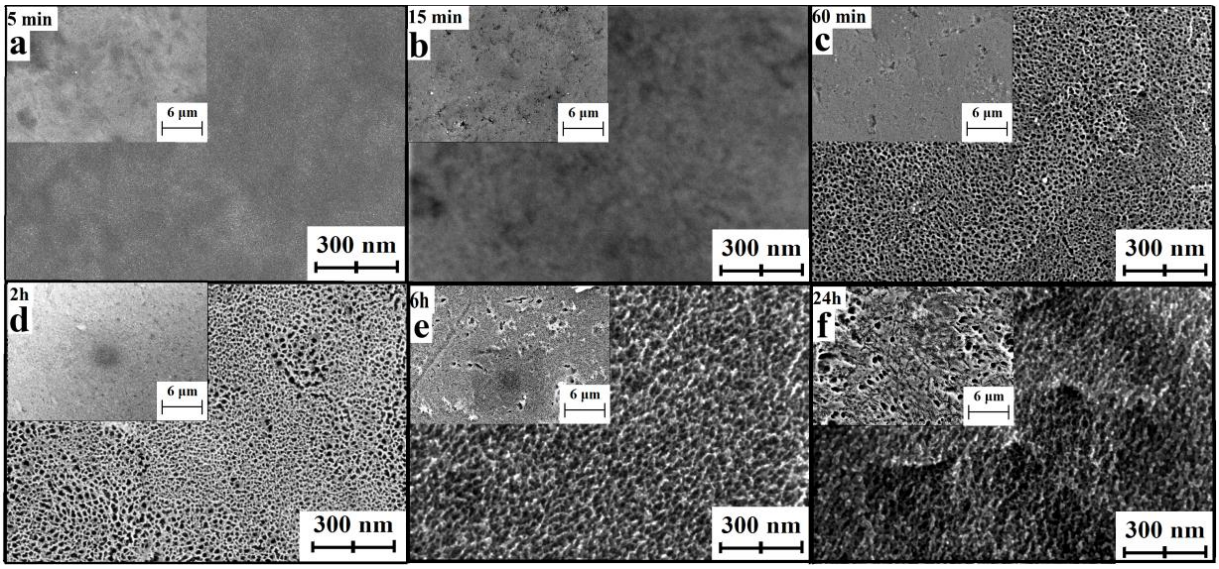

Figure 3-3. Characteristic SEM images of titanium etched in H2SO4/H2O2 solutions for a) 5 minutes; b) 15 minutes; c) 1 hour; d) 2 hours; e) 6 hours and f) 24 hours (magnification 200000x and 10000x) [36].

Roughness strictly depends on the type of acid used and on the etching time and results between 0.5 – 80 nm [35], [36]. Changing etching parameters such as the composition, exposition time and temperature can modify the topography, the surface wettability, and the thickness of the oxide.

The etched surface shows traces of elements depending on the acid or mixture of acids used. Peaks of phosphorus were observed in addition to the peaks of titanium by Zareidoost et al. [35] through EDS for the samples treated with mixed solutions, in which no fluorine was detected. On the other hand, on samples treated with HF were observed traces of fluorine. Since titanium is reactive to fluoride, it can be treated in a fluoride solution as an alternative to dual acid etching, causing the formation of TiF_4 species. There is an improvement in osteoblastic differentiation related to topography and the incorporation of fluorides. Other advantages in comparison with control samples are greater push-out forces and a higher torque removal [2].

A microroughness surface is formed which allows for accelerating and improving the osteoconductive process through the attachment of fibrin and osteogenic cells. Fibrin fibers adhere properly to the surface, therefore contact guidance for osteoblasts is generated. This process produces the generation of a better bone-implant contact. Acid etching enhances osteointegration and it has been demonstrated long-term success of acid-etched implants.

A long-term follow-up clinical study [20] showed that acid-etched dental implants demonstrate good treatment outcomes in terms of prosthetics survival and marginal bone loss. Several types of prosthodontics were acid-etched treated and subsequently evaluated, among which single crown, fixed bridge, overdenture, and fixed full-arch. The more frequent complications seem to be technical prosthetic problems and periimplantitis. However, acid-etched titanium can be a very prominent material for dental and orthopedic implants due to its well-developed surface and the presence of hierarchal micro/nanostructures on the surface [36].

3.1.4 Anodic oxidation

Anodization is one of the most common techniques used to create nanostructures with a diameter of less than 100 nm [11], [37], as illustrated in *Fig. 3 – 4*. The titanium substrate represents the anode, connected by copper wires to the cathode, consisting of an inert platinum sheet. Between anode and cathode, a 30 Volts or 3 Amperes power supply is linked through a positive and negative port. The anode and cathode are kept separated and they are submerged in an electrolyte.

Electrolyte reactions lead to the formation of an oxide film on the anode surface. The anodized metal presents a porous surface, with a porosity of 10 – 100 nm. If a high voltage is used, the anodization is referred to as *spark anodizing* and it increases gas evolution and frequently sparking [37], leading to a less uniform and more porous surface.

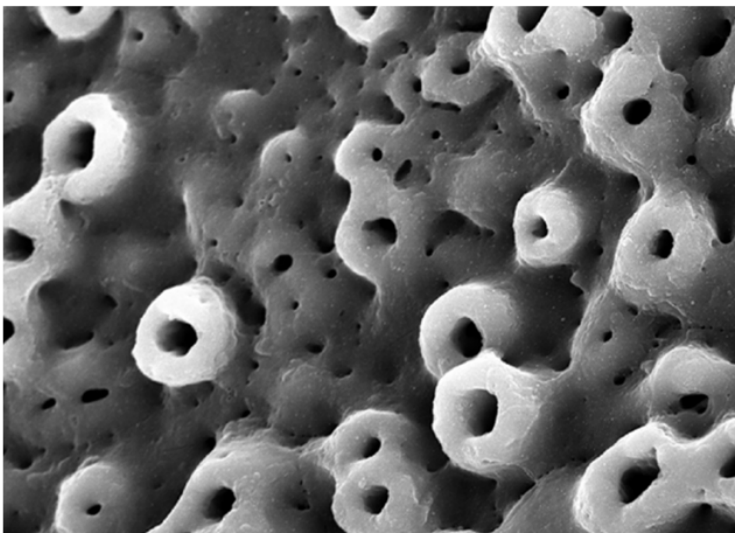

Figure 3-4. Scanning electron micrograph of a porous anodized surface. Note the presence of both nanopores with diameters less than 1 μm and micropores with diameters ranging between 1 and 7 μm. (x1400 original magnification). [12]

The amount of nanometer surface features is dependent on the time of applied voltage [12]. In addition, the diameter of nanotubes and the gap between them are strictly related to the voltage and the density current [11]. Also, porosity and surface roughness depend on the anodization conditions.

When bioactive elements such as Ca and P are added to the electrolyte, they penetrate the oxide layer and make it bioactive. Anodization in an electrolyte composed of β-glycerophosphate sodium and calcium acetate leads to hydroxyapatite growth on the titanium surface by a hydrothermal treatment. The film produced through this type of treatment is 5 – 7 μm thick, porous, highly crystalline, and rich in calcium and phosphorous [37]. Under these conditions, roughness resulted equal to 0.98 μm.

Anodized nanotubular titanium enhances osseointegration as a result of two major mechanisms: a mechanical interlocking through bone growth in pores and a biochemical bonding [13], which is correlated with the presence of bioactive elements on the surface.

3.2 Electron Beam

The main complication of the classic titanium modifications listed above is their propensity to contaminate the substrate material. Additionally, another related problem is the inferior replicability of these methods. Non-contact surface modifications such as surface structuring by electron beam and laser roughening techniques overcome the limitations of common methods for topography changes.

The use of electron beam technology brings with it several advantages, among which there are the high resolution even equal to a few nanometers, the possibility of getting a wide variety of structures and patterns at the microscale level, therefore the generation of a multiscale topography. Besides, the fast repeatable process under vacuum and the very good reproducibility are equally worth considering aspects. The direct writing ability makes electron beam lithography a flexible tool for designing patterns with arbitrary shapes and sizes. Due to the size of the beam focused on the surface of the substrate, about 100-300 µm, a strategy of overlapping of single electron beam beads can be carried out to produce grooves and patterns of 5 µm, 10 µm or 30 µm, as shown in *Fig. 3 – 5*. Despite the possibility of fabricating nanopatterns, electron beam texturing is a high-cost process.

Electron beam uses a similar principle to the conventional scanning electron microscopy (SEM): the high-speed focused electron beam impacts against the surface and causes material melting, local evaporation, and a “keyhole” effect, i.e. the beam creates a hole with vapor pressure in the middle that presses the molten metal against the side walls. Due to the “keyhole” effect, the material transport occurs on the opposite side of the welding direction, so molten material is moved behind the beam and solidifies at the backside. The chamber of EB machine is under vacuum during all the texturing process. *Fig. 3 – 5* shows a schematic illustration of an electron beam principle and an example of an electron beam technique used to design a grooves pattern on commercially pure titanium plane samples [15]. The first parameter to adjust is the energy input, denoted by beam voltage, beam current, and beam velocity. The electron beam is guided by a magnetic field, which in *Fig. 3 – 5* is referred to as “deflector system”.

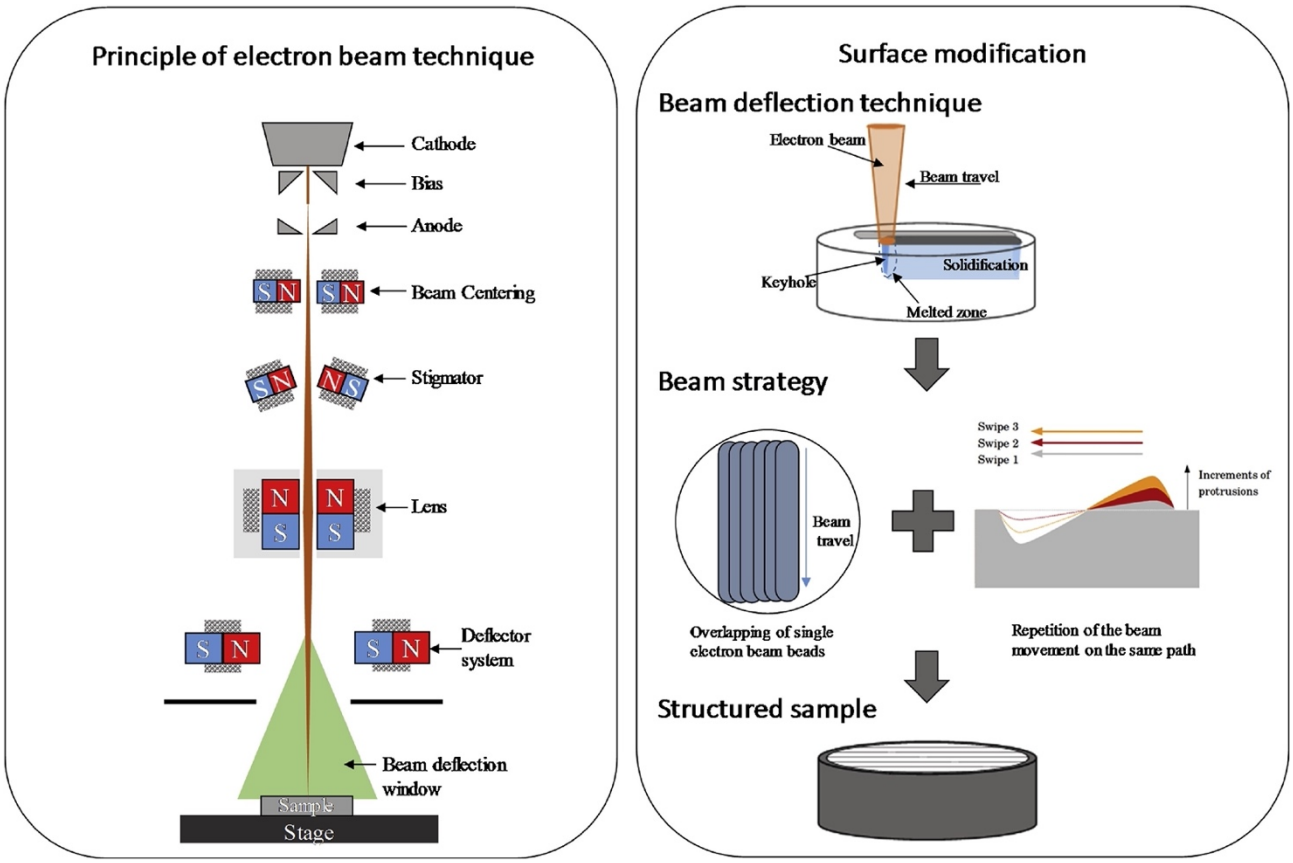

Figure 3-5. Schematic illustration of an electron beam principle and an example of surface modification technique proposed by Ferraris et al. [15]

The amount of melted material depends on the energy, which is regulated by the current applied and the speed of the beam. If the applied energy is too weak, the material doesn't melt, whereas using higher energy the solidification lines are to strong distinct. Whatever energy is applied, provided that it is high enough to melt the metal, a formation of martensite is observed below the melted zone, as illustrated below in *Fig. 3 – 6*. It can be seen in *Fig. 3 – 6 b)* that with increasing energy the martensitic layer increases its thickness.

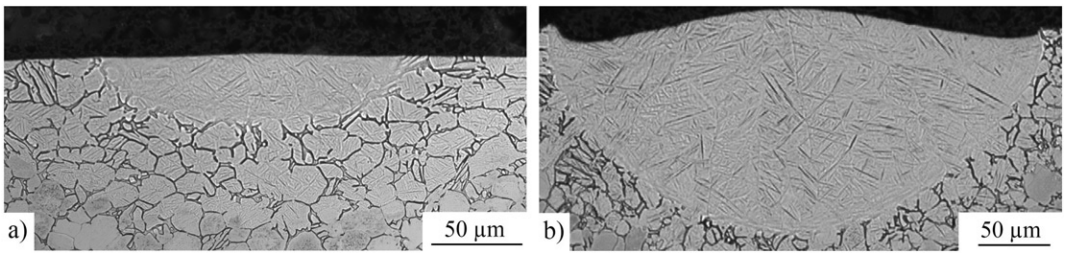

Figure 3-6. Optical microscopy of EB single pass on sample cross section. a) Energy input E=335 J/m, b) Energy input E=555 J/m. [14]

All EB structured samples show the same type of microstructure. *Fig. 3 – 7* illustrates SEM-BSE images of a cross-section of the sample. Ramskogler et al. [14] divided the cross-section into three main zones: the melted zone near the surface, the heat-affected zone, and the base material. In the melted zone, illustrated in *Fig. 3 – 7 b)*, the microstructure has completely converted to martensite (α' phase) resulting from the fast-cooling rate after melting. The heat-affected zone represents a

mixture of α′, primary α, and β phases, as it is visible in *Fig. 3 – 7 c)*. This microstructure could be related to the short exposure time of the solid material at temperatures above the β transus of the material. The microstructure of the base material (*Fig. 3 – 7 d)*) consists of a so-called bimodal microstructure, composed of primary α grains (α_p), and secondary α with lamellar morphology (α_s) and transformed β areas.

An increase in the hardness was observed in the molten zone, which is mainly related to the morphology of the alpha grains, the substructure formation by a non-equilibrium phase transformation, and the thermal stresses related to the process [15]. Additional heat treatments showed a stabilization of the martensitic morphology in the melted zone decreasing the hardness. [14]

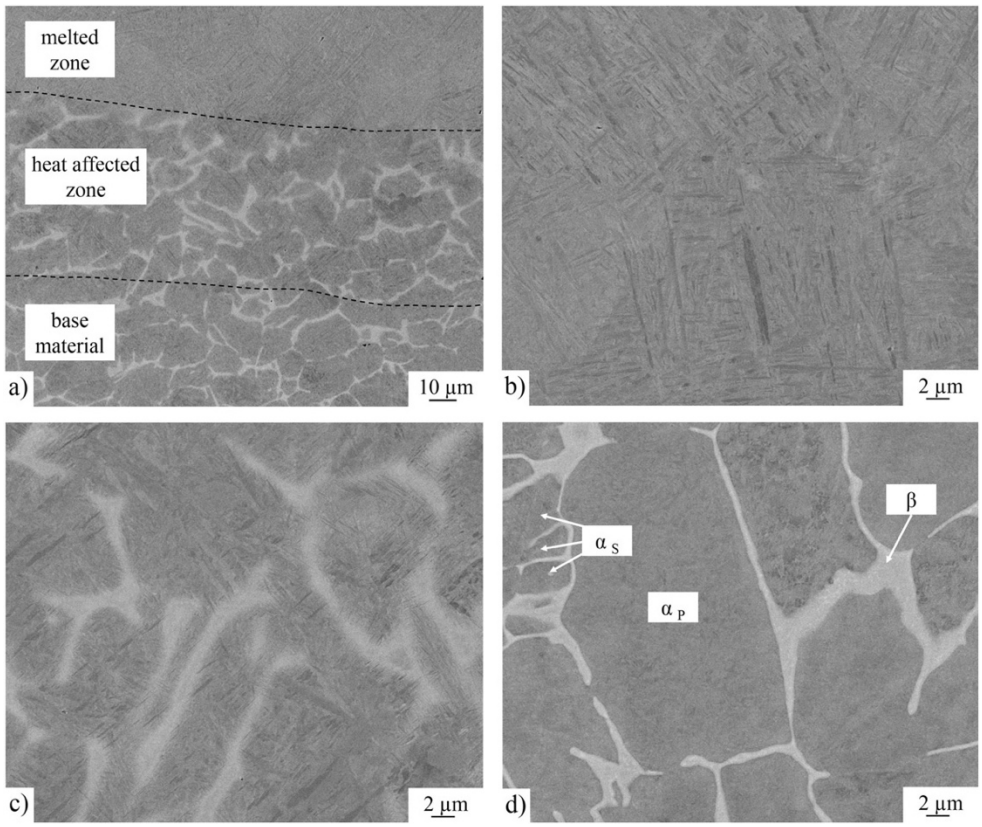

Figure 3-7. SEM-BSE images of cross section after electron beam surface treatment on a Ti6Al4V plate. a) overview and division in three areas, b) detail of melted zone, c) detail of heat affected zone, d) detail of base material. [14]

Electron beam texturing is an innovative technology also because it makes it possible to create almost any type of pattern, with dimensions of the order of nanometers. Recent *in vitro* studies [15,16] highlighted that the production of a grooves pattern on titanium and Ti6Al4V samples with an electron beam leads to an enhancement of adhesion properties since it was observed that fibroblast cells tend to line up along the grooves of a similar dimension (10-15 µm), whereas beyond the expectation a significant reduction of bacteria metabolism was noticed for the EB structured samples, regardless of the size of the grooves.

The antibacterial effect on electron beam textured samples can be attributed to the presence of a microstructure with high density of grain boundaries after EB surface treatment. Therefore, electron beam surface treatment can be considered as an innovative and efficient antibacterial method for metallic materials, even if it would be necessary to deepen the studies in this direction.

3.3 Laser Surface Texturing

Laser surface texturing (LST) is a promising quick, clean, and contact-free technology for generating surface patterns with great potential in the biomedical field. The main advantages of this technique that ensures an enhancement of the tribological properties of the material are high efficiency, remarkable controllability, and accuracy. Compared to traditional long-pulse lasers, ultrafast laser systems, which include pico and femtosecond laser technologies, ensure high pick energy in a very short time and are used to create well-structured surface morphology [23]. Laser technology is often used within companies and research sites, and it may have several functions. For instance, the picosecond laser system used to run the experiment related to this thesis is daily used for industrial applications. Furthermore, many patterns and textures are possible thanks to LST, such as arrays of micro and nanopits or grooves of different sizes.

The literature shows that there are several approaches that exploit laser technology to generate patterns and textures on the work surface. Among them, widely used methods are texturing using laser ablation and texturing using laser interference.

The *laser ablation process* is based on a focused laser beam which generates melting and subsequent vaporization of material which happens due to ablation when the high energy beam of the laser impinges on the surface. When the material is removed, the surface topography is modified, and the desired pattern is obtained. The advantages of this technique are related to its micron-level precision at a faster rate, which involves the development of innovative beam paths by which it is possible to obtain complex geometries [4].

Fig. 3 – 8 shows a representative system of laser texturing by laser ablation.

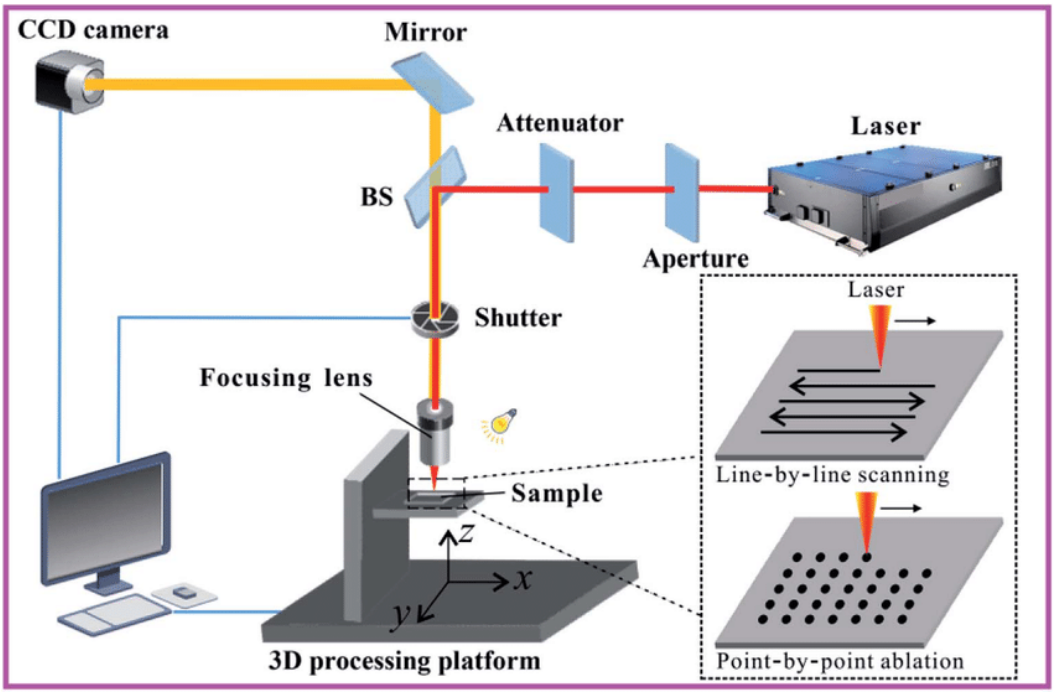

Figure 3-8. Schematic diagram of a typical laser processing system. The two main texturing patterns used in microfabrication are line-by-line scanning and point-by-point ablation. [7]

The sample is placed on the support, which can move, as shown in *Fig. 3 – 8*, or can be stationary. In the latter case, the laser beam draws the desired pattern by moving. The computer controls the movement and the parameters. The optical lens is used to focus the laser on the sample.

The most used processing manners in the microfabrication field are the line-by-line (LBL) scanning pattern and the point-by-point (PBP) ablation pattern, which enables a microholes array design. The LBL manner produces grooves or uniform surfaces, with a very precise roughness. Among the relevant parameters of this technique, there are laser energy, scanning speed, and the interval/shift of the scanning lines [7].

The *laser interference method* allows pattern production through the interference of two or more high-power pulsed laser beams, that generate local heating of the working surface via photothermal interaction between the laser and the working surface. This process can be used not only for nanoscale pattern generation but also for removing contamination or surface oxides of no interest from the surface [4].

In the remaining part of this thesis, I'll focus on laser ablation technology, since it is the most widely used.

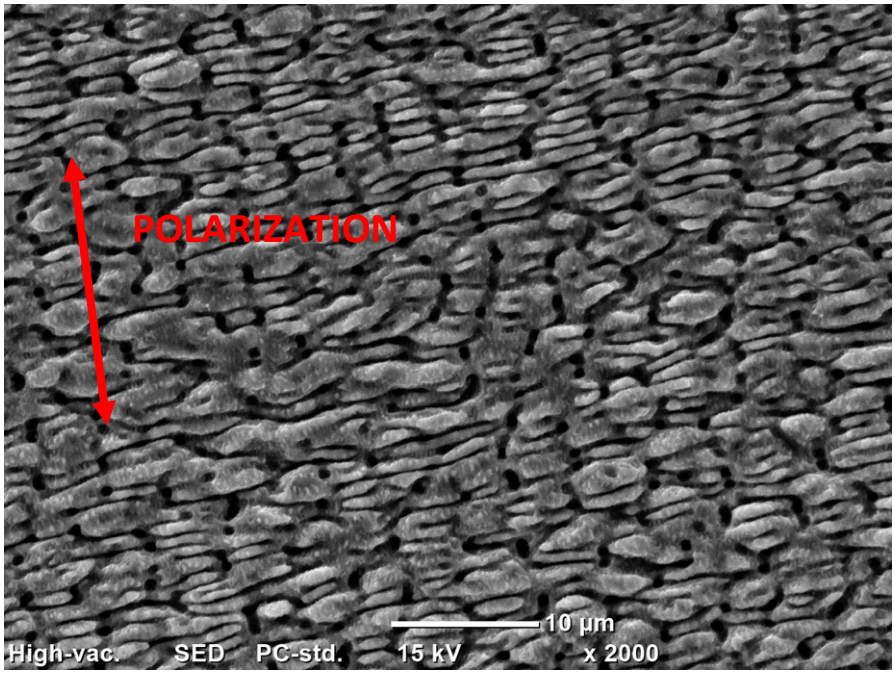

Figure 3-9. SEM image of Low Spatial Frequency LIPSS (LSFL) formed on titanium alloy (Ti6Al4V) surface after irradiation with ps-laser pulses (15 ps, 1064 nm, 500kHz).

Laser-induced periodic surface structures (LIPSS) emerge as almost periodic lines, as shown in *Fig. 3 – 9*, and are a universal phenomenon formed on any type of surface (metals, semiconductors, and dielectrics) irradiated with linearly polarized radiation, such as that emitted by the laser beam. The parameters that several studies have shown to be key for pulsed laser systems in the formation of LIPSS are the laser wavelength λ, the direction of laser beam polarization (if vertical or horizontal), the laser fluence ϕ (energy density in J/cm^2), the number of laser pulses N applied to the same spot [9], [24].

The formation of the LIPSS involves a complex sequence of physical processes, which are based on the absorption of radiation by the electron system of the material hit by the laser beam. The absorption is followed by energy transfer to the crystalline system and several thermal, hydrodynamical, and chemical effects [25]. The process allows the formation of periodic structures through the removal of spatially modulated material (ablation). However, several aspects related to the formation of the LIPSS are still controversial.

As reported by literature and illustrated in *Fig. 3 – 10*, periodic surface structures can be divided in two subgroups according to spatial repetition periods: Low Spatial Frequency LIPSS (LSFL), with a period Λ_{LSFL} at least greater than half the wavelength, and High Spatial Frequency LIPSS (HSFL), which Λ_{HSFL} is lower than $\lambda/2$.

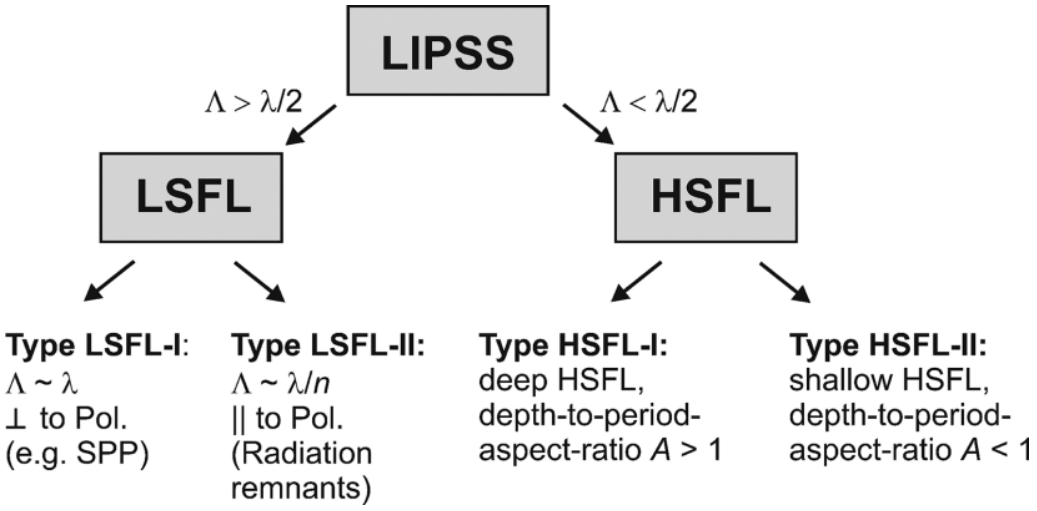

Figure 3-10. Classification scheme of fs-laser-induced periodic surface structures. [25]

LSFL of the first type (LSFL-I) affect strong absorbing materials, such as semiconductors and metals. The direction is perpendicular to the laser beam polarization and the period $\Lambda_{\mathrm{LSFL-I}}$ is close to the wavelength, with a deviation of no more than a few tens of percent. The LSFL-I origin lies in the excitation of Surface Plasmon Polaritons (SPPs), which can interfere with the incident laser beam and then can lead to a modulated energy deposition into the material [24], [25], [26]. Surface plasmon polaritons are electromagnetic waves that move along the interface of a metallic or semiconductor material with any other material (solid or gaseous) and can be excited by both electrons and photons.

LSFL of the second type are formed on dielectric materials, or on materials where the single-photon energy is smaller than the band gap of the material [25]. LSFS-II differ from the former in that they have a direction parallel to the laser beam polarization and their period is approximately equal to $\Lambda_{\mathrm{LSFL-II}} \approx \lambda/\mathrm{n}$, where n is the refractive index of the dielectric material.

LSFL-II are somehow related to the Radiation Remnants (RR), which, according to J.E. Sipe et al. [27], represent a specific non-propagating electromagnetic mode close to the surface, which transfers energy from the incident laser beam to the material.

HSFL formed at fluences very close to the damage threshold of the material and predominantly for pulse duration in the fs-to-ps range [25], however, the origin of HSFL is still controversially

discussed. The depth-to-period-aspect-ratio A illustrated in *Fig. 3 – 10* represents the ratio between the depth d of the grooves and the period Λ_{HSFL} of the HSFL, that is of the order of a few hundreds of nanometers.

In addition to LIPSS, other nanoscale structures can be obtained by changing certain parameters such as energy density and polarization direction, and among these textures are arrays of nanopillars, LIPSS nanotextured microcolumns and parallel lines consisting of nanotextured microcolumns.

Cunha et al. [9], [28] obtained the surface textures shown in *Fig. 3 – 11* using different energies per type and changing the number of laser pulses per surface point. In his study, type 1 texture illustrated in *Fig. 3 – 11 A and B*, consists of LIPSS with an average period of 820 ± 50 nm, which are oriented perpendicularly to the polarization vector of the linearly polarized laser beam. The LIPSS texture was obtained with an average fluence ϕ=0.3 J/cm^2 and a scanning speed of 0.2 mm/s. The roughness measured perpendicular to the direction of the LIPSS is R_a = 290 ± 20 nm.

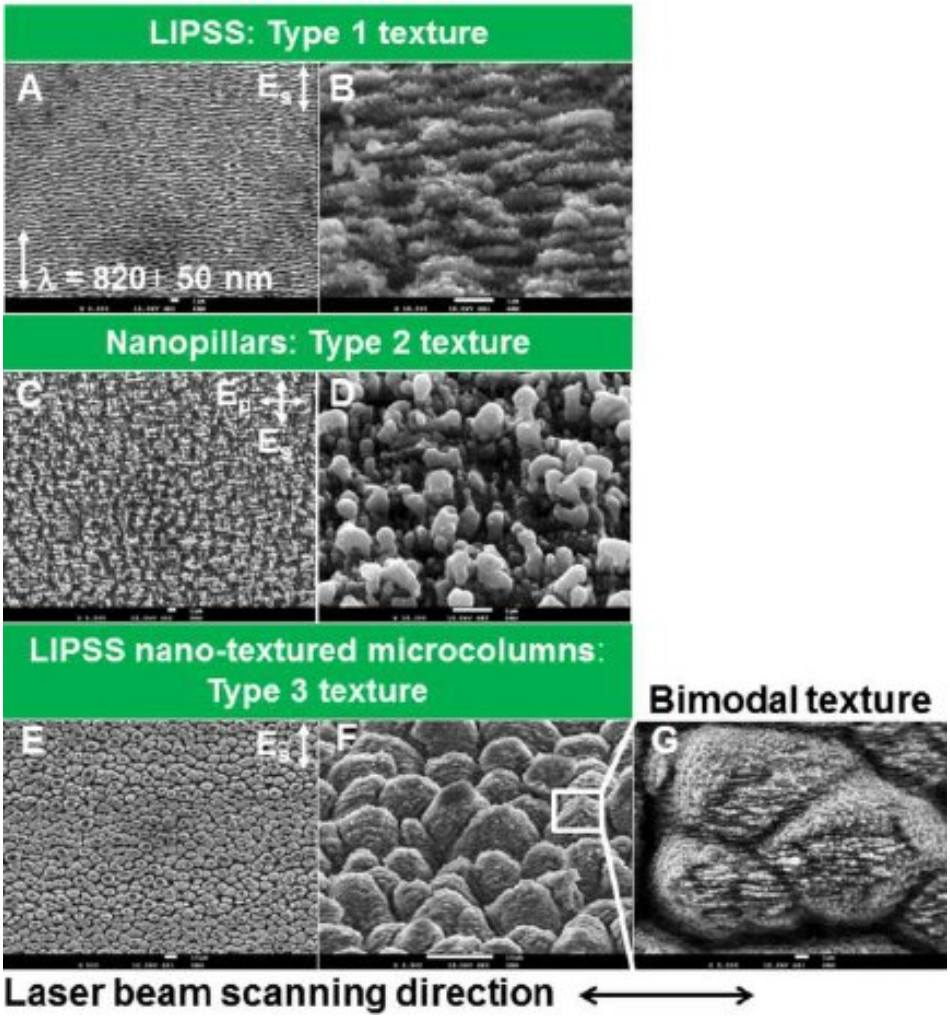

Figure 3-11. SEM micrographs of the textured surfaces. [9]

Nanopillars with hemispherical tops are created by two consecutive laser treatments. The parameters of the former were identical to those used for producing type 1 texture, but for the second treatment the polarization direction was rotated by 90°, a lower energy density of ϕ=0.2 J/cm^2 and a higher scanning rate of 0.8 mm/s were used. Thus, an overlapping of LIPSS with mutually perpendicular

orientations results in type 2 texture, depicted in *Fig.3 – 11 C and D*, and the roughness obtained is $R_a = 260 \pm 10$ nm.

Type 3 texture, illustrated in *Fig. 3 – 11 E, F and G*, is characterized by LIPSS nanotextured microcolumns: the surface has been worked with greater energy than used for previous textures, approximately equal to ϕ=0.6 J/cm^2, and the roughness is equal to 1.1 ± 0.1 μm.

Yu et al. [23] analyzed the surface characteristics of Ti6Al4V samples treated with a picosecond laser and examined the elemental distribution by EDS and the crystal phase by XRD of both groove array samples and polished samples. The results showed that neither the chemical composition nor the position of the characteristic peaks in the X-ray diffraction images change after laser treatment, meaning that picosecond laser texturing did not change the basic crystal structure of titanium alloy. Moreover, the wettability was studied with the tensile drop method and resulted in an increase in the hydrophobicity of the laser textured samples [4], [23] most of the time. However, the literature also points to studies [17] in which wettability is diminished following the laser treatment. This means that wettability is a parameter that strictly depends on the conditions applied and the type of laser treatment carried out.

Also, the literature shows that roughness is a reproducible characteristic, with values ranging from some hundreds of nanometers and a few micrometers.

Literature highlights how the impact of the laser textured material on *in vitro* and *in vivo* studies enhances biological properties and it results in a better response in terms of cells adhesion, interfacial strength, and reduction of a cytotoxic effect linked to the possible release of elements such as Al and V into solution [17], [18], [25] if compared with polished samples or surfaces textured with traditional techniques, such as those mentioned above.

In vivo studies [17] investigated the osteointegration of laser-textured superhydrophilic Ti6Al4V surface in an ovine model and demonstrated that the interfacial strength of laser-treated samples was significantly greater than the machine-finished and grit-blasted control samples. In addition, a significant increase in bone-to-implant contact was measured.

To illustrate the potentiality of laser surface texturing technique with an example of commercially available treatment, Laser-Lok technology by BioHorizons® can be considered.

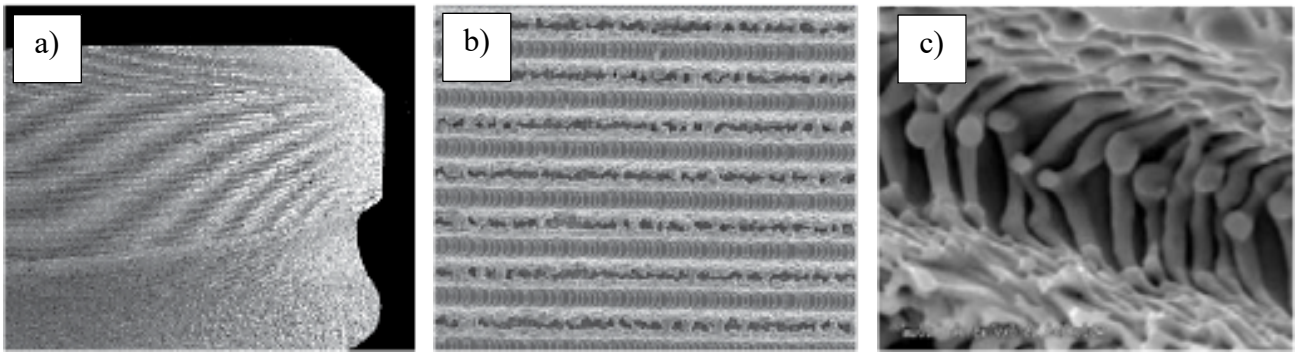

Figure 3-12. SEM images of the Laser-Lok® treated area at different enlargements. a)39x; b)800x, it is possible to distinguish microchannels that organize and promote tissue growth; c) 10000x, the uniformity of the Laser-Lok® microstructure and nanostructure is evident using extreme magnification. [21]

Laser-Lok is a surface treatment for dental implants produced using laser ablation technology. Several studies have shown the excellent biological response following implantation, in particular, it has been observed inhibition of epithelial downgrowth, an attachment of connective tissue, and a huge reduction of bone loss compared to control samples [21].

The surface topography is characterized at the microscale by a series of channels of the same size as the cells, which allow both fibroblasts and osteoblasts to attach and organize themselves in an orderly way.

Furthermore, as shown in *Fig. 3 – 12 c)*, repeating nanostructures maximize surface area and enable cell pseudopodia and collagen microfibrils to interact with the Laser-Lok surface [21].

References

[1] Kumar P.S., KS S., Grandhi V., Gupta V. “The Effects of Titanium Implant Surface Topography on Osseointegration: Literature Review.” *JMIR Biomedical Engineer*. Vol. 4(1):e13237, 2019.

[2] Le Guéhennec L., Soueidan A., Layrolle P., Amouriq Y. “Surface treatments of titanium dental implants for rapid osseointegration.” *Dental Materials Journal.* Vol. 23(7), 2007, p.844-854.

[3] Borsari V., Giavaresi G., Fini M., Torricelli P., Tschon M., Chiesa R., Chiusoli L., Salito A., Volpert A., Giardino R. “Comparative in vitro study on an ultra-high roughness and dense titanium coating.” *Biomaterials*. Vol. 26(24), 2005, p. 4948-4955.

[4] Shivakoti I., Kibria G., Cep R., Pradhan B.B., Sharma A. “Laser Surface Texturing for Biomedical Applications: A Review.” *Coatings.* Vol. 11, 2021, 124.

[5] Kwasniak P., Pura J., Zwolinska M., Wiecinski P., Skarzynski H., Olszewskib L., Marczak J., Garbacz H., Kurzydłowski K.J. “Laser and chemical surface modifications of titanium grade 2 for medical application.” *Applied Surface Science.* Vol. 336, 2015, p.267-273.

[6] Chen J., Bly R.A., Saad M.M., AlKhodary M.A., El-Backly R.M., Cohen D.J., Kattamis N., Fatta M.M., Moore W.A., Arnold C.B., Marei M.K., Soboyejo W.O. “In-vivo study of adhesion and bone growth around implanted laser groove/RGD-functionalized Ti-6Al-4V pins in rabbit femurus.” *Materials Science and Engineering*. Vol 31, 2011, p.826-832.

[7] Yong J., Qing Y., Guo C., Chen F., Hou X. “A review of femtosecond laser-structured superhydrophobic or underwater superoleophobic porous surfaces/materials for efficient oil/water separation.” *RSC Advances.* Vol. 9(22), 2019, p.12470-12495.

[8] Stango S.A., Karthick D., Swaroop S., Mudali U.K., Vijayalakshmi U. “Develpoment of hydroxyapatite coatings on laser textured 316LSS and Ti-6Al-4V and its electrochemical behavior in SBF solution for orthopedic applications.” *Ceramic International*. Vol. 44(3), 2018, p.3149-3160.

[9] Cunha A., Oliveira V., Serro A.P., Zouani O.E.F., Almeida A., Durrieu M.C., Vilar R. “Ultrafast laser texturing of Ti-6Al-4V surfaces for biomedical applications.” *ICALEO 2013 - 32nd International Congress on Applications of Lasers and Electro-Optics*. 2013.

[10] Wennerberg A., Ektessabi A., Albrektsson T., Johansson C., Andersson B. “A 1-year follow-up of implants of differing surface roughness placed in rabbit bone.” International Journal of Oral Maxillofac Implants. Vol. 12(4), 1997, p.486-494.

[11] Bressan E., Sbricoli L., Guazzo R., Tocco I., Roman M., Vindigni V., Stellini E., Gardin C., Ferroni L., Sivolella S., Zavan B. “Nanostructured surfaces of dental implants.” *International Journal of Molecular Sciences*. Vol. 14(1), 2013, p.1918-1931.

[12] Yao C., Perla V., McKenzie J.L., Slamovich E.B., Webster T.J. “Anodized Ti and Ti6Al4V possessing nanometer surface features enhance osteoblast adhesion.” Journal of Biomedical Nanotechnology. Vol. 1(1), 2005, p.68-73.

[13] Schüpbach P., Glauser R., Rocci A., Martignoni M., Sennerby L., Lundgren A., Gottlow J. “The human bone-oxidized titanium implant interface: a light microscopic, scanning electron microscopic, back-scatter scanning electron microscopic, and energy-dispersive x-ray study of clinically retrieved dental implants.” *Clin Implant Dentistry and Related Research*. Vol.7, Suppl. 1, 2005, S36-43.

[14] Ramskogler C., Warchomicka F., Mostofi S., Weinberg A., Sommitsch C. “Innovative surface modification of Ti6Al4V alloy by electron beam technique for biomedical application.” *Materials Science and Engineering.* Vol. 78, 2017, p.105-113.

[15] Ferraris S., Warchomicka F., Ramskogler C., Tortello M., Cochis A., Scalia A., Gautier di Confiengo G., Keckes J., Spriano S. “Surface structuring by Electron Beam for improved soft tissues adhesion and reduced bacterial contamination on Ti-grade 2.” *Journal of Material Processing Tech*. Vol. 266, 2019, p.518-529.

[16] Ferraris S., Warchomicka F., Iranshahi F., Rimondini L., Cochis A., Spriano S. “Electron beam structuring of Ti6Al4V: new insight on the material surface properties influencing the bacterial adhesion.” *Materials*. Vol.13(2), 2020, 409.

[17] Coathup M.J., Blunn G.W., Mirhosseini N., Erskine K., Liu Z., Garrod D.R., Li L. “Controlled Laser Texturing of Titanium Results in Reliable Osteointegration.” *Journal of Orthopaedic Research*. Vol. 35(4), 2017, p.820-828.

[18] Schweitzer L., Cunha A., Pereira T., Mika K., Botelho do Rego A.M., Ferraria A.M., Kieburg H., Geissler S., Uhlmann E., Schoon J. “Preclinical In Vitro Assessment of Submicron-Scale Laser Surface Texturing on Ti6Al4V.” *Materials.* Vol. 13(23), 2020, 5342.

[19] Ong J.L., Carnes D.L., Bessho K. “Evaluation of titanium plasma-sprayed and plasma-sprayed hydroxyapatite implants in vivo.” *Biomaterials*. Vol. 25, 2004, p. 4601-4606.

[20] Velasco-Ortega E., Jimenez-Guerra A., Mosalve-Guil L., Ortiz-Garcia I., Nicolas-Silvente A.I., Segura-Egea J.J., Lopez-Lopez J. “Long-Term Clinical Outcomes of Treatment with Dental Implants with Acid Etched Surface.” *Materials*. Vol. 13, 2020, p. 1553-1565.

[21] BioHorizons, 2017, https://vsr.biohorizons.com/GetDocument?DocumentId=43809, accessed on 13/04/2022

[22] Yu Z., Yang G., Zhang W., Hu J. “Investigating the effect of picosecond laser texturing on microstructure and biofunctionalization of titanium alloy.” *Journal of Materials Processing Tech.* Vol. 255, 2018, p. 129-136.

[23] Yu Z., Yin S., Zhang W., Jiang X., Hu J. “Picosecond laser texturing on titanium alloy for biomedical implants in cell proliferation and vascularization.” *Journal of Biomedical Materials Research*. Vol. 108, 2019, p. 1494-1504.

[24] Bonse J., Krüger J., Höhm S., Rosenfeld A. “Femtosecond laser-induced periodic surface structures.” *Journal of Laser Applications*. Vol. 24, 2012, p. 042006.

[25] Bonse J., Höhm S., Kirner S.V., Rosenfeld A., Krüger J. “Laser-Induced Periodic Surface Structures— A Scientific Evergreen.” *IEEE Journal of Selected Topics in Quantum Electronics*. Vol. 23(3), 2017, 9000615.

[26] Bonse J., Rosenfeld A., Krüger J. “On the role of surface plasmon polaritons in the formation of laser-induced periodic surface structures upon irradiation of silicon by femtosecond-laser pulses.” *Journal of Applied Physics*. Vol. 106, 2009, 104910.

[27] Sipe J.E., van Driel H.M., Young J.F. “Surface electrodynamics: Radiation fields, surface polaritons, and radiation remnants.” *Canadian Journal of Physics*. Vol. 63, 1985, p. 104–113.

[28] Cunha A., Serro A.P., Oliveira V., Almeida A., Vilar R., Durrieu M.C. “Wetting behaviour of femtosecond laser textured Ti-6Al-4V surfaces.” *Applied Surface Science*. Vol. 265, 2013, p. 688-696.

[29] Zupan J. “Mesenchymal Stem/Stromal Cells and Fibroblasts: Their Roles in Tissue Injury and Regeneration, and Age-Related Degeneration.” *Fibroblasts: Advances in Inflammation, Autoimmunity and Cancer, edited by Mojca Bertoncelj, Katja Lakota*. London: IntechOpen, 2021. 10.5772/intechopen.100556

[30] Kensy J., Dobrzynski M., Wiench R., Grzech-Leśniak K., Matys J., "Fibroblasts Adhesion to Laser-Modified Titanium Surfaces – A Systematic Review" *Materials*. Vol. 14, 2021, 7305

[31] Lee B. H., Kim J. K., Kim Y. D., Choi K., Lee K. H. "In vivo behavior and mechanical stability of surface-modified titanium implants by plasma spray coating and chemical treatments" *Journal of biomedical materials research*. *Part A*. Vol. 69(2), 2004, p. 279–285.

[32] https://www.exac.com/wp-content/uploads/2021/01/711-12-80-Titanium-Plasma-Spray-Case-Report.pdf. Visited on 6/05/2022.

[33] Fousova M., Vojtech D., Jablonska E., Fojt J., Lipov J. "Novel Approach in the Use of Plasma Spray: Preparation of Bulk Titanium for Bone Augmentations" *Materials*. Vol. 10, 2017, p. 987-1001.

[34] Asl S.K., Sohi M.H. "Effect of grit-blasting parameters on the surface roughness and adhesion strength of sprayed coating." *Surface Interface Analysis*. Vol. 42, 2010, p. 551-554

[35] Zareidoost A., Yousefpour M., Ghaseme B., Amanzadeh A. "The relationship of surface roughness and cell response of chemical surface modification of titanium." *Journal of materials science. Materials in medicine.* Vol. 23(6), 2012, p. 1479-1488

[36] Nazarov D.V., Zemtsova E.G., Solokhin A. Y., Valiev R. Z., Smirnov V. M. "Modification of the Surface Topography and Composition of Ultrafine and Coarse Grained Titanium by Chemical Etching." *Nanomaterials*. Vol. 7, 2017, p. 15-30.

[37] Liu X., Chu P. K., Ding C. "Surface modification of titanium, titanium alloys and related materials for biomedical applications." *Material Science and Engineering*. Vol. 47, 2004, p. 49-121.

4 Cell Adhesion and Bacterial Proliferation

4.1 Dynamic of Cell Adhesion

Studying cell adhesion is of fundamental importance for understanding the interactions between an implanted biomaterial and the surrounding tissue.

Cell adhesion occurs when a cell binds to another cell of the same type (homophilic bonding) or when a cell binds with other types of cells, with the extracellular matrix (ECM) or with an implanted biomaterial (heterophilic bonding). The cell adhesion phenomenon affects all cells of the body except blood cells. Furthermore, it represents a key aspect in the occurrence of several natural events, such as embryogenesis, maintenance of tissue structure, wound healing, immune response, metastasis as well as tissue integration of biomaterials [1].

Two main conditions of surfaces, considering cell attachment, can be described:

1. The surface of the biomaterial is inert and does not allow cell adhesion and proliferation. This category includes all vascular prostheses, joint prostheses, and blood-contacting devices.
2. Other types of implants require the surface to adhere strongly to the body tissue to ensure adhesion and long-term stability. These include endoprostheses, dental implants, and skin substitutes.

Biocompatibility is defined as the ability of a material to perform its function with an appropriate response from the host living system. Biocompatibility of biomaterials is closely linked to the behavior of the cells and in particular their binding to the surface.

The purpose of a biomaterial is to interact properly with the biological environment by miming the ECM and sending specific signals to cells. To control the behavior of cells, the engineering and modification of the biomaterial surface is a fundamental step in promoting the long-term success of an implanted biomaterial. The main aspects for controlling the interaction force of a biomaterial surface are:

- Surface tension.
- Charge and electric properties.
- Surface roughness. In fact, an increase in the specific area promotes cell adhesion.
- Surface chemistry.
- Mechanical and morphological properties, such as pores, grooves, micro-pits, etc.

What happens in an organism in the presence of a biomaterial can be divided on a time scale. Indeed, in the first fraction of a second following implantation, water molecules and ions form a single or double layer on the surface, thereby creating a hydration shell around the material. The interaction of the water molecules depends on the surface properties, which also influences the protein absorption step.

The cascade of events following implantation begins majorly with protein absorption, which takes place within a few seconds and mediates the actual cell adhesion, which proceeds for several hours.

4.1.1 Protein Absorption

Proteins are charged and composed of functional groups. When proteins interact with an implanted surface can denature and change their orientation and their adhesion ability. The main mechanisms of surface adhesion by proteins are modulated by electrical, chemical, and thermodynamical properties: the process of protein absorption under physiological conditions correlates with a decrease in free energy and an increase in the entropy of the system.

Cell-biomaterial interactions follow two different types of routes of attachment [2]: (i) the cell adhesion is carried out in absence of receptors and (ii) favored and mediated by receptors (which attach to proteins-ligands previously absorbed on the surface). In the former event, (non-receptor mediated), the cells adhere to the surface by weak bonding (hydrogen, polar or ionic, electrostatic bonds) or with the help of chemical groups present on the implant surface. A key aspect of the latter case is a precise controlling of the proteins' conformation and orientation, which is possible through the improvement of topographical and chemical properties of the surface according to the final function of the implant.

Several surface and protein properties influence protein adhesion. For instance, larger proteins may have more contact sites with the surface, and molecules with an isoelectric point close to that of the surface are absorbed more rapidly. The structure of the protein is also important since proteins with a fast-unfolding rate seem to form contact sites with the surface more quickly. Topography and wettability of the biomaterial are key aspects, as increasing the contact area of the surface by, for example, increasing roughness favors protein adhesion. In addition, hydrophobic surfaces bond a major number of proteins.

The biomaterial is covered by proteins from the extracellular matrix ECM. Among the proteins present in the blood plasma, fibrinogen is found in a high concentration. Because of this it initially adheres to the surface. It is often proposed that in its adsorbed state it does not support biocompatibility [2]. However, hemoglobin, although it is a smaller protein found in a very minute amount in the plasma, is adsorbed in concentrations similar to those of fibrinogen. Also, IgG, albumin, and kininogen are proteins contained in blood plasma.

Other proteins present in the ECM are laminin, collagen, vitronectin, and fibronectin. Fibronectin attachment to the implant surface enhances chemotaxis and focal adhesion of osteogenic cells. Fibronectin is capable of activating signaling pathways involved in cell-cycle progression, gene expression, matrix mineralization, and osteoblast regulation [25]. It, therefore, follows that fibronectin plays a key role in osteogenesis.

Since there are a finite number of anchoring sites on the surface, proteins in solution compete for these sites. Molecules with higher diffusion coefficient, which mean higher concentrations and/or smaller proteins, reach the surface more quickly. Over time, proteins with a higher affinity also arrive on the surface more slowly, and a competitive exchange takes place. The formers fall off, leaving sites for the latter, which occupy the newly available binding sites. This event is called the "Vroman" effect and, by way of example, occurs when fibrinogen is initially adsorbed due to its high cytoplasmatic concentration, and it is later displaced by proteins that are more surface-active, such as kininogen [2]. The Vroman effect is schematically represented in *Fig. 4 – 1*.

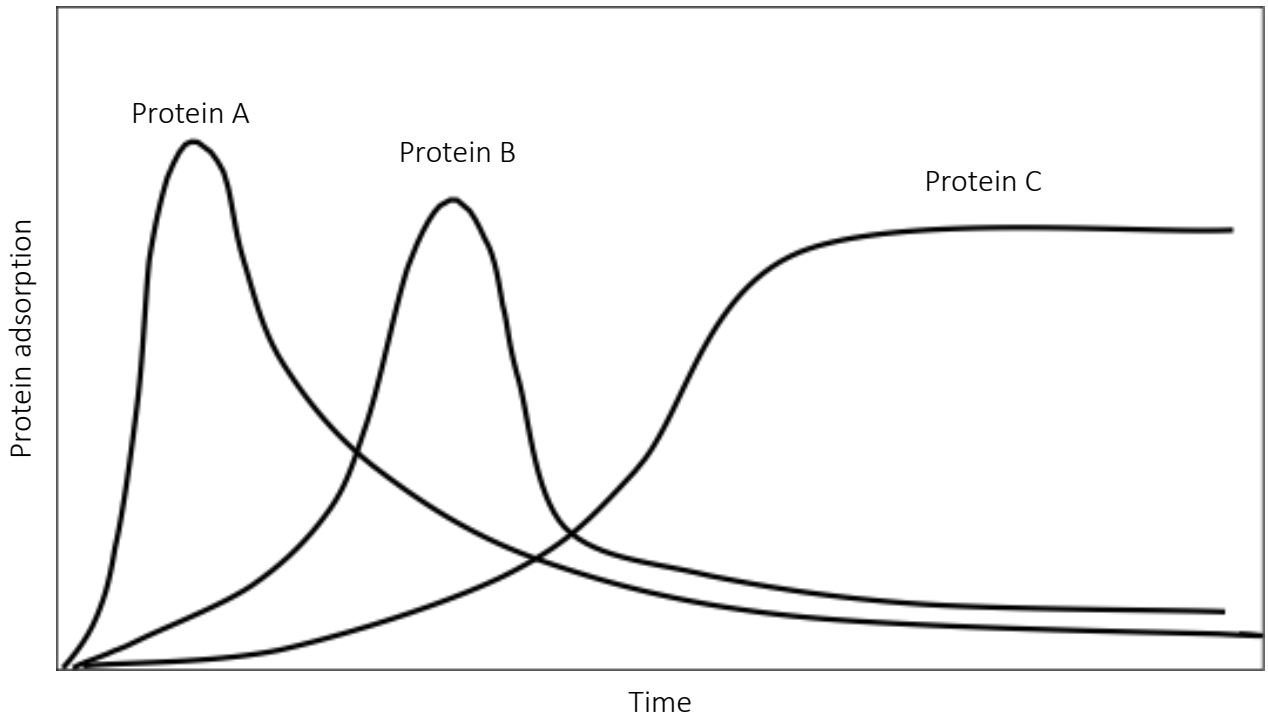

Figure 4-1. Schematic representation of the sequential protein exchange process on the surface (Vroman effect).

The proteins bonded to the material intensify the attachment of cells, which possess receptors (cell-membrane-spanning proteins), binding distinctively to the adhered proteins known as *ligands* [2]. The process of protein pre-adsorption also encourages the cell to flatter and spread on the biomaterial. [12]

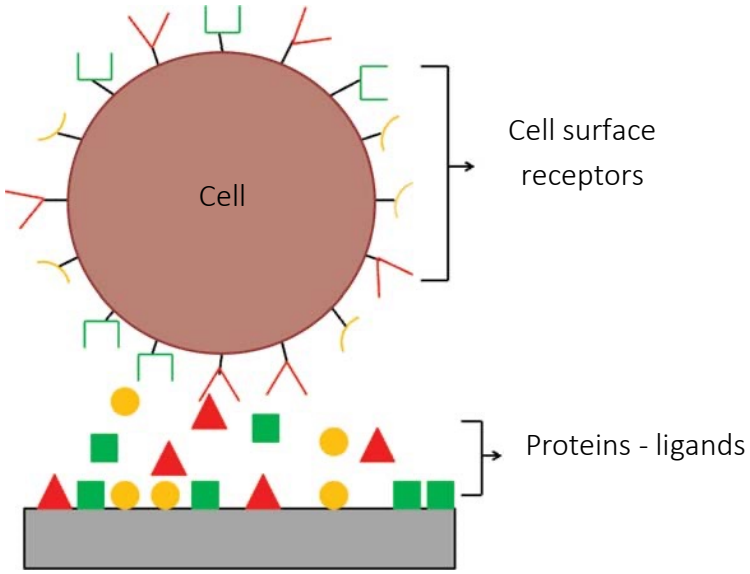

Figure 4-2. Enlarged view of the cell with its receptors and the layer of proteins-ligands adsorbed on the biomaterial surface. (Adapted from [2].)

As shown in *Fig. 4 – 2*, the biomaterial surface is covered by a layer of proteins-ligands from the ECM, such as fibronectin, laminin, collagen, and vitronectin, which result from the protein adsorption

process. The cell surface receptors involved in cell-protein interactions are named *integrin proteins*, present on most of the cells, and they recognize a sequence of amino acids called RGD and composed of Arg-Gly-Asp, which is present on several proteins. Integrins bind to the receptor-specific peptide sequence RGD through α and β domains, which represent the integrin receptors. In addition to the RGD sequence, integrins can also bind to the nearby amino acids [2].

4.1.2 Cell adhesion

As described in the previous chapter, cell adhesion is mediated by the absorption of proteins through receptors-ligands bonding. Integrins recruit regions on the cell membrane called *focal adhesion sites* (*Fig. 4 – 3*) which are represented by focal adhesion proteins, which are membrane-associated cytoskeleton proteins, which link integrin receptors with the actin cytoskeleton [2]. Hence, focal adhesion proteins influence cell behavior and endocytosis, influencing proliferation, differentiation, and apoptosis.

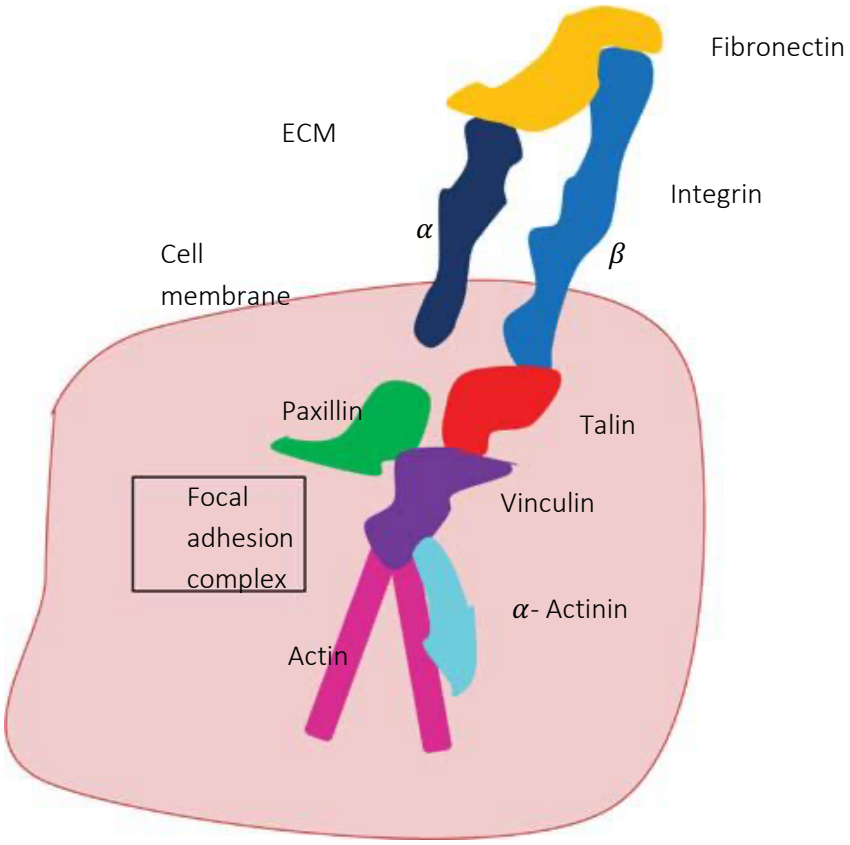

Figure 4-3. Interaction of the ECM proteins with those of the focal adhesion complex [2].

The receptor-mediated cell adhesion strictly depends on the physical and chemical properties of the surface, including wettability, roughness, porosity, topography, electrical charge, pH, crystallinity, and chemical functional groups.

Wettability is a key feature concerning cell adhesion since it is widely recognized that cell spreading is promoted by a hydrophilic surface. Osteoblast adhesion is favored by contact angles between 0° and 90°, whereas fibroblast spreading is promoted by contact angles between 60° and 90° [5], [6].

The amount of surface charge affects cell behavior [2]. Proteins have a positive or negative charge when the solution is acidic or alkaline respectively, while cells have a negative resting transmembrane potential, so it's easy to understand the importance of the surface charge role in applications of tissue engineering and cell biology. However, the molecular mechanisms behind the modulation of cellular activities dependent on surface charge are still not understood clearly [2].

Texture modification dramatically affects guiding tissue growth. Contact guidance occurs when cell activity is directed by a pattern in a biomaterial surface [2] and it is achieved through the application of surface treatments leading to the production of grooves, pits, or other surface textures, as shown in the previous chapter. Surface patterns promote cells to change their shape, aligning and elongating along with the shape of the surface. Changing topography and roughness in a controlled manner prevents epithelial down-growth on dental implants [4], thus inducing the implant to better long-term stability. Different cell strains are diversely sensitive to roughness, for instance, it is widely known from the literature that osteoblasts are particularly rugophilic, whereas fibroblasts preferentially adhere to smooth surfaces, but they are sensitive to the contact guidance phenomenon. These characteristics can be exploited to improve the biocompatibility of an implant. As an example, considering a dental implant, the abutment's surface, which is the part that most closely adheres to the connective tissue of the gingiva mainly composed of fibroblasts, should be characterized by a low-rough grooved topography, with a characteristic size close to that of the cells – approximately 10 μm, to allow their correct alignment along the grooves. The fixture should instead favor osseointegration of the implant with the alveolar bone, so its surface should be rough in order to enhance osteoblast adhesion. According to Albrektsson and Wennerberg [16], the range of roughness that seems to promote osseointegration is about 1-2 μm, mimicking the dimensional scale of the cells. Despite that, surface modification can also be used to generate protein-resistant surfaces, which are desirable for blood contact applications such as vascular grafts [2].

Subsequently, after cell-protein interaction, cells relate with each other through a so-called *homophilic* interaction, which is mediated by calcium-dependent cadherin proteins.

When considering titanium and Ti6Al4V titanium alloy for dental or orthopedic applications, it is desirable that bone tissue (in the case of both dental and orthopedic implants) or soft tissue (for dental applications) adheres properly to the surface. Therefore, osteoblasts' and fibroblasts' adhesion plays a key role in the long-term success of the implant. The following two sub-chapters will focus on the behavior of fibroblasts and osteoblasts, with a special focus on dental and titanium implants.

4.1.3 Fibroblasts

Fibroblasts are the most abundant cells of connective tissue and provide the majority of the structural framework of almost all types of tissues. They play a key role in the secretion of extracellular matrix molecules, such as collagen for tissue regeneration after injuries, proteoglycans, and others. Therefore, fibroblast cells act in tissue development, maintenance, and repair [7].

Together with mesenchymal stem cells (MSCs), fibroblasts intervene in the presence of an inflammatory reaction, allowing the normal resolution of inflammation to take place, thus leading to successful tissue repair.

The importance of fibroblast adhesion in tissue engineering is mainly linked to the dental implant sector since the epithelium forms a barrier that seals the implant surface from contaminants in the oral environment and migrates apically if not properly supported by the connective tissue interface [8],[21]. *Fig. 4 – 7* depicts the approximate percentage of soft and hard tissue adhering to the implant: epithelium represents the 17% of the tissue that comes into contact with the implant, while connective tissue is 18% [20]. When the epithelial tissue shrinks, gingival recession, pocket formation, and bone resorption can occur, leading to implant failure.

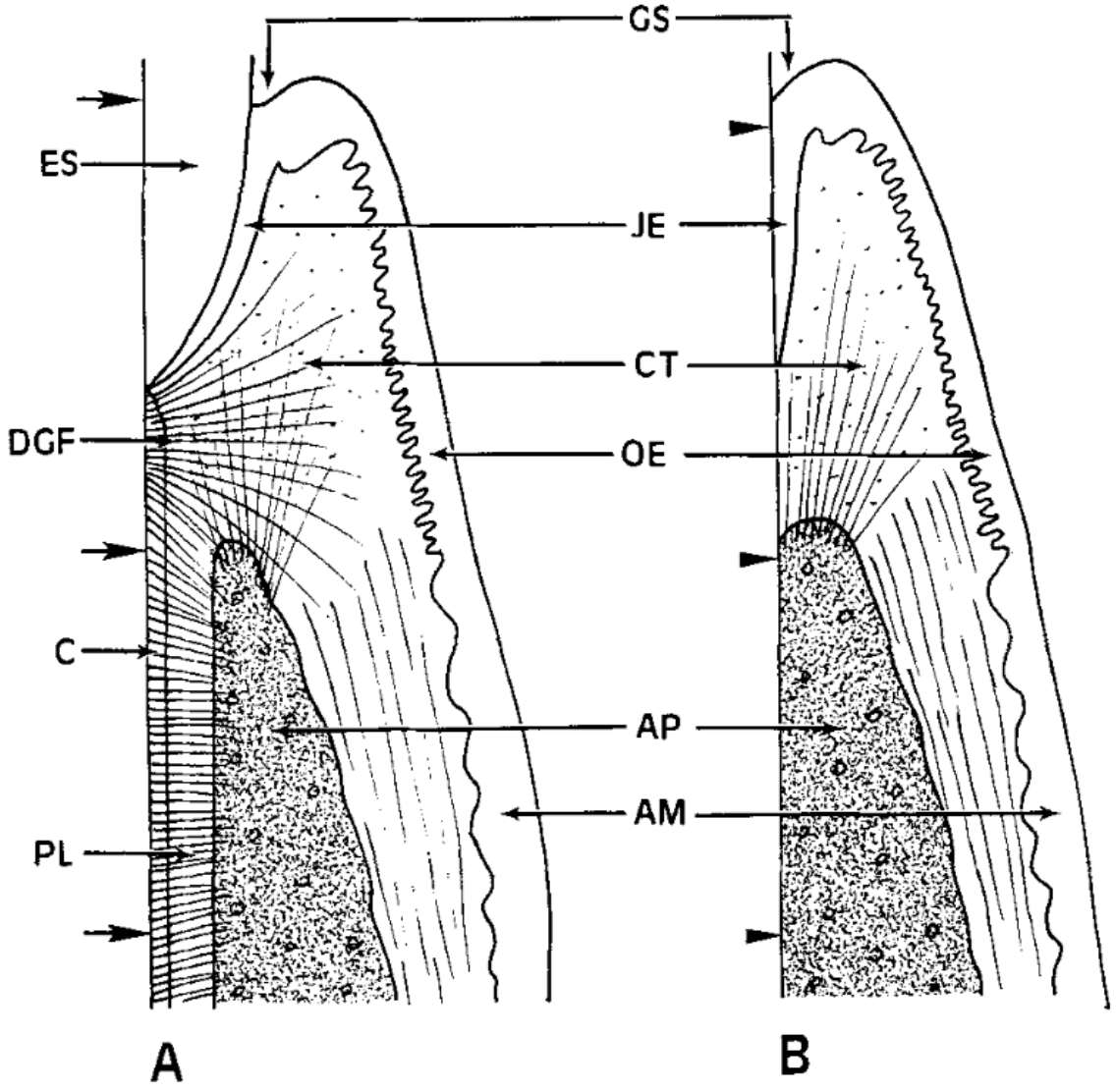

Figure 4-4. Diagrammatic illustration of the interfacial region between A) a tooth and the periodontal tissue and B) an implant and the periimplant tissue.GS: gingival sulcus; JE: junctional epithelium; CT: gingival connective tissue; OE: oral epithelium; AP: alveolar process; AM: alveolar mucosa; ES: enamel space; C: cementum layer; PL: periodontal ligament; DGF: dento-gingival fibers. [11]

The main difference between a natural healthy tooth and a correctly healed implant is that in the former case the gingiva is attached to the enamel space by junctional epithelium and dento-gingival fibers, which extend from the gingival connective tissue into the cementum layer that covers the roots, and the primary anchorage is through the periodontal ligament [11]. On the other hand, in the latter

case, the anchorage is provided by osseointegration of the implant surface with the bone of the alveolar process, and both the cementum layer, the periodontal ligament, and the dento-gingival fibers are missing. As illustrated in *Fig. 4 – 4* and *4 – 7*, the gingival connective tissue, together with the bone of the alveolar process, is the main source of anchorage of the dental implant and provides long-term success stability.

Dental implants are introduced into a site that is surgically created within mature tissues, so the peri-implant tissue which forms after implantation is a result of a wound healing process [11]. Fibroblasts, the major constituents of connective tissue, are therefore cells whose correct adhesion to the surface of the biomaterial allows the correct development of the peri-implant tissue and the successful implantation.

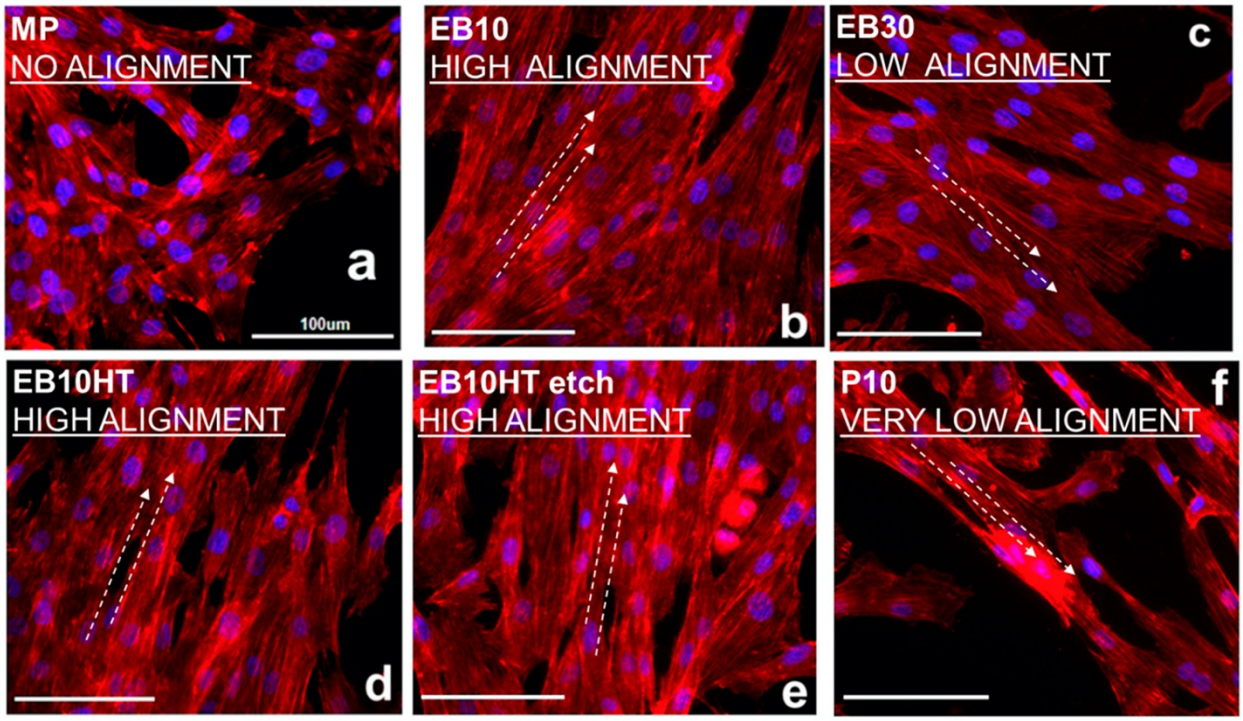

Figure 4-5. Fibroblast alignment on the different samples after 48h culture. A) Mirror polishing sample (MP) with smooth surface. B) and C) Electron beam samples with grooves respectively of 10 µm width and 30 µm width. D) Electron beam structuring + heat treatment sample with grooves of 10 µm width. E) Electron beam structuring + heat treatment + etching sample with grooves of 10 µm width. F) Polished sample after laser treatment. [19]

Literature highlights that a surface-functionalized to improve fibroblasts adhesion leads to better subsequent development of connective tissue, and therefore to long-term success in dental implantation. Fibroblasts are rugo-phobic, which means that their adhesion is reduced on rough surfaces [18], but they can align on parallel grooves as shown in *Fig. 4 – 5*, following the contact guidance phenomenon. For this reason, in order to make a dental implant as stable as possible, it is desirable for the abutment area to have a smoother surface with grooves of 10 µm width [19] in order to promote epithelial cell adhesion, prevent inflammation [20],[21] and the formation of a stable soft tissue barrier [10].

Most types of laser surface treatments are able to produce a low-rough oriented topography stimulating fibroblasts to adhere and proliferate [9]. The growth and elongation of fibroblasts along the surface improve long-term implant stability since titanium dental prostheses after implantation

are surrounded by peri-implant mucosal tissue, a connective tissue that includes epithelial cells and fibroblasts. The mucosa attachment protects the peri-implant bone from bacteria contamination and the oral environment, preventing pathologies.

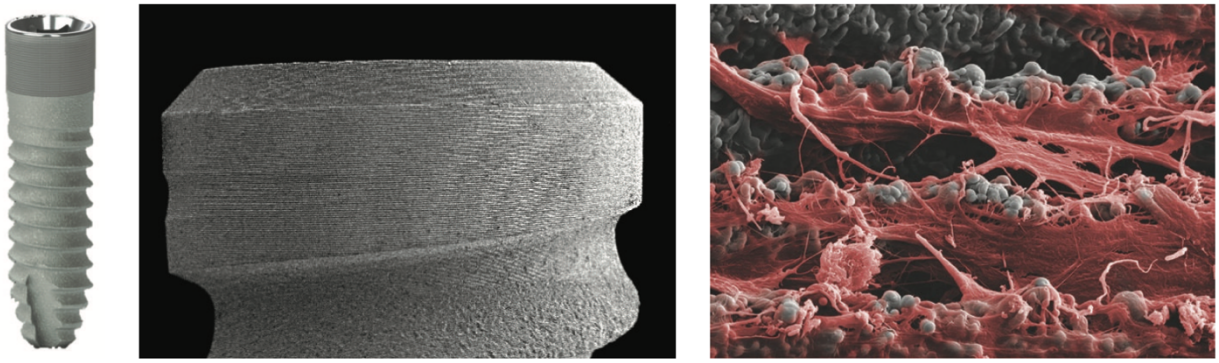

Figure 4-6. (a) Laser-Lok implant (BioHorizons, Birmingham, AL, USA). (b) A pattern of grooves around the implant abutment is created by laser treatment. (c) Attachment of connective tissue. Courtesy of BioHorizons IPH Inc.

One type of laser-treated implant that is currently on the market is the Laser-Lok implant (BioHorizons, Birmingham, AL, USA), and its processing technique focuses on improving the adhesion of fibroblasts, and more in general connective tissue, with the aim of enhancing the integration of dental implant. Nevins et al. [21] in an *in vivo* model have demonstrated that connective tissue formation around the Laser-Lok abutment is aligned along the microchannels. *Fig. 4 – 6 (c)* shows the organization of connective tissue, which actually occurs parallel to the grooves. The soft tissue seal has been claimed to act like a barrier, preventing apical migration of junctional epithelium.

4.1.4 Osteoblasts

The synthesis and calcification of the bone matrix are governed by the osteoblast (bone-generating cells). The organic bone matrix is composed of over 90% of type I collagen. Under physiological conditions, osteoblasts produce type I collagen fibers in a highly organized fashion such that they are aligned in parallel to each other ad form lamellar bone [14]. The pores between the fibers are sites of mineral nucleation. Since osteoblasts govern the overall process of bone maintenance and directly regulate bone matrix synthesis and mineralization [13], they affect the osseointegration of an implant, defined as the direct contact between living bone and the implant surface. Bone is a dynamic tissue that is constantly remodeled by the coordinate actions of osteoblasts and osteoclasts [14], whereby the interface between the surface of the biomaterial and of the bone tissue must promote cell adhesion and proliferation in order to ensure the success of the implant.

The dental implant is directly in contact with the bone as figured in *Fig. 4 – 4* and *4 – 7*, and it goes osteointegration unless a looser union mediated by a fibrous capsule is formed. In the long term, the fibrous capsule does not guarantee stability [11].

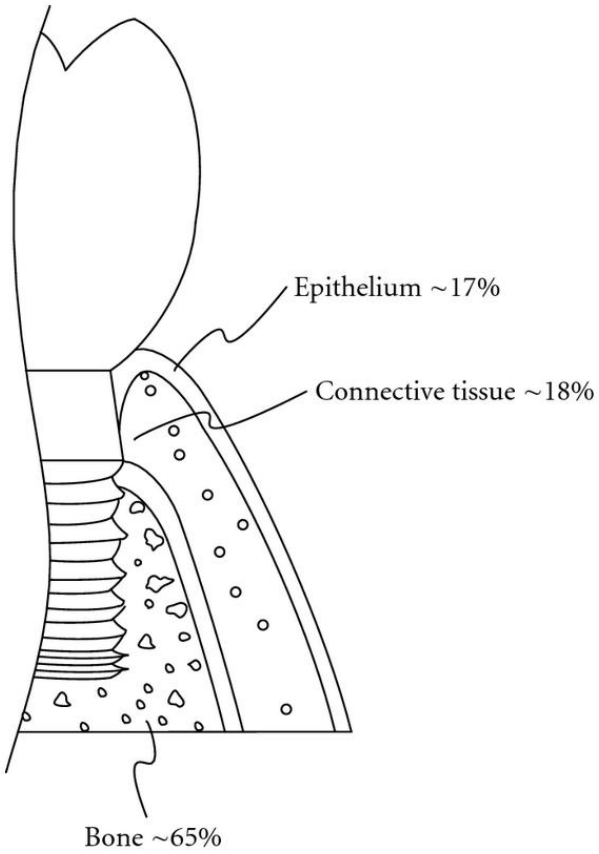

Figure 4-7. A diagrammatic illustration showing the relationship of the interfacial parts between periodontal tissues and an implant (length: 5.7 mm). Assuming proper adhesion of the implant surface to the tissues, the relationship between the bone of the alveolar process, the gingival connective tissue, and the junctional epithelium is shown [20].

As figured in *Fig. 4 – 7,* the bone tissue of the alveolar process represents the major part of the tissue that interacts with the titanium surface and the total fixture part. It is intended that the fixture section of a dental implant has a rough surface since it provides soluble ions which enhance the early-stage proliferation of osteoblast cells [20]. In fact, it is recognized by several studies [1],[15],[17],[20] that increasing degrees of roughness outstandingly elicits enhanced levels of bone cell proliferation since osteoblasts result to be rugophilic. According to Albrektsson and Wennerberg [16], the range of roughness that seems to promote osseointegration is about 1-2 μm, mimicking the dimensional scale of the cells.

Coathup et al. [26] in an *in vivo* study investigated the osteointegration of laser-textured Ti6Al4V surface in an ovine model and have concluded that there is a significant increase in bone-to-implant contact in laser-treated samples compared to control samples, meaning that osseointegration and osteoblast adhesion are facilitated by the treatment.

4.2 Bacteria, The Agents of Infections

Bacteria make up the majority of prokaryotic microorganisms, do not contain a nucleus, and have a membrane consisting of phospholipids, like eukaryotic microorganisms, but differ from the latter in that their structure is very rigid and the membrane inflexible. Bacteria have a characteristic length of

a few micrometers (1-2 µm) and are found in several shapes, like spherical, rod, or twisted. Bacteria live in several environments, in a symbiotic and parasitic relationship with plants and animals. Most of them are harmless to the protective effects of the immune system, some are beneficial. However, several species of bacteria are pathogenic and can cause infections.

Surgical site infections are mainly caused by bacteria, with *Staphylococcus aureus* representing the most common pathogen. *S. aureus* is particularly aggressive and resistant to antibiotic treatment, forming a protective layer for bacteria shielded from immune effector mechanisms. It initiates local and systemic production of cytokines, that bind to proteins associated with death domains and to inflammatory mediators, triggering an apoptotic pathway.

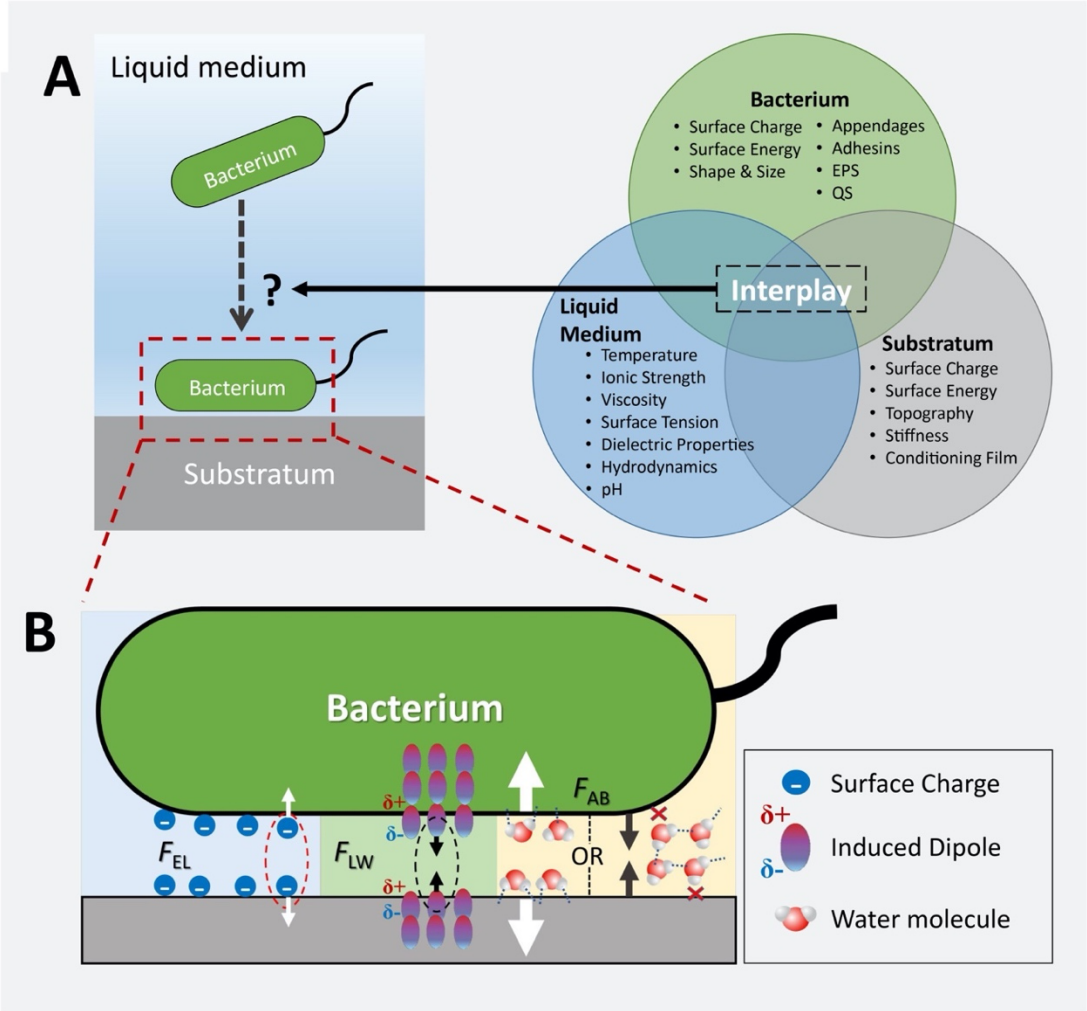

Figure 4-8. A schematic representation of the factors that influence initial bacterial attachment to an interface. A) The bacteria adhesion on the surface is mediated by the interplay of three leading actors: the bacterium, the substratum, and the liquid medium. B) Forces and other factors that affect interaction: F_{EL} electrostatic interactions, F_{LW} van der Waals interactions, F_{AB} acid-base interactions. Figure from [27].

The early implant marginal bone loss can expose the micro-texture of the surface to an implant–tissue gap of 10-50 µm, within which fluids with bacteria can infiltrate [22]. Micromovements of the implant following infiltration can lead to bone loss around the neck, inflammatory reaction, and even peri-implantitis, whether biofilm is present. Biofilm is an agglomeration of bacteria, durable and persistent, which leads to enormous rejection and inflammation problems.

The interaction between the implant surface and the bacteria is still not entirely clear, and this is because the attachment is mediated by many different factors and forces, as illustrated in *Fig. 4 – 8*, and bacterium bonding to the surface is a result of the complex interplay between the bacterium, the surface, and the surrounding medium [27]. However, several studies about the relationship between surface roughness and bacteria ([23],[24]) have revealed that the roughness threshold below which bacterial adhesion does not increase is 0.2 μm, a value about an order of magnitude smaller than the size of bacteria, which, being rigid and non-splitting, do not fit on the surface.

Despite that, literature regarding the influence of topography on bacterial adherence led to contradictory results. It should be considered that part of the topographical information is lost when roughness is used as the only descriptor of surface topography, and surfaces with similar roughness can have different topographies, which relate to bacteria in different ways. Additionally, as shown in Fig. 4 – 8 other physiochemical factors contribute to bacterial adhesion. Furthermore, it seems that different antifouling mechanisms may "switch on" at different topographical scales [27]. Further investigation into the subject would be necessary to better clarify and understand the mechanisms of the bacterial response.

References

[1] Anselme K. “Osteoblast adhesion on biomaterials” *Biomaterials*. Vol. 21, 2000, p. 667-681.

[2] Balani K., Verma V., Agarwal A., Narayan R., “Tissue interaction with biomaterials.” in *Biosurfaces: A materials science and engineering perspective*. John Wiley & Sons, Incorporated, Hoboken, New Jersey, 2015.

[3] Balani K., Verma V., Agarwal A., Narayan R., “Host response of implanted biomaterials.” in *Biosurfaces: A materials science and engineering perspective.* John Wiley & Sons, Incorporated, Hoboken, New Jersey, 2015.

[4] Kuhn L.T. “Biomaterials.” In *Enderle J.D. and Bronzino J.D. Introduction to Biomedical Engineering.* Academic Press Series in Biomedical Engineering, 2012.

[5] Tamada Y., Ikada Q. “Effect of preadsorbed proteins on cell adhesion to polymer surfaces.” *Journal of Colloid Interface Science*. Vol. 155(2), 1993, p. 334–339.

[6] Wei J., Igarashi T., Okumori N., Igarashi T., Maetani T., Liu1 B., Yoshinari M. “Influence of surface wettability on competitive protein adsorption and initial attachment of osteoblasts.” *Biomedical Materials*. Vol. 4(2), 2009, 045002.

[7] Zupan J. “Mesenchymal Stem/Stromal Cells and Fibroblasts: Their Roles in Tissue Injury and Regeneration, and Age-Related Degeneration.” in *Bertoncelj, M. F., Lakota, K. Fibroblasts - Advances in Inflammation, Autoimmunity and Cancer.* IntechOpen, 2021.

[8] Baltriukienė, D., Sabaliauskas, V., Balčiūnas, E., Melninkaitis, A., Liutkevičius, E., Bukelskienė, V., Rutkūnas, V. “The effect of laser-treated titanium surface on human gingival fibroblast behavior.” *Journal of Biomedical Materials Research*. Part A, Vol. 102(3), 2014, p. 713–720.

[9] Kensy J., Dobrzynski M., Wiench R., Grzech-Leśniak K., Matys J., “Fibroblasts Adhesion to Laser-Modified Titanium Surfaces – A Systematic Review.” *Materials*, vol. 14, p. 7305, 2021.

[10] Canullo L., Genova T., Trujillo E.G., Pradies G., Petrillo S., Muzzi M., Carossa S., Mussano F. “Fibroblast Interaction with Different Abutment Surfaces: In Vitro Study.” *International Journals of Molecular Science*. Vol. 21, 2020, p. 1919-1937.

[11] Listgarten M.A., “Soft and Hard Tissue Response to Endosseous Dental Implant” in *The Anatomical Record*. Vol. 245, 1996, p. 410-425.

[12] Suzanne G.E. et al. “Some background concepts.” in *Ratner BD, Hoffman AS, Schoen FJ, editors. Biomaterials Science – An Introduction to Materials in Medicine*. 2nd ed. Elsevier Academic Press; 2004.

[13] Rosemberg N., Rosenberg O., Soundry M. “Osteoblasts in Bone Physiology – Mini Review.” *Rambam Maimonides Medical Journal*. Vol. 3(2), e0013, 2012.

[14] Bradley E.W., Westendorf J.J, van Wijnen A.J., Dudakovic A. “Osteoblasts: Function, Development and Regulation.” in *Bilezikian J.P. Primer on the Metabolic Bone Diseases and Disorders of Mineral Metabolism.* John Wiley & Sons, Incorporated, 2018, Newark.

[15] Brett P.M., Harle J., Salih V., Mihoc R., Olsen I., Jones F.H., Tonetti M. “Roughness response genes in osteoblasts.” *Bone*. Vol. 35, 2004, p. 124-133.

[16] Albrektsson T., Wennerberg A. “Oral implant surfaces: Part 1--review focusing on topographic and chemical properties of different surfaces and in vivo responses to them.” *The International journal of prosthodontics.* Vol. 17(5), 2004, p. 536-43.

[17] Smeets R., Stadlinger B., Schwarz F., Beck-Broichsitter B., Jung O., Precht C., Kloss F., Gröbe A., Heiland M., Ebker T. “Impact of Dental Implant Surface Modifications on

Osseointegration." *BioMed Research International.* Vol. 2016, 2016: 6285620. doi:10.1155/2016/6285620

[18] Bauer S., Schmuki P., von der Mark K., Park J., "Engineering Biocompatible Implant Surfaces: Part I: Materials and Surfaces" *Progr. Mater. Sci*. Vol. 58, 2013, p.261-326.

[19] Ferraris S., Warchomicka F., Iranshahi F., Rimondini L., Cochis A., Spriano S. "Electron beam structuring of Ti6Al4V: new insight on the material surface properties influencing the bacterial adhesion." *Materials*. Vol.13(2), 2020, p. 409-420.

[20] Teng, F. Y., Ko, C. L., Kuo, H. N., Hu, J. J., Lin, J. H., Lou, C. W., Hung, C. C., Wang, Y. L., Cheng, C. Y., Chen, W. C. "A comparison of epithelial cells, fibroblasts, and osteoblasts in dental implant titanium topographies." *Bioinorganic chemistry and applications.* 2012, 687291. https://doi.org/10.1155/2012/687291

[21] Nevins M., Kim D.M., Jun S.H., Guze K., Schupbach P., Nevins M.L. "Histologic evidence of a connective tissue attachment to laser microgrooved abutments: a canine study." *The International Journal of Periodontics & Restorative Dentistry*. Vol. 30(3), 2010, p. 245-255.

[22] Insua A., Monje A., Wang H.L., Miron R.J. "Basis of bone metabolism around dental implants during osseointegration and peri-implant bone loss." *Journal of biomedical material research*. Vol. 105, 2017, p. 2075-2089.

[23] Frijd V., Linderback P., Wennerberg A., de Paz L.C., Svensater G., Davies J.R. "Effect of nanoporous TiO_2 coating and anodized Ca^{2+} modification of titanium surfaces on early microbial biofilm formation." *BMC Oral Health*. Vol. 11(8), 2011.

[24] Quiryen M., Bollen C.M.L., Papaioannou W., Van Eldere J., van Steenberghe D. "The influence of Titanium Abutment Surface Roughness on Plaque Accumulation and Gingivitis: Short Term Observations." *Int. Journal of Oral & Maxillofacial Implant*. Vol. 11, 1996, p. 69-178.

[25] Jimbo R., Ivarsson M., Koskela A., Sul Y.T., Johansson C.B. "Protein Adsorption to Surface Chemistry and Crystal Structure Modification of Titanium Surfaces." *Journal of Oral & Maxillofacial Research.* Vol. 1(3), 2010, p.1-9.

[26] Coathup M.J., Blunn G.W., Mirhosseini N., Erskine K., Liu Z., Garrod D.R., Li L. "Controlled Laser Texturing of Titanium Results in Reliable Osteointegration." *Journal of Orthopaedic Research*. Vol. 35(4), 2017, p.820-828.

[27] Cheng Y., Feng G., Moraru C.I. "Micro- and Nanotopography Sensitive Bacterial Attachment Mechanisms: A Review." *Frontiers in Microbiology*. Vol. 10, 2019, 191.

5 Experimental

As described in the previous chapter, techniques for modifying surface topography are many and very different from each other. Standard surface modification methods, such as grit blasting, acid etching, and anodization, have the main limitation of obtaining not reproducible surfaces without an ordered pattern. On the other hand, laser or electron beam surface texturing methods provide reproducible patterns with well-defined geometry. In recent years, several studies have been conducted in order to develop a surface that ensures healthy and firm implant–connective tissue attachment and laser surface texturing turned out to be one of the most prominent techniques for enhancing cell adhesion and avoiding epithelial down-growth.

The experimental part of this thesis consists firstly of a laser surface texturing of pure titanium grade 2 and Ti6Al4V alloy samples at the Innovation & Development section of *Osai Automation Systems S.p.A*. Therefore, chemical, and mechanical analyses were carried out at Politecnico di Torino, and surface characterization techniques will be presented.

The biological characterizations and the analysis of the cellular and bacteria adhesions have been carried out at the Biomedical Materials Lab of the University of Piemonte Orientale.

5.1 Preparation of the samples

The specimens used for the experiment are square-shaped plates, of area approximately equal to 1 cm^2 and about 1 mm thick, half consisting of pure titanium grade 2 and the other half of Ti6Al4V alloy.

Plates were polished under water irrigation to avoid thermal or mechanical damage at 250 bpm rotation speed. SiC abrasive papers with a 320-4000 sequence have been used. The samples for laser treatment were mirror-polished with diamond suspensions of size 3 µm and 1 µm, whereas the suspensions were not used for untreated samples, as traces remained on the surface and potentially altered the results. We noticed this problem through an analysis of wettability, in fact, the contact angle of the untreated sample after applying suspensions was too low compared to the standards of titanium and alloy.

Finally, in order to remove all traces and to perform analysis correctly, specimens were washed by 5-minutes ultrasonic washing with acetone, and consequentially two 10-minutes ultrasonic washings with distilled water.

5.2 Laser surface texturing

As shown by previous studies [3,4], the use of the electron beam to characterize the surface topography of titanium and Ti6Al4V samples enables the creation of groove patterns, which lead to an excellent result from cell adhesion tests. Fibroblasts align along the grooves, whose optimal dimension is 10 µm, a width which is actually comparable with that of fibroblasts. Another unexpected result from those studies is the antibacterial property of the electron beam textured

surface, associated with the high density of grain boundaries, which is supposed to be the key aspect affecting bacteria adhesion and metabolism on the analyzed samples.

Following this line of study, the idea was to try to reproduce a similar surface treatment using a laser beam instead of an electron beam, with the aim of comparing the results. The laser system has easier availability compared to electron beam machines, and also it generates a very different surface characterized by periodic microstructures called Laser Induced Periodic Surface Structures (LIPSS). Understanding if the cellular response improves or worsens in one case or another is of crucial concern, together with the analysis of the differences between the techniques.

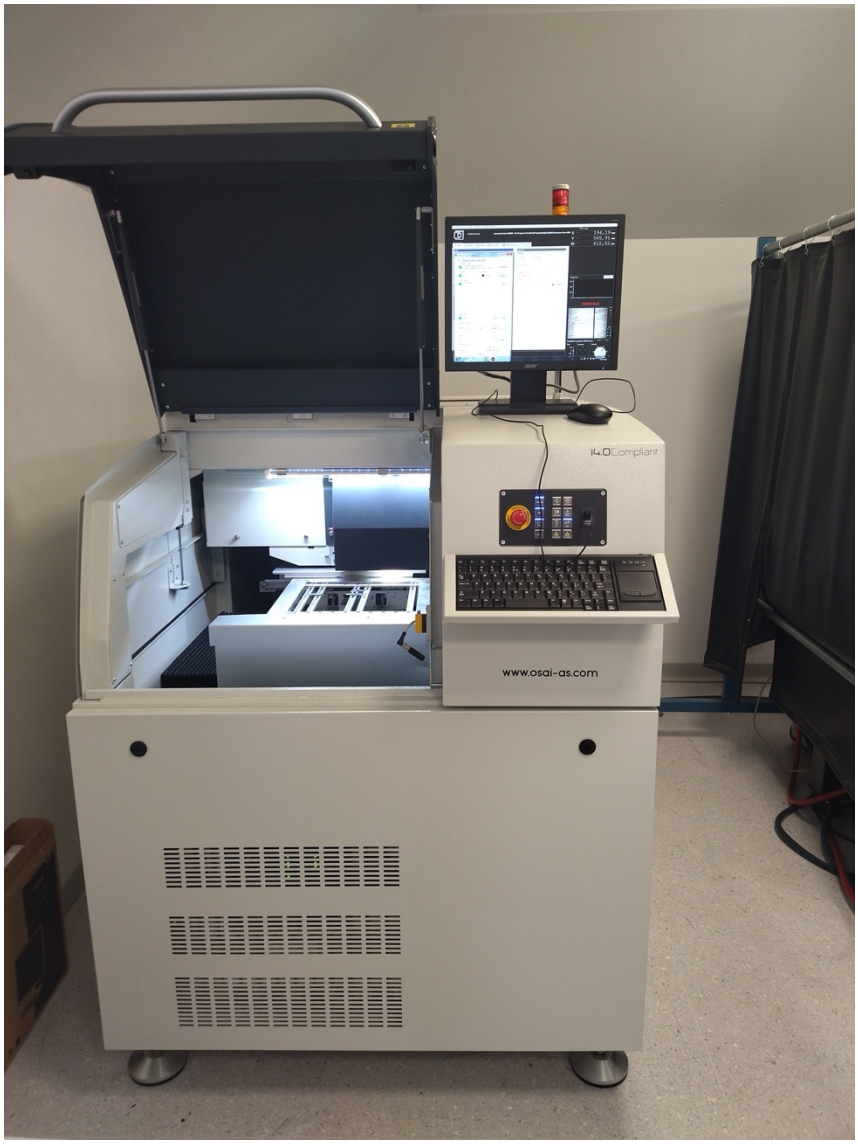

Figure 5-1. HyperRapid NX high-power picosecond laser system (Coherent, Germany) used for the experiment.

To carry out the laser surface treatment for the purpose of the experiment linked to this thesis a high-power picosecond laser system (*HyperRapid NX* model, *Coherent*, Germany), illustrated in *Fig. 5 – 1*, from the Innovation & Development section of *Osai Automation Systems S.p.A.* was used. This laser system is normally used for industrial applications, such as cutting and drilling of glass, sapphire, ceramics and metals, micromachining, and structuring of large surfaces with line focusing

or multiple beams [1], while for the aim of this thesis it was used for a new application, namely the surface micro-texturing of titanium and Ti6Al4V specimens with an area of 1 cm^2.

According to the manufacturer, the main specifications of the *HyperRapid NX* Laser System are given in *Table 5.1* [1].

Table 5-1. Specification of the HyperRapid NX picosecond laser system at lowest amplifier pulse repetition rate and for a single-pulse operation (burst number = 1).

HyperRapid NX model	
Single wavelength output λ	1064 nm
Output pulse repetition rate range	0-1000 kHz
Average Maximum Power P	50 W (at 500kHz)
Pulse duration τ	9-15 ps
Maximum Pulse Energy	220 µJ
Direction of polarization	Vertical

The laser parameters are of primary importance in determining the texture of the surface, which modifies a lot even slightly changing a single variable. The final set-up chosen for the experiment was obtained after several experimental tests, which led to what seemed to be the most suitable solution for our purposes. Initially, in fact, the first tests were carried out at a greater focal distance (7 mm), with a greater lateral displacement of 0.03 mm, but no evident grooves of the desired size were obtained since the surface was only partially melted. At shorter focal lengths or by increasing the number of repetitions, the grooves were deeper and more pronounced, but the roughness was greater than 0.2 µm.

A focal distance of 4 mm, a single loop repetition, and a lateral displacement, or hatch spacing, that is the distance between the center of the lines of two consecutive laser scans of 0.01 mm were chosen as the best compromise to achieve a non-excessive roughness but grooves that are evident and approximately 15 µm in size. The ideal size of the grooves should be approximately 10 µm, comparable to that of the fibroblasts so that they can "comfortably" line up along the grooves [3].

The applied parameters used for the experiment are listed in *Table 5 – 2* and a schematic illustration of laser textured samples is shown in *Fig. 5 – 2 a)*.

Table 5-2. Laser processing parameters selected used for the surface texturing of the titanium and Ti6Al4V samples.

Hatch spacing (h)	0.01 mm
Focal distance (df)	4 mm
Number of repetitions (N)	1
Frequency (f)	500 kHz
Selected Power (P)	20 W (about 50% of the power at 500 kHz)
Scanning speed (v)	1000 mm/s
Processing atmosphere	Ambient atmosphere (air)

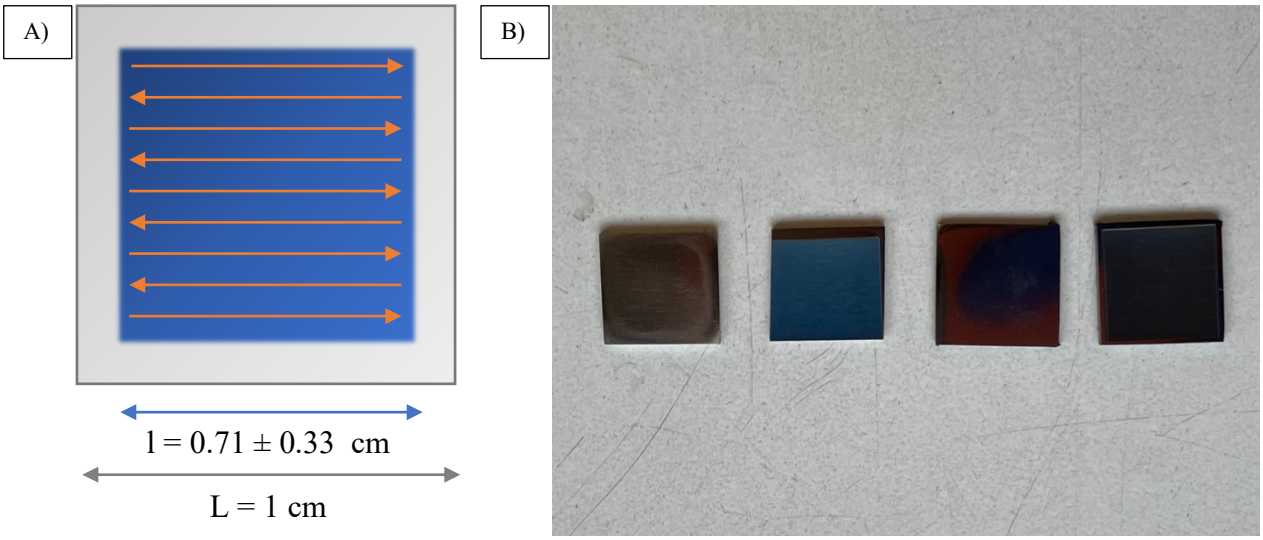

Figure 5-2. A) Schematic illustration of a laser textured sample. The plate is a square with an area of about 1 cm²; the treated area is shown in blue, with a side of approximately 0.7 - 0.8 cm; the orange arrows indicate the direction of application of the laser, which changes direction for each groove it makes. B) From the left to the right: Ti-cp grade 2 polished sample, Ti-cp grade 2 laser treated sample, Ti6Al4V polished sample, Ti6Al4V laser treated sample.

5.3 Materials and methods for surface characterization

5.3.1 Surface Topography (Confocal Microscopy and Contact Profilometer)

The textured surfaces were characterized in terms of topography, chemical composition, and crystallographic structure. The surface topography was characterized by confocal microscopy (*Zeiss LSM 900, Oberkochen*, *Germany*, 50x/0.95 objective).

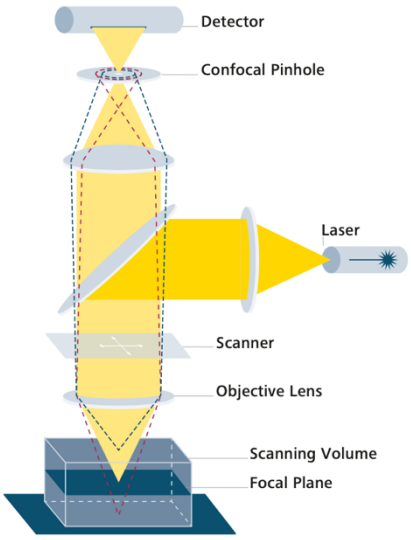

Figure 5-3. Schematic of confocal principle. In-focus information (yellow). Out of focus information (red and blue dotted lines). [6]

The confocal microscopy technique delineates the 3D microstructures and surfaces of samples, combining all essential light microscopy contrasting methods with high precision topography. The image is generated through recombination of images obtained by scanning in the x, y-direction and

changing the focus, thus the sample is optically sectioned. In *Fig. 5 – 3* the main parts of the confocal microscopy used in the experiment are shown.

Confocal microscopy permits both the characterization of material properties and the surface roughness analysis in accordance with international standards e.g. ISO 25178.

ISO 25178 Surface Texture is a collection of international standards relating to the analysis of surface roughness. It supports two evaluation methods: the contact type (stylus method) and the non-contact type (optical probe). With confocal microscopy we calculate the height parameters described below, which focus on the displacement of the evaluation area. [7]

The arithmetical mean height (Sa) is the difference in height of each point compared to the mean plane of the surface within the defined area. [7] This parameter is generally used to evaluate surface roughness and it's the most commonly used and it is calculated as in equation (1).

$$Sa = \frac{1}{A}\iint_A |Z(x,y)|dxdy \tag{1}$$

Where: A – the definition area; Z – surface height in position x, y; x, y – lengths in perpendicular directions.

However, there are several problems with using a single parameter to describe the 3D topography of a surface, since a single value is not very informative. Sa is unable to describe lateral roughness and to distinguish between peaks and valleys. Additional parameters should be used, such as Sq, Ssk, and Sku.

Sq, calculated in equation (2), represents the root mean square value of ordinate values within the defined area. [7]

$$Sq = \sqrt{\frac{1}{A}\iint_A Z^2(x,y)dx\,dy} \tag{2}$$

Sp is the maximum peak height and Sv is the maximum valley depth. The maximum height of surface Sz is the sum of the maximum peak height Sp and maximum valley depth Sv. [7] Sa, Sq, Sp, Sv, and Sz characterize the surface amplitude.

Ssk and Sku characterize the aspect of the texture height distribution. The skewness (Ssk) is the degree of bias of the roughness shape (asperity), which means it indicates whether the surface is composed mainly of peats or spikes. As shown in *Fig. 5 – 4*, if Ssk < 0, the height distribution is skewed above the mean plane, and oppositely if the skewness is positive the height distribution is skewed below the mean plane. Negative skewness is characteristic of stratified surfaces and porous material.

The kurtosis (Sku) represents the measure of the sharpness of the roughness profile. If Sku is lower than 3, the peaks have a flatter and rounder shape, while they are more pointed if Sku is greater than 3.

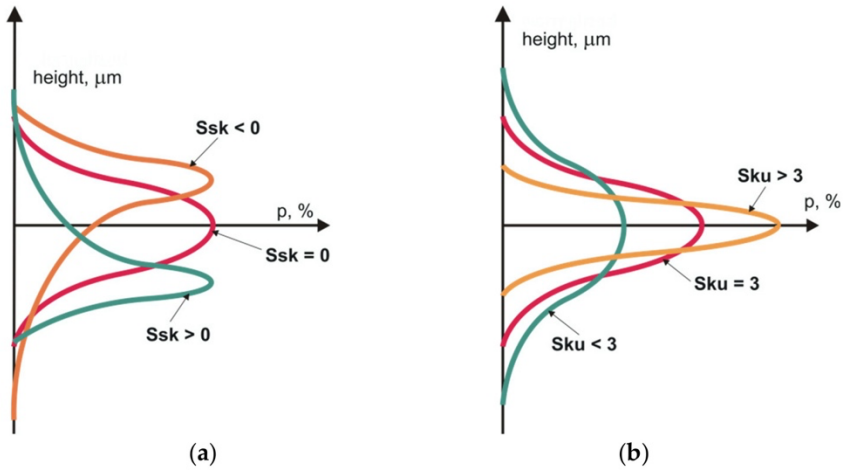

Figure 5-4. Skewness Ssk (a) and kurtosis Sku (b) of surface texture ordinate distribution. [8]

The parameters described above relate to roughness in an area, while the equivalent parameters for evaluating roughness along a line are referred to as Ra, Rq, Rp, Rv, Rz, Rsk, and Rsku. In order to calculate the roughness profile, ISO 4287 is used.

Moreover, roughness along a line was measured by a contact profilometer (*Intra Touch, Taylor Hobson, Leicester, United Kingdom*) making three different measurements per sample with a length of 3 mm. With the contact profilometer, we took three more measurements on the polished samples to compare the treated and untreated surfaces. Measurements were made in the major roughness direction, that is the one perpendicular to the grooves.

5.3.2 Chemical characterization (SEM, FESEM)

Surface morphology was analyzed qualitatively and chemically with Scanning Electron Microscopy and Energy Dispersive Spectroscopy, which perform in conjunction (SEM-EDS – *SEM, JEOL, JCM 6000 plus, EDS, JEOL, JED 2300*). SEM technology evaluates surface topography, whereas EDS provides elemental information about the semi-quantitative composition of the structure of the surface of a sample.

Titanium is a highly reactive metal, which reacts with oxygen by simply exposure to air. The surface treatment causes rearranging and modification of the existent oxide layer, and it is important to evaluate it because the presence of a TiO_2 layer suggests higher biocompatibility and corrosion resistance. Furthermore, it supports the incorporation of mineral ions such as calcium phosphate and water, promoting the mineralization of the surface.

Surface topography at the nanoscale was investigated by Field Emission Scanning Electron Microscopy (FESEM – *SUPRA™ 40, Zeiss*) to three-dimensionally highlight the structures that have formed on the surface by laser scanning.

5.3.3 Crystallographic characterization

The crystallographic structure was investigated by X-Ray Diffraction (XRD – *PANalytical X'Pert Pro PW 3040160 Philips, Malvern Panalytical, Egham, United Kingdom*) and the spectra were analyzed by *XPERT High Score* software.

5.3.4 Microstructure analysis

Two laser-treated samples were vertically embedded in resin. In this way, it was possible to mirror polish the cross surface of the specimens with SiC abrasive papers with a 320-4000 sequence and with diamond suspensions of sizes 3 µm and 1 µm.

Then, to assess the change in microstructure consequent to the laser treatment, acid etching was performed on the cross surface by rubbing the surface with a Kroll's solution (composed of 100ml of water, 1ml of HF, and 2ml of HNO_3) for 40s. The cross surfaces of the samples were observed by SEM and optical microscopy.

5.3.5 Wettability

Surface roughness has a great influence on surface wettability, which can play an important role not only in protein absorption but also in cell adhesion and spreading.

Surface wettability was evaluated using the sessile drop method through contact angle measurements (*DSA-100, KRÜSS GmbH, Hamburg, Germany*). The measurements were performed using a 5µm drop of ultrapure water as a wetting fluid at room temperature. If the contact angle is greater than 90°, the surface is hydrophobic, while if it is less than 90°, the surface is hydrophilic (*Fig. 5 – 5*).

Contact angle measurements on the first batch of untextured samples were found to be too low compared to the titanium standard values, in fact, the water drop spread excessively on the surface. The significant hydrophilicity found was thought to be caused by the use of diamond suspensions applied after polishing. For that reason, those samples were discarded, and new specimens, polished with the same abrasive papers as the previous ones, were obtained again, but suspensions were not used anymore. Wettability was, therefore, more consistent with the expected values.

The contact angle was calculated as the sum of the average value and the standard deviation (equation (3)), which were calculated using at least three measurements.

$$\theta_{contact} = mean \pm standard\ deviation = \frac{\sum_{i=1}^{n} \theta_i}{n} \pm \sigma \qquad (3)$$

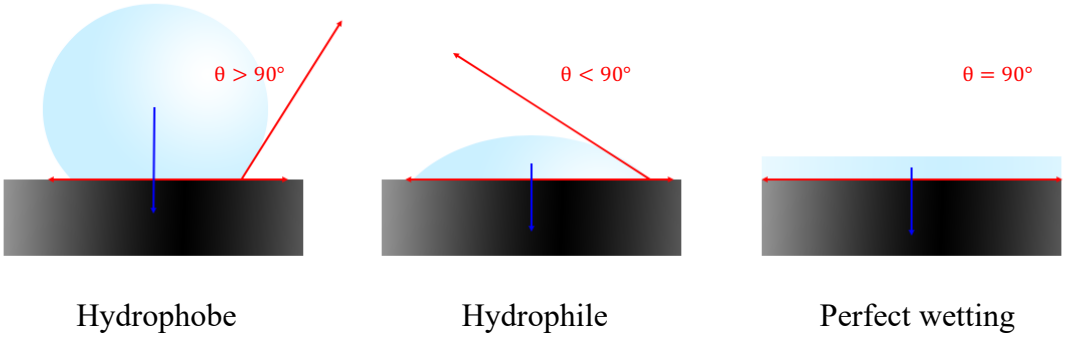

Figure 5-5. Example of contact angle measurement.

5.3.6 Zeta potential

The zeta potential describes the charging behavior at interfaces. The surface charge is established on the surface of a solid material in contact with a water-based fluid, and it determines the behavior of the material where aqueous systems play a role, such as biomedical implants in contact with body fluids. The zeta potential, also known as electrokinetic potential, is relevant not only to analyzing solid-liquid interfaces, but also to understanding the stabilization of emulsions (liquid-liquid interfaces) and foams (liquid-gas interfaces).

As shown in *Fig. 5 – 6*, the zeta potential is walked through the electrochemical double layer (EDL) model. When a solid surface is placed in a liquid solution, a surface charge is formed. The charged surface generates a charge of the opposite sign to the solid-liquid interface, which is different from the charge in the rest of the liquid.

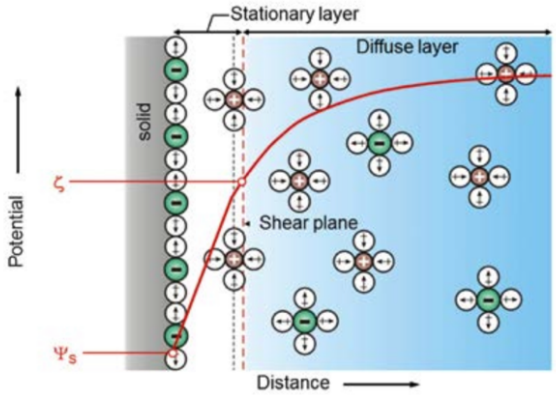

Figure 5-6. Model of the electrochemical double layer (EDL) at the solid-liquid interface. [5]

The charge difference between the solid surface and the interface, and then between the interface and the rest of the liquid results in the formation of a potential, which decays with increasing distance from the solid surface. In *Fig. 5 – 6*, Ψ_s indicates the surface potential, while ζ is the zeta potential. The shear plane splits the stationary layer from the diffusive layer and indicates the location of slipping of the moving liquid phase relative to the stationary liquid phase during the electrokinetic measurement. In the first layer, the potential assumes linear behavior, whereas in the latter it tends to

decay. The zeta potential is defined as the potential outside the stationary layer, meaning that it is calculated as the potential on the shear plane.

The surface charge at the interface between a solid surface and an aqueous solution is originated by two major mechanisms: (1) acid-base reactions of surface functional groups and (2) adsorption of ions. Both processes depend on the pH of the aqueous solution, therefore pH is the most important parameter of the liquid phase that affects the zeta potential. [5]

A diagram of the instrument used for the zeta potential measure (*SurPASS, Anton Paar GmbH*, Austria) is shown in *Fig. 5 – 7*.

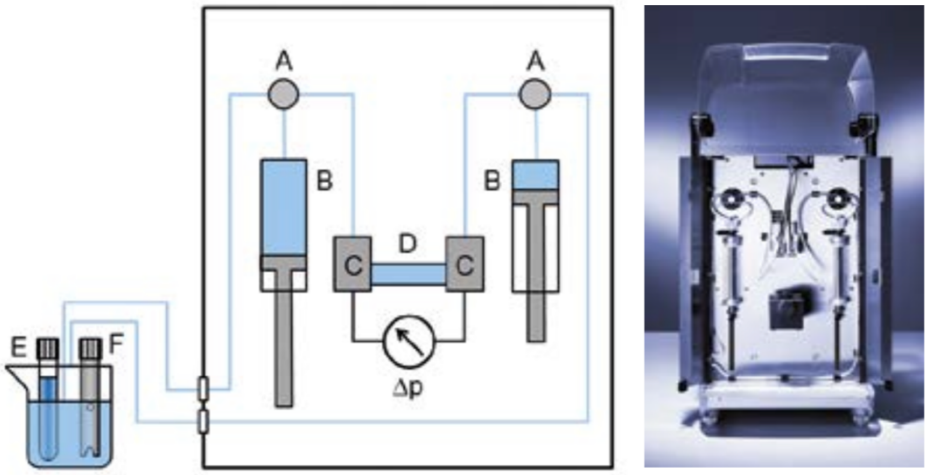

Figure 5-7. Components of the SurPASS electrokinetic analyzer. [5]

The essential configuration of the streaming potential apparatus must include a measuring cell with an appropriate sample holder, electrodes for the streaming potential measurement (dc voltage), a corresponding voltmeter, and a container with measuring liquid that is connected to the measuring cell.

In addition to the streaming potential, the electric conductivity and pH of the aqueous solution must be measured separately. In order to determine the zeta potential correctly, calculating the flow rate is of the utmost importance.

A are 3-way valves, in B are the needles for electrolyte transport, pressure transducers and electrodes are in C, and D is the measuring cell. Out of the grounded metal cage, used to protect the setup from external electromagnetic fields, there are in E the pH electrode and in f the conductivity probe. [5]

The Helmholtz-Smoluchowski equation (4) is used to calculate the zeta potential of samples with a flat surface and known geometry. [5]

$$\zeta = \frac{dI_{str}}{d\Delta p} \times \frac{\eta}{\epsilon \times \epsilon_0} \times \frac{L}{A} \qquad (4)$$

Where:

- The streaming current coefficient $\frac{dI_{str}}{d\Delta p}$ is measured and related to the cell constant L/A.
- As shown in the schematic representation in *Fig. 5 – 8*, L, W and H are the length, width, and height of the streaming channel (the gap between adjacent solid samples). A is the cross section, $A = W \times H$.
- η, ϵ and ϵ_0 are respectively the viscosity, the dielectric coefficient of the electrolyte solution, and the dielectric coefficient of the vacuum.

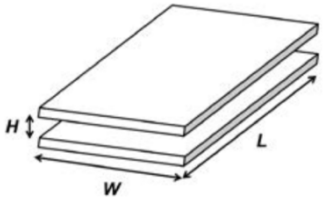

Figure 5-8. Schematic representation of the rectangular slit channel between adjacent solid samples with a planar surface. [5]

For zeta potential analysis of not regular-shaped samples, an approximation of the Helmholtz-Smoluchowski equation is applicable.

The zeta potential as a function of pH was analyzed by means of electrokinetic measurements (SurPASS, Anton Paar GmbH, Austria with an adjustable gap cell) in a dilute solution of KCl (0.001 M), which assumes the role of the electrolyte, with 0.05 M NaOH or 0.05 M HCl were used by the automatic titration unit to make measurements in the basic and acid field respectively.

First of all, the pH calibration was carried out using three buffers. Two laser-treated titanium samples, and subsequently, two laser-treated Ti6Al4V samples, were placed in the appropriate container. The same couples were used for the whole measurement, therefore, since the titanium reacts more in an acidic environment, we preferred to start from the measure in the basic field. Next, the circuit is filled with the electrolyte.

Zeta potential gives information about the solid surface charge. At neutral pH, the majority of materials assume a negative charge. We are also interested in the behavior of implants in case of deviation from neutral pH since the body pH shifts to the acid or basic fields under certain conditions. Moreover, the zeta potential in function of pH gives information about the functional groups present on the surface and on the stability of the surface at different pH.

The pH dependence of the zeta potential is directly related to the chemistry of surfaces. The isoelectric point, i.e. the pH where the zeta potential is zero, is another key parameter for biological processes that we get from the test. Besides, the pH dependence of the charging of solid-water interfaces offers information about solid surface hydrophilicity, material swelling, or buffer capacity for acids or bases. [5]

5.4 Material and methods for biological evaluation

The biological characterizations were carried out at the Biomedical Materials Lab of the University of Piemonte Orientale.

Specimens (1 cm side squares) were heat sterilized at 180°C for 1 hour in a dry oven. Afterward, they were stored at room temperature inside sterile Petri dishes to preserve the nanotextured surface until use.

5.4.1 In vitro cytocompatibility evaluation

5.4.1.1 Cells cultivation

Human fibroblasts were used to assay specimens' cytocompatibility. Cells were purchased from the American Type Culture Collection (*ATCC, VA, USA, CRL-4061*) and cultivated using the alpha-modified minimal essential medium (*α-MEM, from Sigma-Aldrich, Milan, Italy*) supplemented with 10% fetal bovine serum (*FBS, Lonza, Milan, Italy*) and 1% antibiotics (penicillin/streptomycin) at 37°C, 5% CO2. When cells reached 80-90% confluence, they were detached by trypsin/EDTA solution, collected, and used for experiments.

5.4.1.2 Direct Cytocompatibility

Sterile specimens were gently seeded to a new 12-multiwell plate by sterile tweezers avoiding any surface damage. Then, a defined number of cells (1x104 cells/specimens) were dropwise (100 µl) seeded directly onto the specimens' surface and allowed to adhere for 2 h at 37°C, 5% CO2. Afterward, each well was rinsed with 1 ml of fresh medium, and the cells were cultivated for 24-48-72 hours. At each time-point, specimens were first moved to a new multiwell plate, and then cell viability was verified by means of metabolic activity by the metabolic colorimetric Alamar blue assay (*alamarBlue®, ThermoFisher, Waltham, MA, USA*) following the manufacturer's instructions. Briefly, at each time-point, supernatants were removed from each well-containing cell and replaced with Alamar blue solution (10% v/v in fresh medium). Plates were incubated in the dark for 4 h and then 100 µl were removed, spotted into a new black 96-well plate and fluorescence signals were evaluated with a spectrophotometer (*Spark, from Tecan Trading AG, Switzerland*) using the following set-up: fluorescence excitation wavelength 570 nm, fluorescence emission reading 590 nm. As a control, the Alamar solution in contact with test materials solely (intended as cells-free) was applied and compared with the fluorescence of the same solution to exclude any reading background due to the reactive groups on the surface. Results were expressed as relative fluorescence units (RFU).

5.4.1.3 Morphological analysis

After 72 hours in culture the morphology of seeded cells was visually checked by immunofluorescent imaging (IF) and Scanning Electron Microscopy (SEM). For IF staining, cells were fixed at room temperature by Immunofix solution (*Bio Optica, Milan, Italy*) for 15min; then, they were washed 3 times with phalloidin (*ab176759, AbCam, Cambridge, UK*) and 4′ ,6-diamidino-2-phenylindole (*DAPI, Sigma-Aldrich, Milan, Italy*) to visualize cytoskeleton f-actin filaments and nuclei, respectively.

For SEM imaging, specimens were fixed overnight in 4% glutaraldehyde (from *Sigma-Aldrich, Milan, Italy*, 4°C, diluted in cacodylate buffer) and then dehydrated by the alcohol scale (50-70-90-100%, 1 h each). Then, samples were treated in hexamethyldisilazane (*Sigma-Aldrich, Milan, Italy*)

for 20 minutes at room temperature, mounted onto aluminum stubs with conductive carbon tape to undergo surface metallization by means of gold layer and observed with a *JSM-IT500* SEM using secondary electrons (from *Jeol S.P.A., Basiglio, Italy*).

5.4.2 In vitro antibacterial activity

5.4.2.1 Strain growth conditions

Specimens' antibacterial or antifouling properties were tested against the pathogen, strong biofilm former, multi-drug resistant strains *Staphylococcus aureus* (*S. aureus*, ATCC 43300). Bacteria were cultivated in Trypticase Soy Agar plates (*TSA, Sigma-Aldrich, Milan, Italy*) at 37°C until round single colonies were formed; then, 2–3 colonies were collected and spotted into 30 ml of Luria Bertani broth (*LB, Sigma-Aldrich, Milan, Italy*). Broth cultures were incubated overnight at 37°C in agitation (120 rpm in an orbital shaker), then bacteria concentration was adjusted to 1x105 cells/ml by diluting in fresh media until the optical density of 0.001 at 600 nm was reached as determined by spectrophotometer.

5.4.2.2 Antibacterial evaluation

Bacteria at the final concentration of 1x105/specimen were directly seeded onto the surface of the specimens and allowed growth for 24 hours at 37°C. Afterward, specimens were collected, carefully washed 3 times with sterile PBS to remove non-adherent cells, and seeded into a new plate.

The number of viable colonies adhered to specimens' surface was determined by the colony-forming unit (CFU) count; after 24 h of direct contact, specimens were moved to tubes containing 1ml of PBS, and the biofilm was detached from specimens by sonicator and vortex (30 seconds, 3 times each). Then, 100 µL of supernatant were collected from each tube and used to perform six serial 10-fold dilutions, by mixing 20 µL of bacterial suspension with 180 µL of sterile PBS. Twenty microliters were then collected from each dilution, spotted onto plates containing LB agar medium, and incubated for 24 h at 37°C. Lastly, the CFU/ml were counted as follows:

$$CFU = (number\ of\ colonies\ \times dilution\ factor)^{serial\ dilution} \quad (5)$$

Where:

- *Number of colonies* = countable single round colonies.
- *Dilution factor* = dilution made from the initial 1 mL suspension.
- *Serial dilution* = 1-6 10-fold dilution area where colonies were counted.

Finally, the morphology and the biofilm-like 3D structures of the adhered bacteria was investigated by SEM as previously described.

References

[1] https://www.coherent.com/content/dam/coherent/site/en/resources/datasheet/lasers/COHR_HyperRapidNX_DS_0718_2.pdf

[2] Yong J., Qing Y., Guo C., Chen F., Hou X. "A review of femtosecond laser-structured superhydrophobic or underwater superoleophobic porous surfaces/materials for efficient oil/water separation." *RSC Advanced*. Vol. 9, 2019, p. 12470-12495.

[3] Ferraris S., Warchomicka F., Ramskogler C., Tortello M., Cochis A., Scalia A., Gautier di Confiengo G., Keckes J., Spriano S. "Surface structuring by Electron Beam for improved soft tissues adhesion and reduced bacterial contamination on Ti-grade 2." *Journal of Material Processing Tech*. Vol. 266, 2019, p.518-529.

[4] Ferraris S., Warchomicka F., Iranshahi F., Rimondini L., Cochis A., Spriano S. "Electron beam structuring of Ti6Al4V: new insight on the material surface properties influencing the bacterial adhesion." *Materials*. Vol.13(2), 2020, p.409-420.

[5] Luxbacher T. "The ZETA Guide Principles of the Streaming Potential Technique." *Anton Paar*, Graz, 2014

[6] https://pages.zeiss.com/rs/896-XMS-794/images/ZEISS-Microscopy_Product-Brochure_ZEISS-LSM-900.pdf

[7] ISO 25178-2:2012 Geometrical Product Specifications (GPS) - Surface Texture: Areal - Part 2: Terms, Definitions and Surface Texture Parameters; International Organization for Standardization: Geneva, Switzerland, 2012. Available online: https://www.iso.org/standard/42785.html

[8] Pawlus P., Reizer R., Wieczorowski M. "Functional Importance of Surface Texture Parameters." *Materials.* Vol. 14, 2021, 5326.

[9] Voisey K.T., Scotchford C.A., Martin L., Gill H.S. "Effect of Q-switched laser surface texturing of titanium on osteoblast cell response." *Physics Procedia*. Vol. 56, 2014, p. 1126-1135.

6 Results

The typical diameter of a spread cell is approximately 15-20 µm, so it is desired that surface features have this size or smaller. Elongation of fibroblasts in the direction of the grooves has been widely reported [1][2][3]. The optimal width of the grooves obtained by laser texturing is less than 40 µm [1], and Ferraris et al. [2],[3] highlight in their studies the dependence of groove size on fibroblast alignment. Following this line of research, the final groove size desired in this experiment to maximize fibroblast adhesion is 10 µm and a roughness of 0.2 µm, which was studied to be the threshold below which bacterial proliferation does not increase [9],[10].

6.1 Preliminary analyses for the choice of experimental conditions

With the aim of obtaining grooves 10-20 µm thick and roughness of 0.2 µm, the final set of samples was produced by making several attempts.

The laser firstly draws the grooves in one direction, after which it moves vertically to draw the next groove in the opposite direction, as described in *Fig. 6 – 1*.

Figure 6-1.Direction of the laser beam. In green, laser on. In yellow, laser off.

A changing direction was chosen because, when the grooves are all made in the same direction, an area was observed where the surface is not uniform but appears to be re-melted.

All the laser surface treated specimens were produced with a frequency of 500kHz, a scanning speed of 1000 mm/s, and a power of about 20W.

From the first to the optimum condition, all samples are summarized in *Table 6-1*. Below, the discussion will continue by analyzing the different cases individually.

Table 6-1. Samples developed for the choice of the best conditions. Roughness values were evaluated through contact profilometer.

Name	Material	Focal distance	N° loops	Hatch spacing	Roughness (Ra)	Grooves dimension
L1-Ti-cp	Pure titanium grade 2	7 mm	3	0.2 mm	248 ± 64 nm	~ 80 µm
L2-Ti-cp	Pure titanium grade 2	8 mm	3	0.2 mm	136 ± 76 nm	~ 130 µm
L3-Ti-cp	Pure titanium grade 2	9 mm	3	0.2 mm	120 ± 56 nm	~ 70 µm
L4-Ti-cp	Pure titanium grade 2	10 mm	3	0.2 mm	72 ± 21 nm	Not distinguishable
L5-Ti64	Ti6Al4V	7 mm	3	0.01 mm	117 ± 32 nm	Not distinguishable
L6-Ti-cp	Pure titanium grade 2	7 mm	1	0.03 mm	169 ± 65 nm	Not distinguishable

L7-Ti64	Ti6Al4V	4 mm	1	0.03 mm	203.5 ± 102 nm	18 ± 2.8 µm
L8-Ti-cp	Pure titanium grade 2	4 mm	1	0.03 mm	176 ± 52 nm	12.98 ± 3.6 µm
L9-Ti-cp	Pure titanium grade 2	0 mm	1	0.03 mm	160.5 ± 2 nm	15.4 ± 3.9 µm
L10-Ti64	Ti6Al4V	4 mm	1	0.01 mm	0.198 ± 0.002 µm	13.7 ± 0,8 µm
L11-Ti-cp	Pure titanium grade 2	4 mm	1	0.01 mm	0.207 ± 0.007 µm	13.2 µm

The first tests L1-Ti-cp, L2-Ti-cp, L3-Ti-cp, and L4-Ti-cp were carried out respectively for focal lengths of 7, 8, 9, and 10 mm, 3 loops, and a hatch spacing of 0.2 mm. The starting conditions were taken from preliminary work carried out within a research group at Politecnico di Torino in collaboration with *Osai Automation Systems S.p.A*.

In all the cases, the grooves were more than 70 µm thick, but on the other hand, the most appropriate distance was found to be 7 mm, since in the other cases the total fusion of the treated area did not occur: in L2-Ti-cp, L3-Ti-cp, and L4-Ti-cp the areas dividing a groove and the consequent one were untreated and not melted, as highlighted in *Fig. 6-2*.

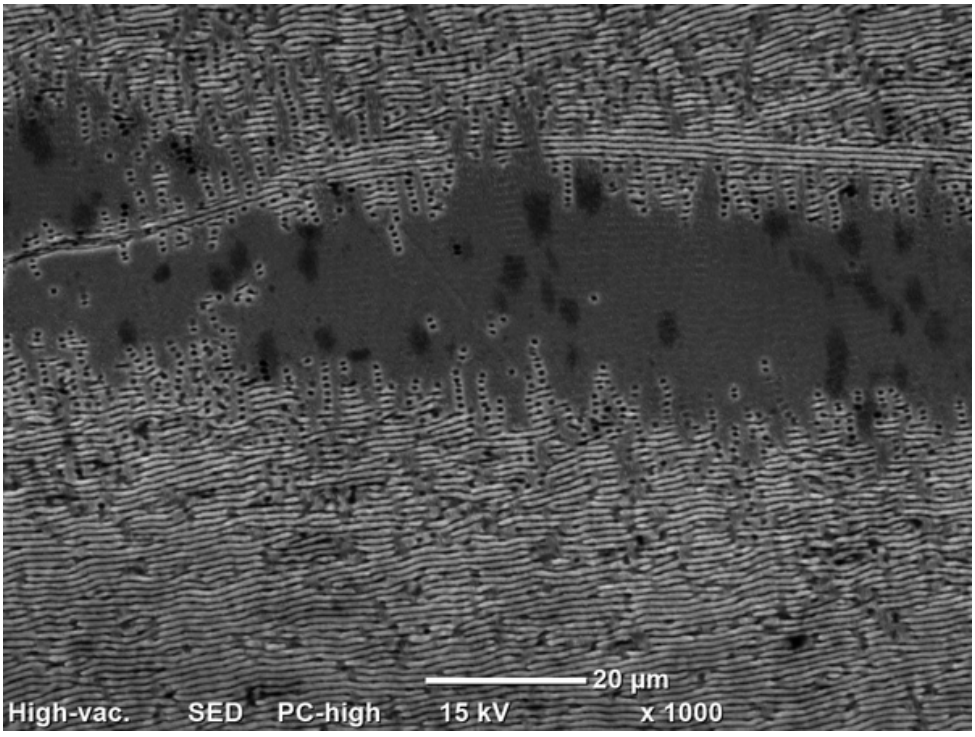

Figure 6-2. SEM image of L2-Ti-cp sample. A non-melted area is evident between two distinct zones where the treatment has produced the typical lamellar microstructure of the laser.

At 7 mm of focal distance, a lamellar topography at the micro-scale is observed (*Fig. 6 – 3*) and the area three times laser-treated and resolidified has a denser microstructure than the neighboring area. This resulted in the production of both high spatial frequency LIPSS (HSFL) and low special

frequency LIPSS (LSFL). *Fig. 6 – 3 A)* highlights the difference between the two structures. Furthermore, the roughness of L1-Ti-cp resulted very closed to the desired roughness of 0.2 µm. However, the grooves were still too wide, as shown in *Fig. 6 – 3 B)*.

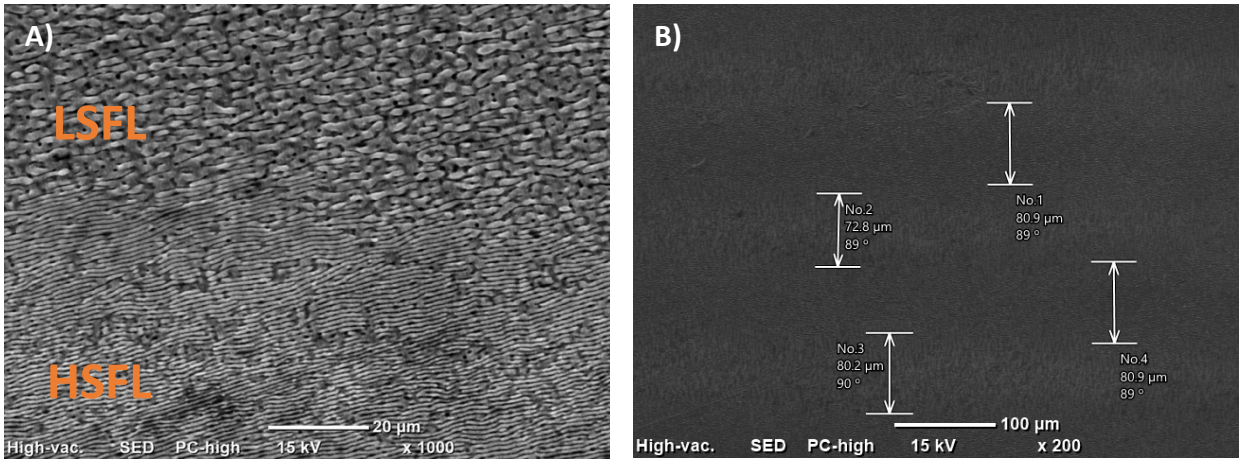

Figure 6-3. SEM microscopy of L1-Ti-cp. A) laser induced periodic surface structures (LIPSS) at 1000x. B) Grooves dimensions at 200x.

With the aim of producing grooves of lower thickness, a smaller hatch spacing of 0.01 mm was used in sample L5-Ti64, but grooves were still difficult to distinguish under both SEM, as illustrated in *Fig. 6 – 4*, and confocal microscopy.

Then, we tried to decrease the number of loops, which became only 1, and the focal distance, maintaining hatch spacing of 0.03 mm. Decreasing the number of loops necessarily involves bringing the beam origin closer to the surface, otherwise, the energy released is not sufficient to melt the surface, which remains partially unmelted. This occurred when the focal distance was still 7 mm and one laser loop in L6-Ti-cp, as shown in *Fig. 6 – 5*.

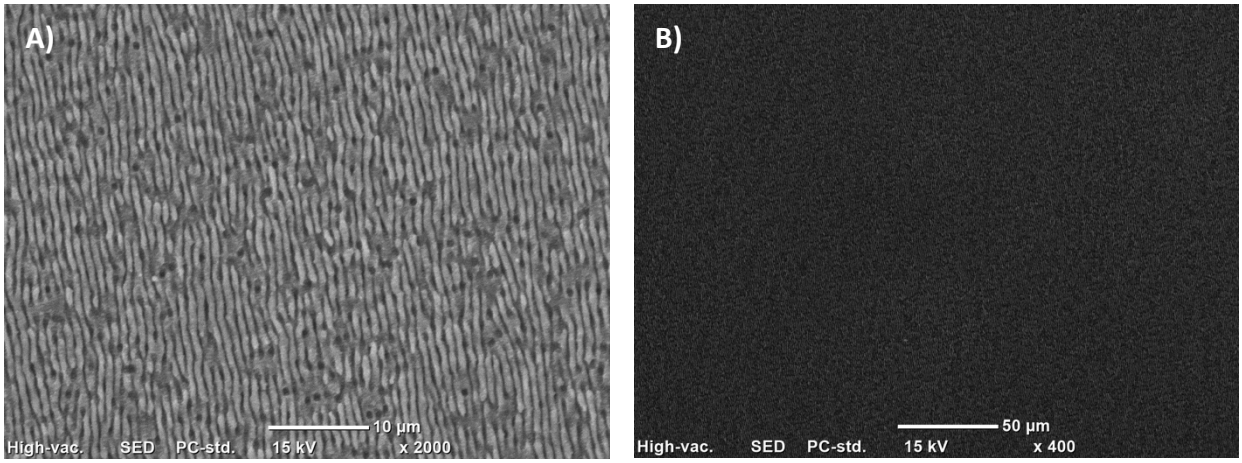

Figure 6-4. SEM microscopy of L5-Ti64 at different magnifications.

Bringing the laser beam origin closer to the surface, grooves are pronounced, as shown in *Fig. 6 – 6*. As expected, the dimension of the grooves in samples L7-Ti64, L8-Ti-cp, and L9-Ti-cp was between 10 and 20 µm, representing the ideal value we were trying to achieve. As well roughness resulted in acceptable values. In conclusion, a lower focal distance is necessary to produce grooves of the desired dimensions.

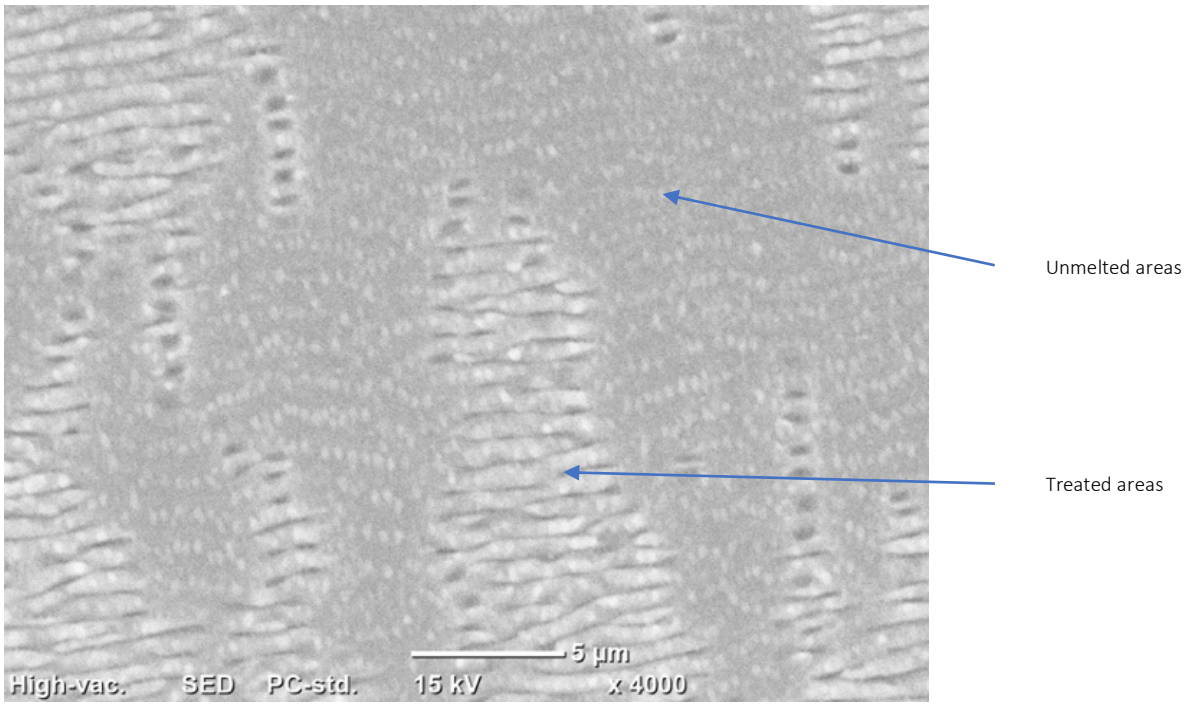

Figure 6-5. SEM microscopy L6-Ti-cp sample. Incompletely melted areas alternate with areas where treatment has taken place.

However, the sample L9-Ti-cp was rejected from the samples of interest because grooves were too pronounced. In addition, the procedure at a shorter focal length is more difficult to control: some areas are more likely to be fused than other on the same sample, leading to a non-uniform surface.

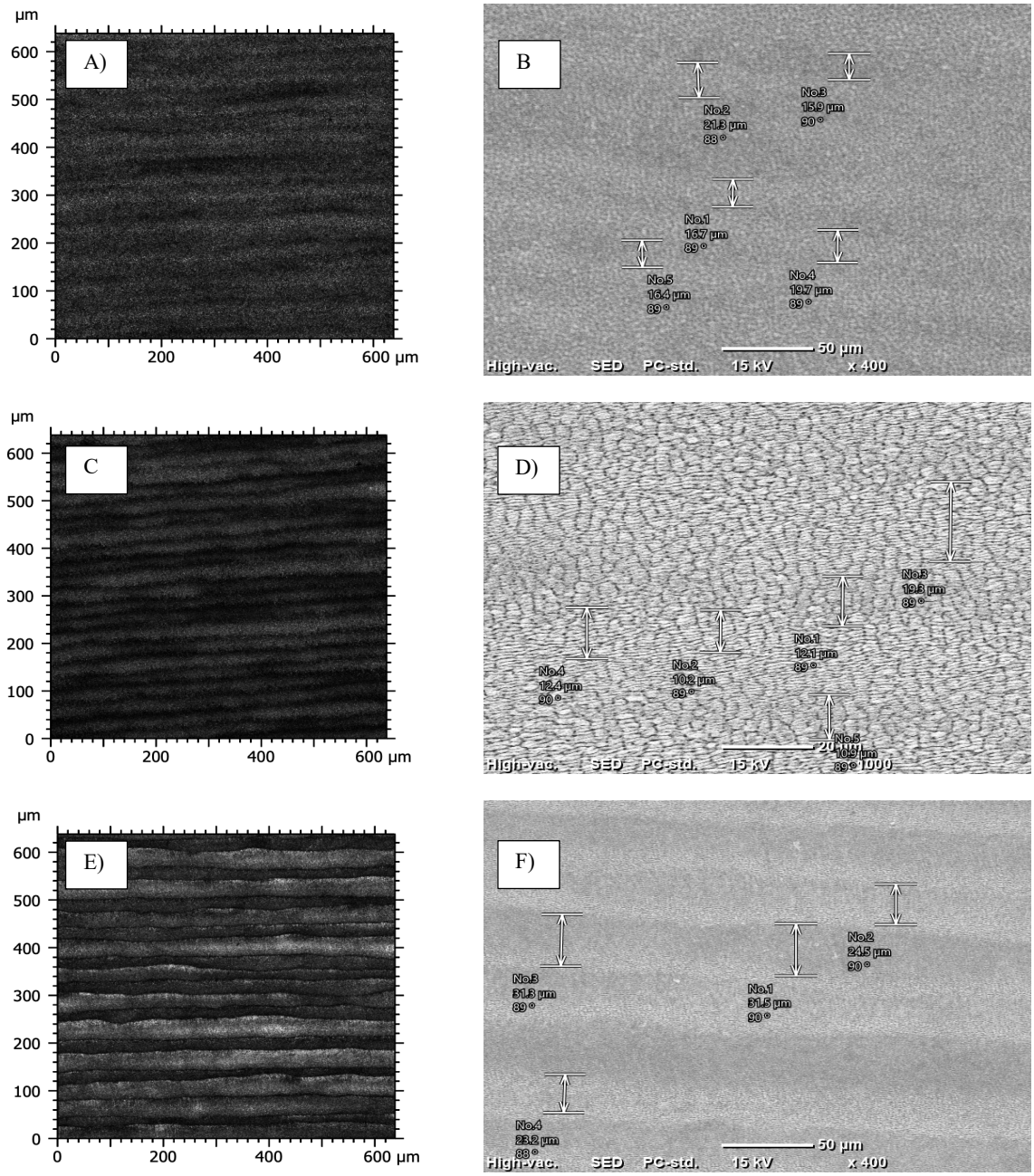

Figure 6-6. A) Confocal and B) SEM images of L7-Ti64. C) Confocal and D) SEM images of L8-Ti-cp. E) Confocal and F) SEM images of L9-Ti-cp.

Looking at samples L7-Ti64 and L8-Ti-cp, which were the most interesting in terms of size and depth of the grooves, and surface uniformity, we tried keeping constant the number of loops – 1 only – and the focal distance – 4 mm – constant, decreasing the hatch spacing to 0.01 mm. Samples L10-Ti64 and L11-Ti-cp were found, which turned out to be the best parameters for the development of the desired surface texture. Grooves size was between 10 and 15 µm, which is the most suitable dimension for fibroblast alignment, and the roughness was approximately 0.2 µm.

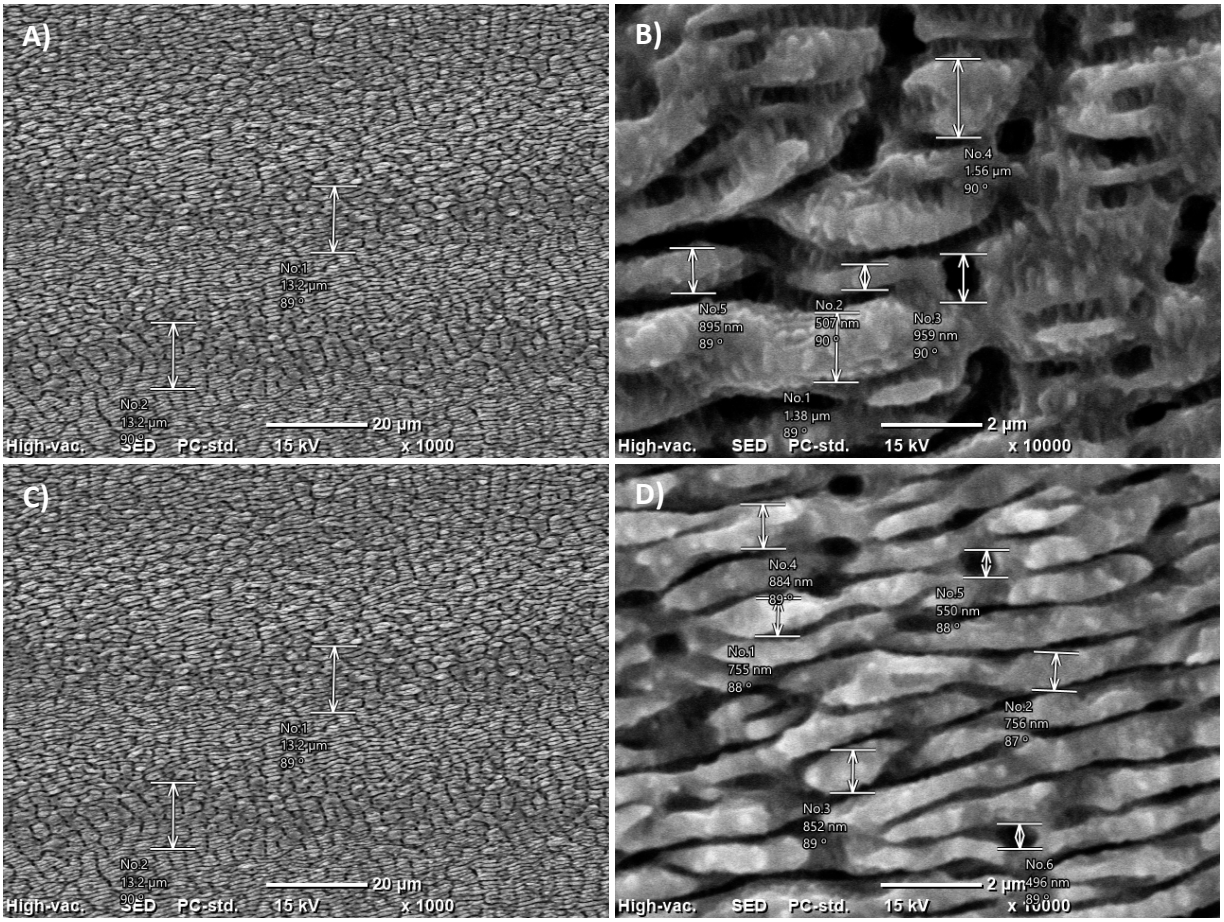

Figure 6-7. SEM microscopy of A) and B) L10-Ti64 sample at different magnifications. C) and D) L11-Ti-cp sample at different magnifications.

In conclusion, the final experimental conditions are listed in *Table 6 – 2*.

Table 6-2. Final laser parameters used for the experiment.

Lateral displacement (dl)	0.01 mm
Focal distance (df)	4 mm
Number of repetitions (N)	1
Frequency (f)	500 kHz
Selected Power (P)	20 W (about 50% of the power at 500 kHz)
Scanning speed (v)	1000 mm/s
Processing atmosphere	Ambient atmosphere (air)

6.2 Surface Morphology and Topography

6.2.1 SEM analysis

The names of the samples used for the experiment are listed in *Table 6 – 3*, where the conditions for obtaining laser structured samples are stated in *Table 6 – 2*. Mirror-polished samples were used as controls.

Table 6-3. Ti-cp and Ti64 samples names and processing.

Sample Name	Material	Processing
TicpMP	Pure Titanium Grade 2	Mirror polishing
Ti64MP	Ti6Al4V	Mirror polishing
TicpL	Pure Titanium Grade 2	Mirror polishing + Laser beam structuring
Ti64L	Ti6Al4V	Mirror polishing + Laser beam structuring

In order to observe the surface morphology, TicpL and Ti64L were observed by SEM.

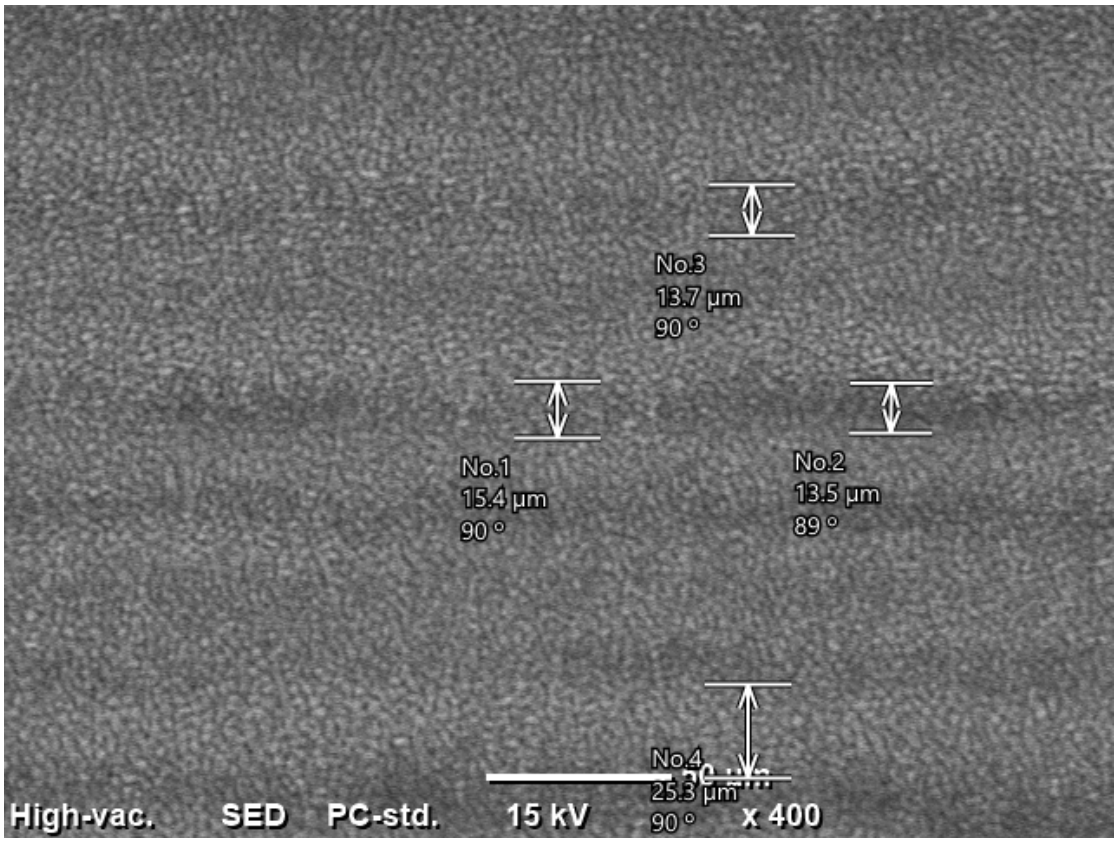

Figure 6-8. TicpL SEM image at 400x magnification.

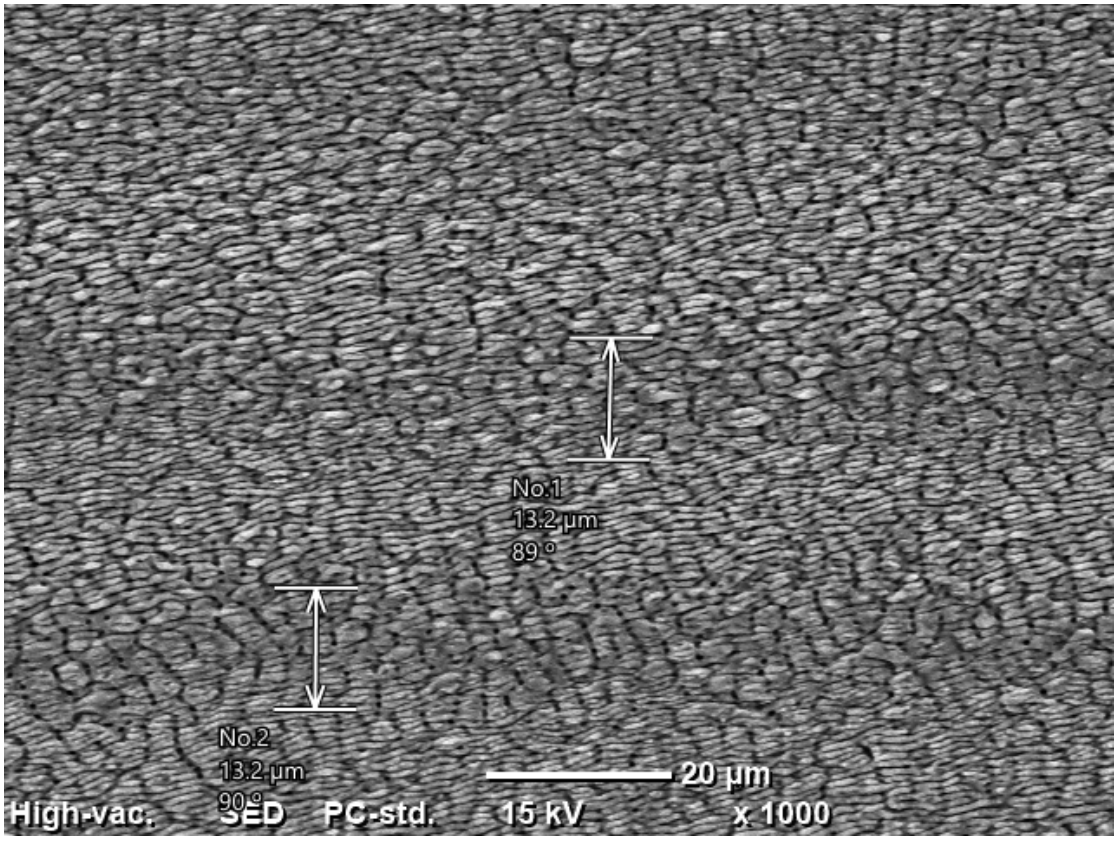

Figure 6-9. TicpL SEM image at 1000x magnification.

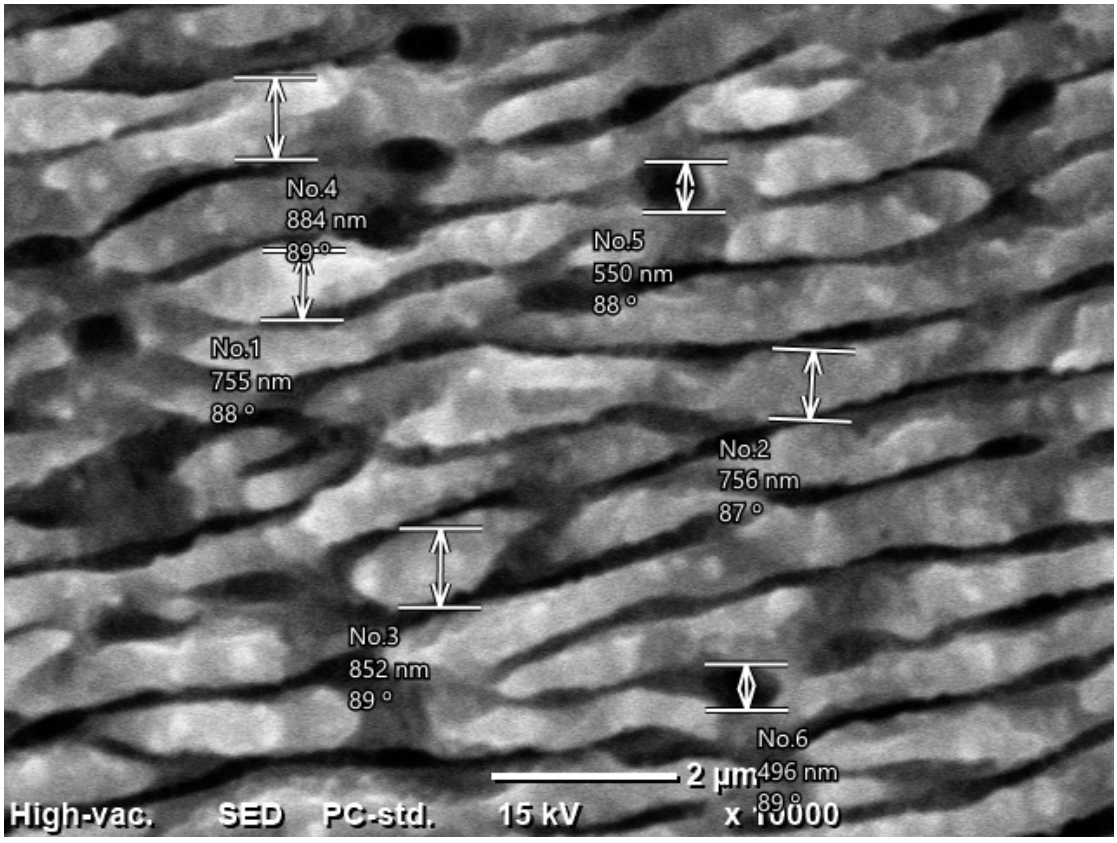

Figure 6-10. TicpL SEM image at 10000x magnification.

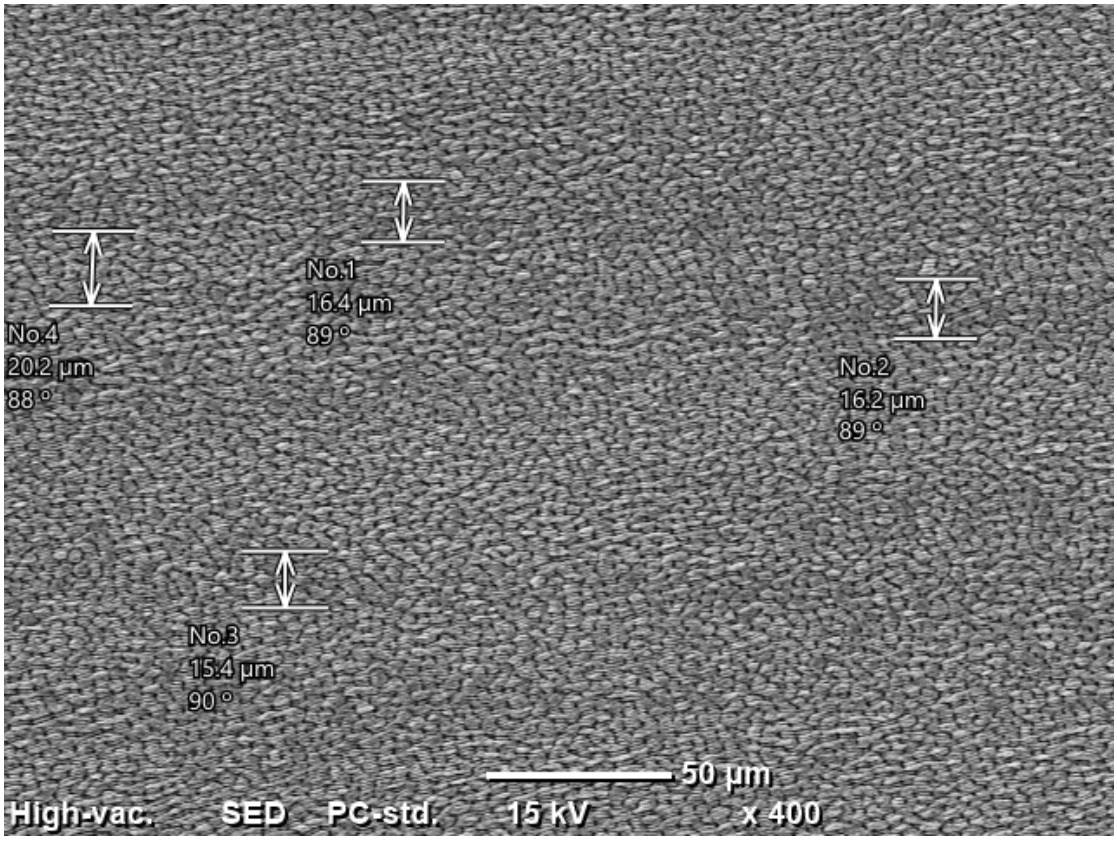

Figure 6-11. Ti64L SEM image at 400x magnification.

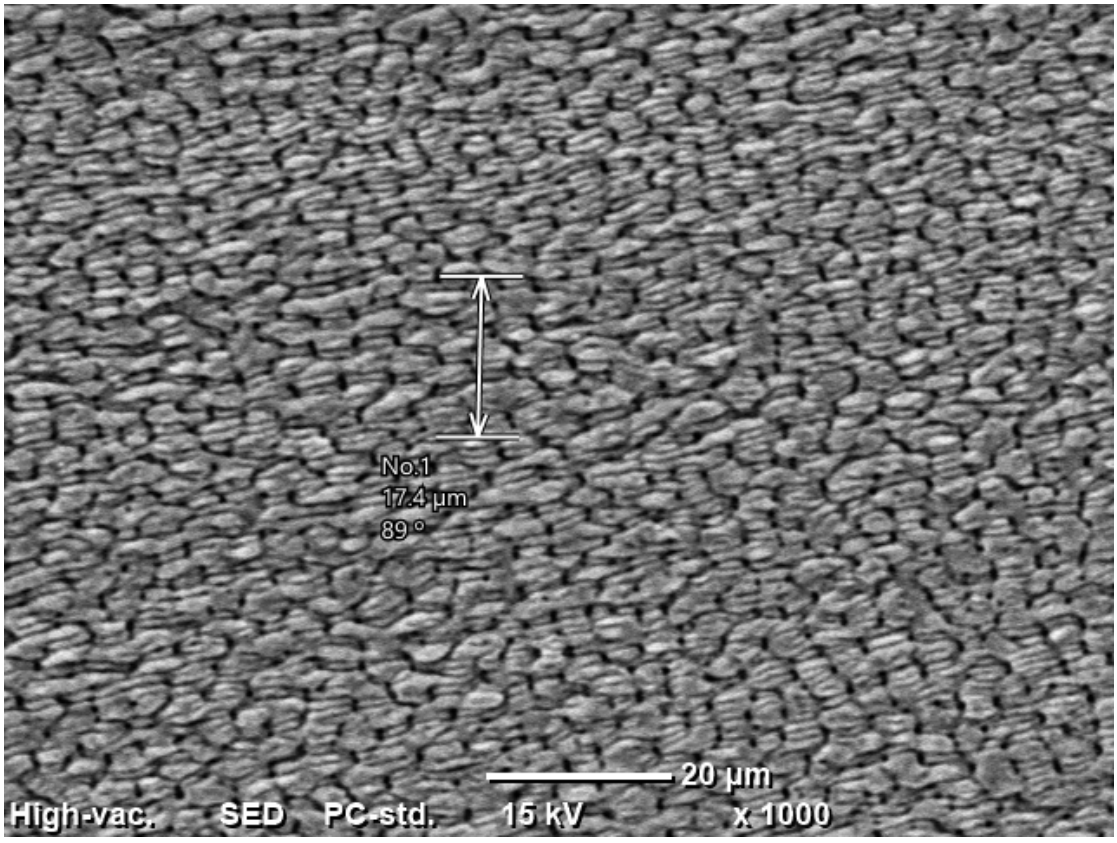

Figure 6-12. Ti64L SEM image at 1000x magnification.

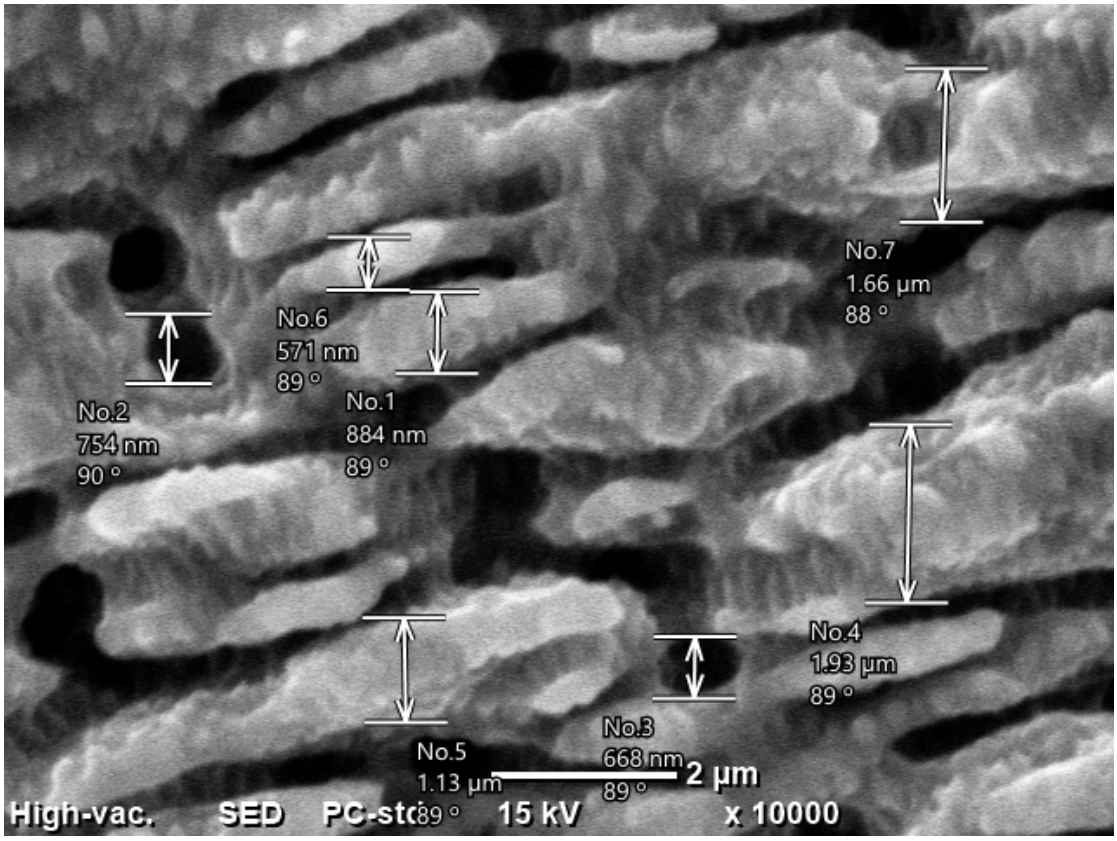

Figure 6-13. Ti64L SEM image at 10000x magnification.

As can be seen from *Fig. 6 – 8, 9, 11, and 12*, grooves are viewable and of an average width of 15.46 ± 2.23 µm. The main limit observed in the laser machine is that it is impossible to reach 10 µm width grooves or lower.

From the above images, it can be observed the typical lamellar topography produced by laser treatment. Laser-induced periodic surface structures (LIPSS), which alternate to holes with a diameter of 600-700 nm, characterizing the surface morphology at the nanoscale. In sample Ti64L, these structures are wider, averagely wide 1.235 ± 0.55 µm (Fig. 6 – 13), whereas in TicpL sample LIPSS are just over half as thick as the former, 0.811 ± 0.66 µm on average (Fig. 6 – 10). This different behavior is influenced by the material properties. The formation of LIPSS is based on the absorption of radiation by the electron system of the material hit by the laser beam, so it strictly depends on the type of material used.

6.2.2 FESEM microscopy

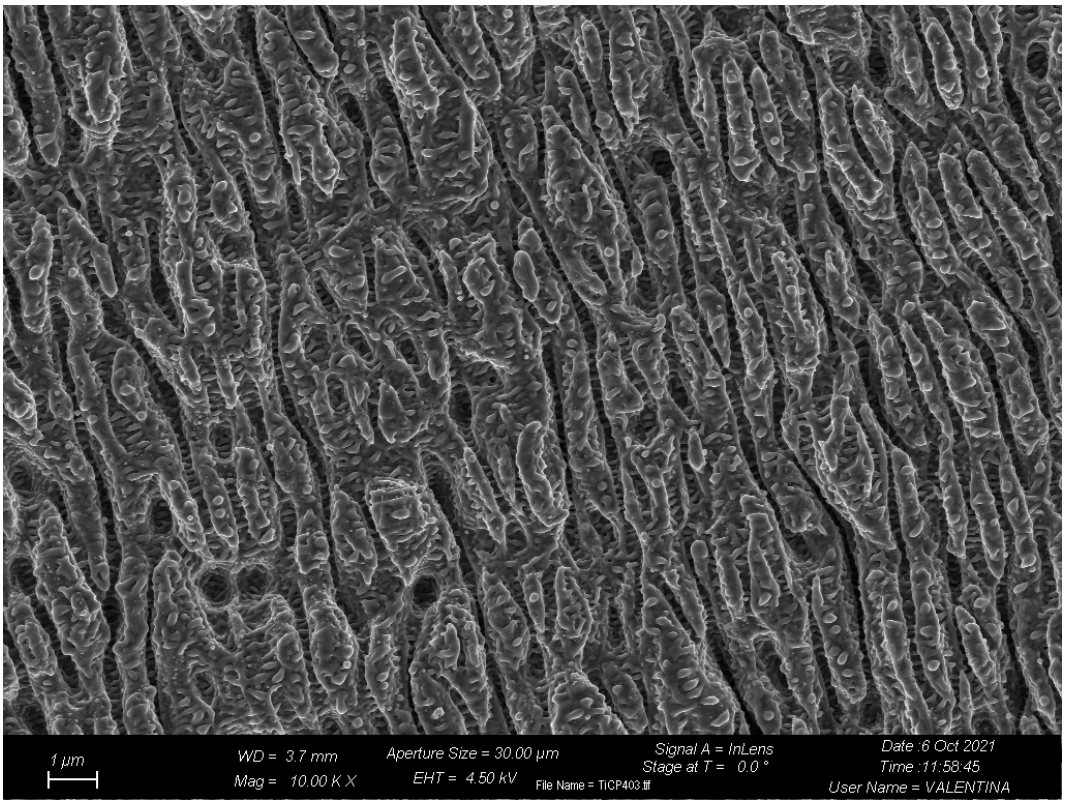

Figure 6-14. FESEM image of TicpL sample at 10000x magnification.

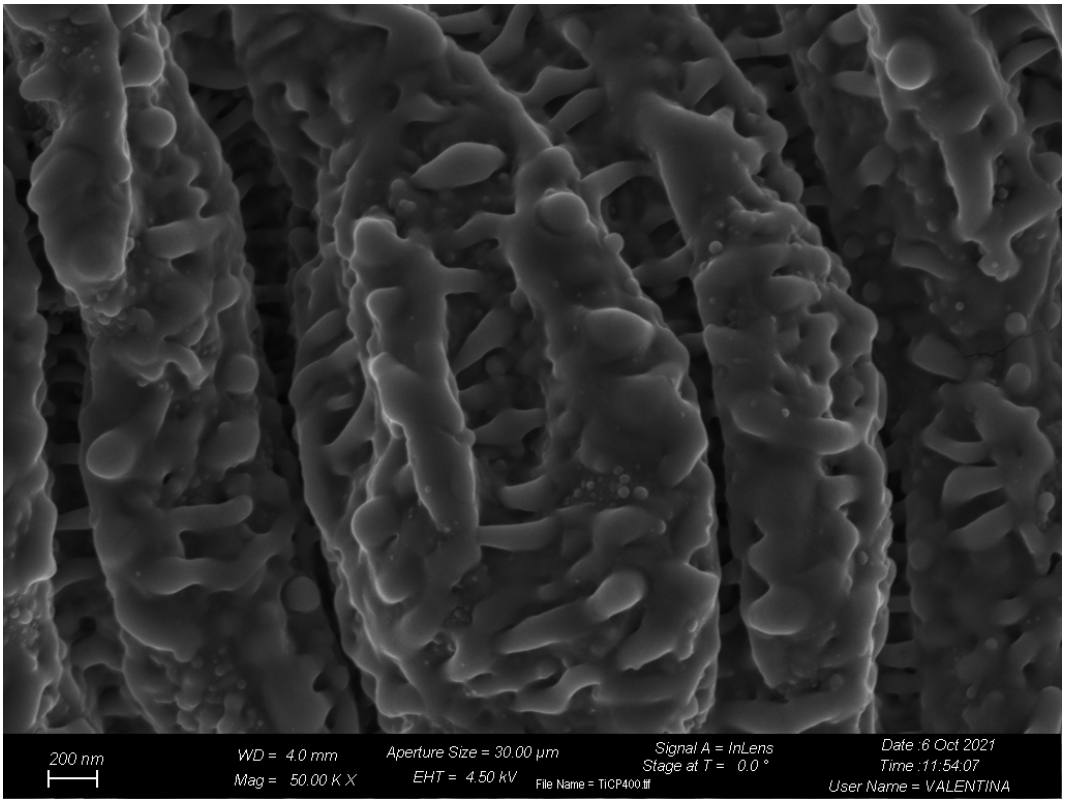

Figure 6-15. FESEM image of TicpL sample at 50000x magnification.

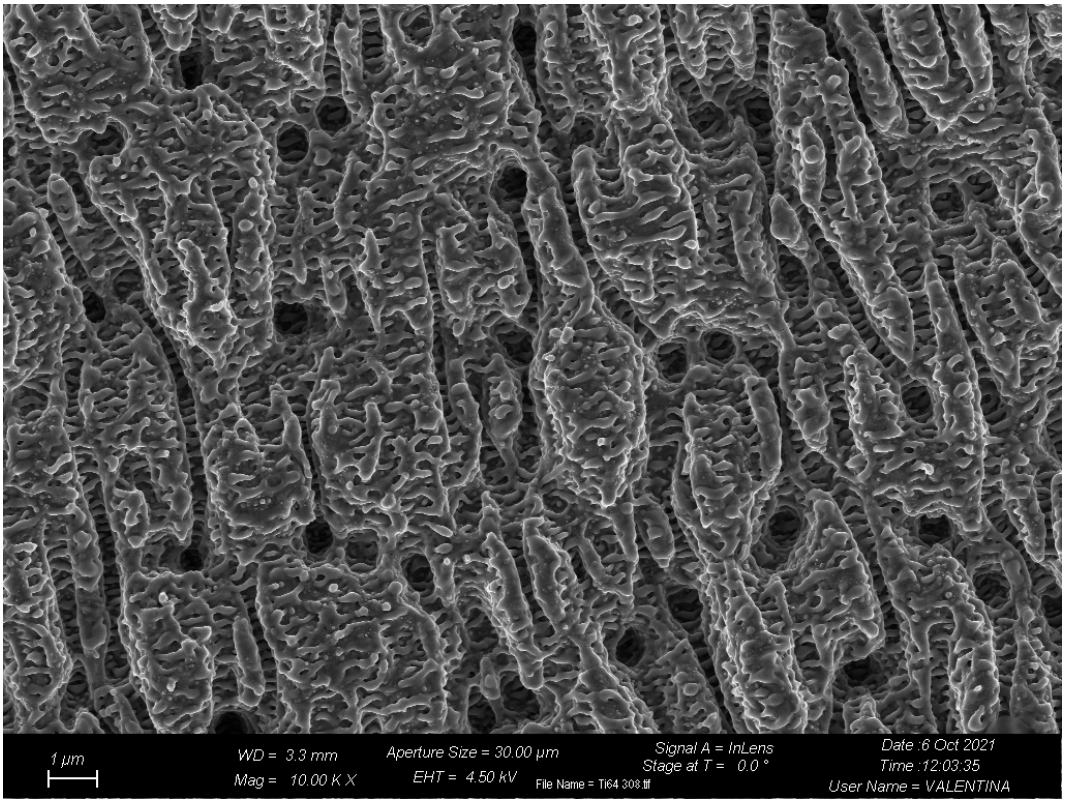

Figure 6-16. FESEM image of Ti64L sample at 10000x magnification.

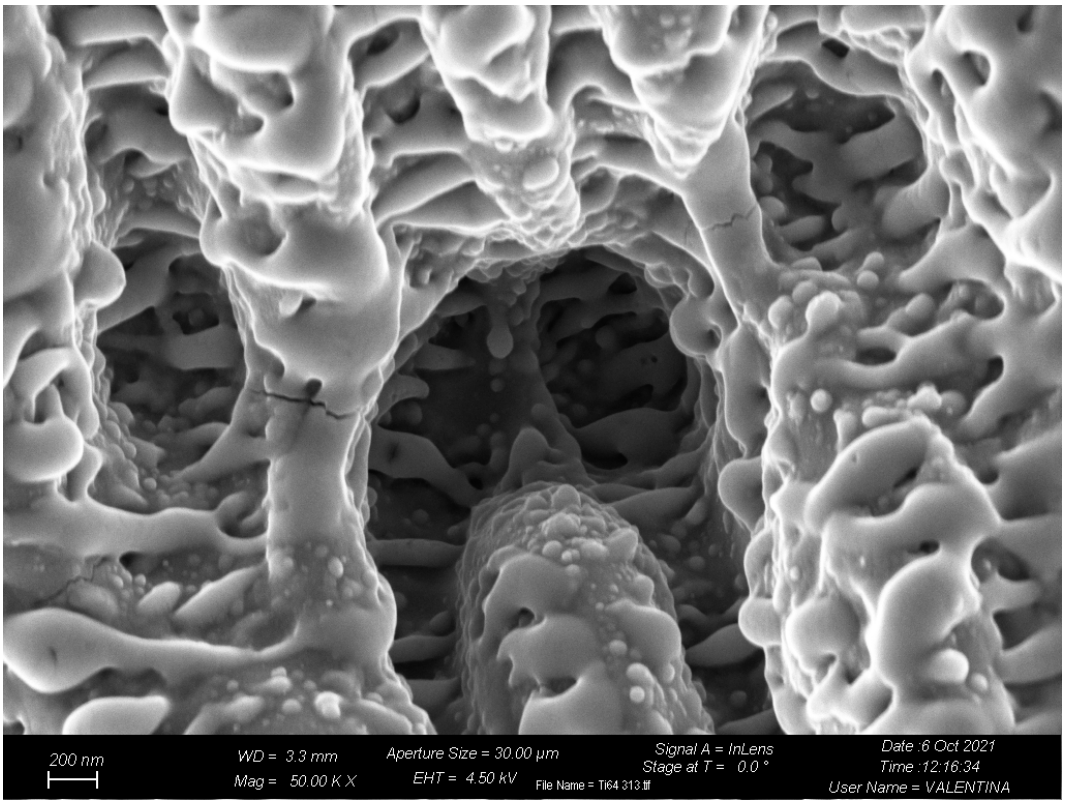

Figure 6-17. FESEM image of Ti64L sample at 50000x magnification.

Fig. 6 – 14, 15, 16 and 17 report FESEM images of the laser-treated surfaces for high magnification investigation of the surface topography. It can be observed that each lamella (micrometric scale)

presents smaller lamellae (at about 100 nm) and nanometric bubbles. As can be seen in *Fig. 6 – 14 and 16*, the only difference between the two materials appears to be the presence of more nanoholes in Ti64L with respect to TicpL.

6.2.3 Confocal microscopy and contact profilometer

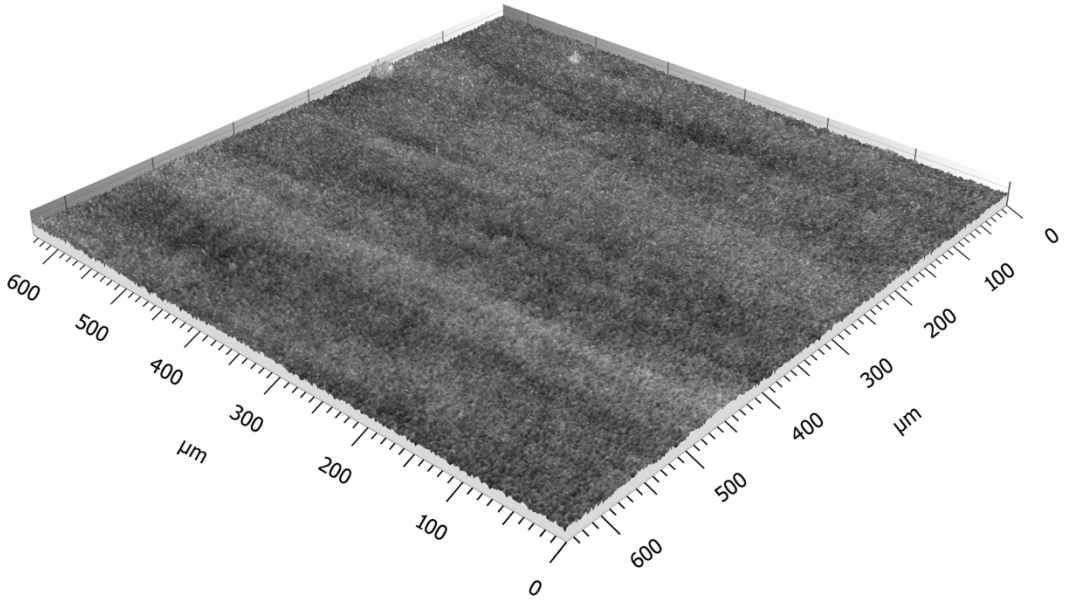

Figure 6-18. Confocal microscopy of TicpL at 20x.

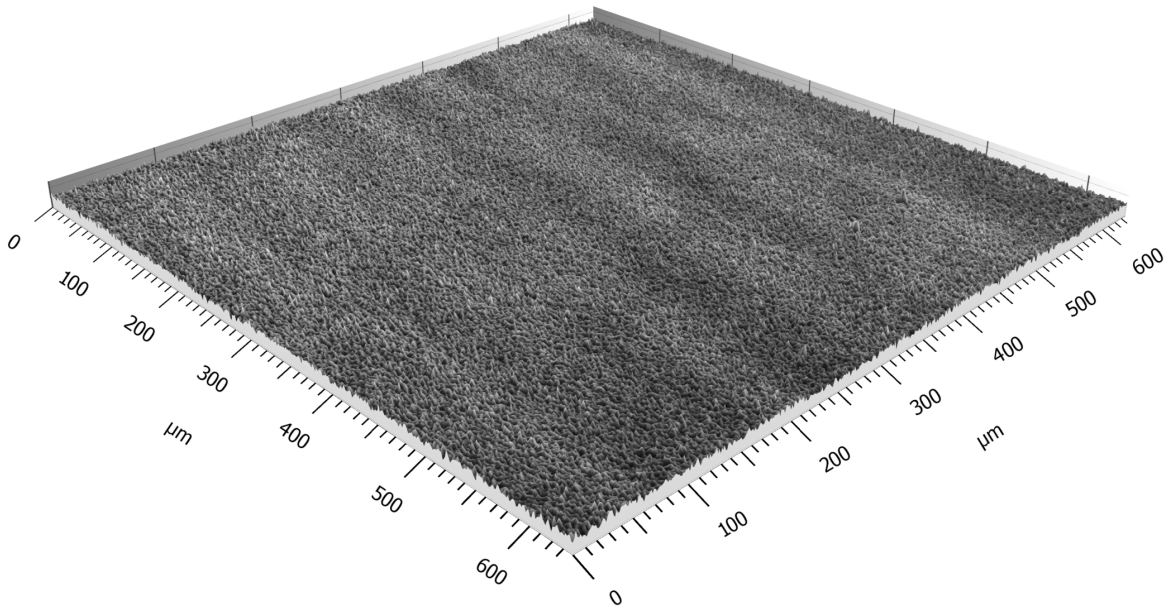

Figure 6-19. Confocal microscopy of Ti64L at 20x.

Through confocal microscope images, the grooves are not particularly emphasized. However, we observed in *Fig. 6 – 18 and 20* that surface is streaked.

Table 6-4. Height parameters of roughness evaluated through confocal microscopy analysis of TicpL and Ti64L samples.

ISO 25178			
Height Parameters			
	TicpL	*Ti64L*	
Sa	0.209	0.154	µm
Sq	0.266	0.194	µm
Sp	3.39	2.35	µm
Sv	1.11	0.840	µm
Sz	4.50	3.19	µm
Ssk	0.436	0.0765	
Sku	6.99	3.59	

Considering the roughness parameters listed in *Table 6 – 4* obtained by confocal microscopy, roughness meets the threshold we wanted to achieve for both pure titanium grade 2 and Ti6Al4V alloy. TicpL resulted to be slightly rougher than Ti64L. The skewness Ssk is slightly greater than 0 in both cases, which means that the height distribution is skewed on the mean plan and partially below it. The kurtosis value Sku is greater than 3 for TicpL and Ti64L, so peaks and valleys have a pointed shape, especially for TicpL, whose Sku is almost 7.

Amplitude parameters listed in *Table 6 – 5* were taken from three different measurements made with the contact profilometer, after which the mean and standard deviation of the values, obtained from linear measurements in three different zones of the same sample, were calculated. Roughness values Ra, Rq, and Rz increase by an order of magnitude for laser-treated samples in comparison with polished samples, reaching the expected values for both pure titanium and Ti6Al4V alloy.

Table 6-5. Amplitude parameters evaluated through profilometry.

ISO 4287					
Amplitude Parameters – Roughness Profile					
	TicpL	*TicpMP*	*Ti64L*	*Ti64MP*	
Ra	0.198 ± 0.002	0.037 ± 0.004	0.207 ± 0.007	0.052 ± 0.001	µm
Rq	0.25 ± 0.001	0.05 ± 0.005	0.257 ± 0.008	0.065 ± 0.002	µm
Rp	0.759 ± 0.059	0.093 ± 0.012	0.812 ± 0.066	0.157 ± 0.004	µm
Rv	0.742 ± 0.009	0.289 ± 0.033	0.762 ± 0.053	0.23 ± 0.029	µm
Rz	1.5 ± 0.06	0.383 ± 0.043	1.57 ± 0.116	0.387 ± 0.033	µm
Rsk	-0.075 ± 0.059	-1.5 ± 0.227	-0.058 ± 0.164	-0.416 ± 0.108	
Rku	2.973 ± 0.145	7.113 ± 1.089	2.853 ±0.03	3.01 ± 0.337	

By comparing the two tables above, it can be concluded that the roughness values obtained from the two different technologies are comparable and compliant with each other.

6.2.4 Wettability

Surface wettability was evaluated by means of the sessile drop method through contact angle measurements and the means and standard deviations of the resulted values, obtained from contact angle measurements in three different zones of the samples, are listed in *Table 6 – 6*.

Table 6-6. Means and standard deviations of contact angles resulted from wettability analysis.

Wettability				
	TicpL	*TicpMP*	*Ti64L*	*Ti64MP*
Contact angle [°]	70.33 ± 7.5	55.47 ± 3.2	84.76 ± 2.2	60.87 ± 6.7

The laser-treated samples TicpL and Ti64L were still in the range of hydrophilicity. However, compared to controls, the contact angle values increased following the surface treatment. The contact angles of the laser-treated samples are within the range that promotes the spreading of fibroblasts along the surfaces, i.e., the range of values between 60° and 90° [5],[6]. The increase in the contact angle can be attributed to the roughness of the surface and to the presence of submicrometric structures. A change in the chemistry of the surface can be also supposed.

6.3 Surface charge and microstructure

6.3.1 Zeta potential

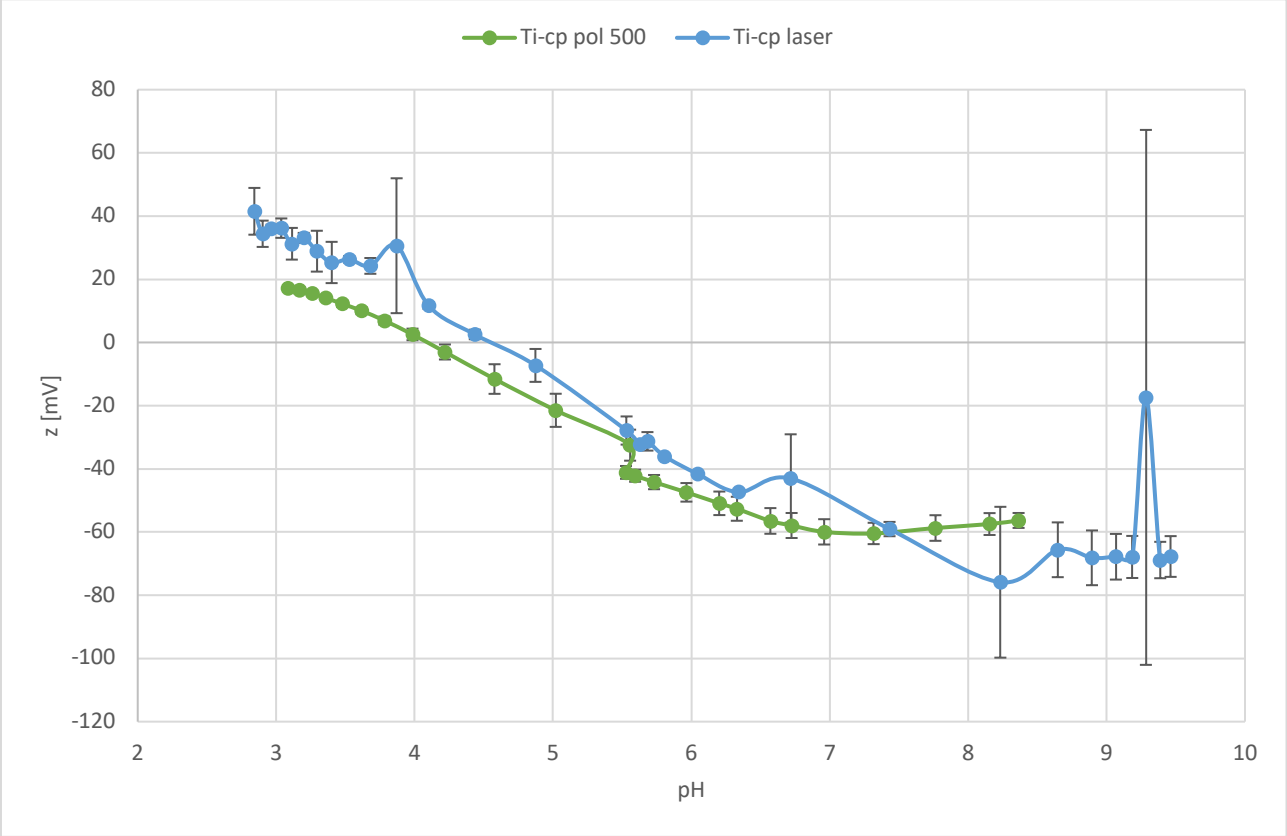

Figure 6-20. Zeta potential of TicpL sample in comparison with a Ti-cp sample polished to 500 grit paper taken as reference. The isoelectric point of the control and the TicpL sample are: $IEP_{control}$=4.09, IEP_{TicpL} = 4.55.

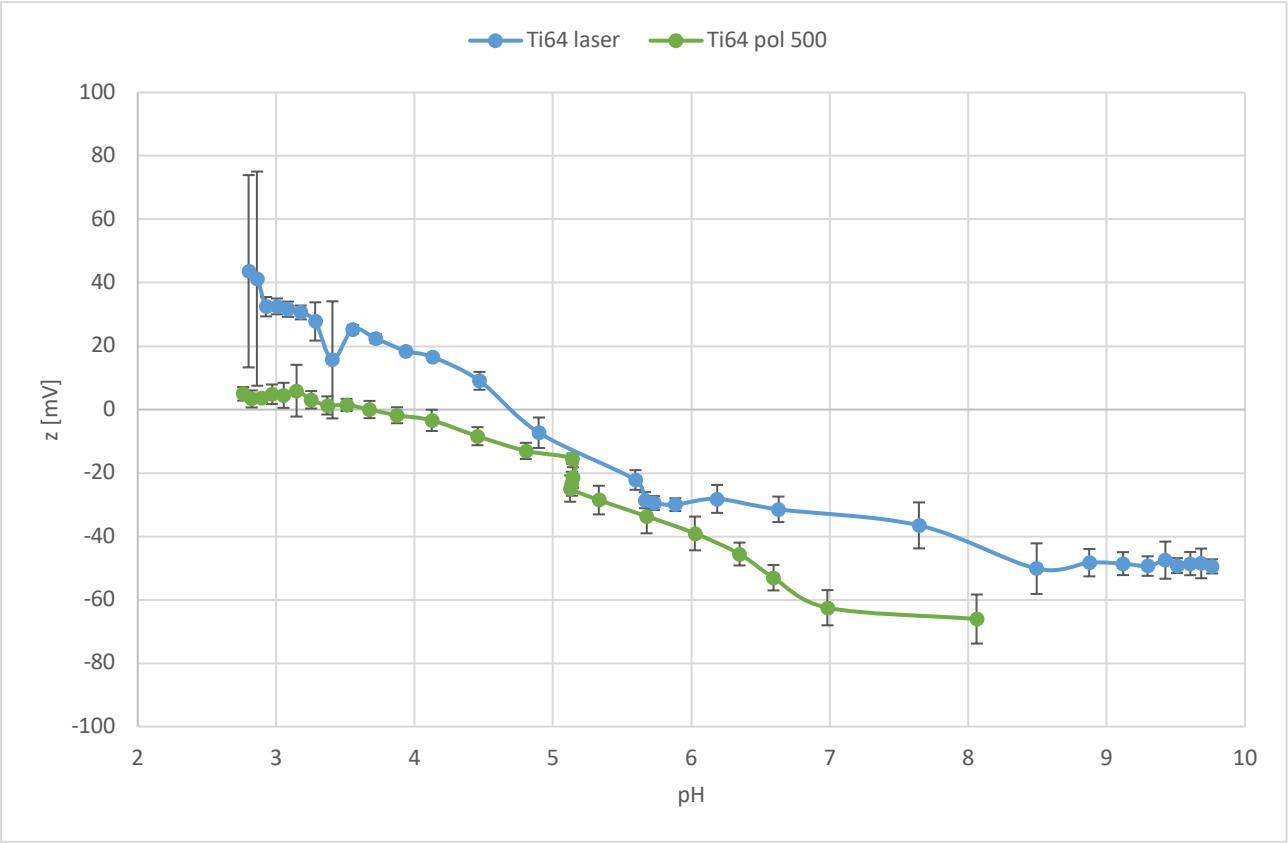

Figure 6-21. Zeta potential of Ti64L sample in comparison with a Ti6Al4V sample polished to 500 grit paper taken as reference. The isoelectric point of the control and the Ti64L sample are: $IEP_{control}$=3.68, IEP_{Ti64L} 4.71.

For both TicpL and Ti64L, a shift in the basic field is observed compared to the control, as it can be seen in Fig. 6 – 20 and 21. All surfaces are negatively charged at physiological pH. The laser-treated samples Ti64L and TicpL show small plateaus at the extremes of the basic ranges, which could be associated with a prevalence of acid functional groups. Furthermore, a shift towards the basic field is observed, as the isoelectric point goes from 4.09 to 4.55 for pure titanium and from 3.68 to 4.71 for the alloy. The onset of the basic plateau is at lower pH values for the untreated surfaces and has a shift towards the basic range after the surface treatment on both the materials. The shift of both the isoelectric points and onsets of the plateau can be assumed to be a consequence of the formation of an oxide layer with a prevalence of basic functional groups (OH) because of the laser treatment. In the case of the Ti64 alloy, it is also observable a higher slope of the zeta potential curve around the isoelectric point: this change can be explained by a lower wettability in agreement with the contact angle measurement. If the surface is highly hydrophilic, it strongly adsorbs the water molecules, and they are not desorbed even if the composition of the liquid phase is changing: in this case the change of the zeta potential with pH is low and the slope of the curve is low. The opposite occurs on a hydrophobic surface, where hydroxyl or hydronium ions easily substitute adsorbed water and rapidly change the zeta potential by changing pH of the liquid phase.

Despite a great number of studies in the field, it is still to be explored and understanding the relationship between surface charge, also referred to as zeta potential, and cellular interaction is still highly controversial. For instance, it is believed that negative zeta potential favors various bone growth processes including nucleation and proliferation of bone cells [7], but the rate of fibroblast

cells proliferation was significantly depressed on surfaces with a higher magnitude of negative potential [8]. The presence of basic functional groups on a titanium surface is not usual and it can be of interest both for the interaction with the physiological liquids (such as the bioactive behaviour and formation of hydroxyapatite), proteins, and cells.

6.3.2 XRD analysis

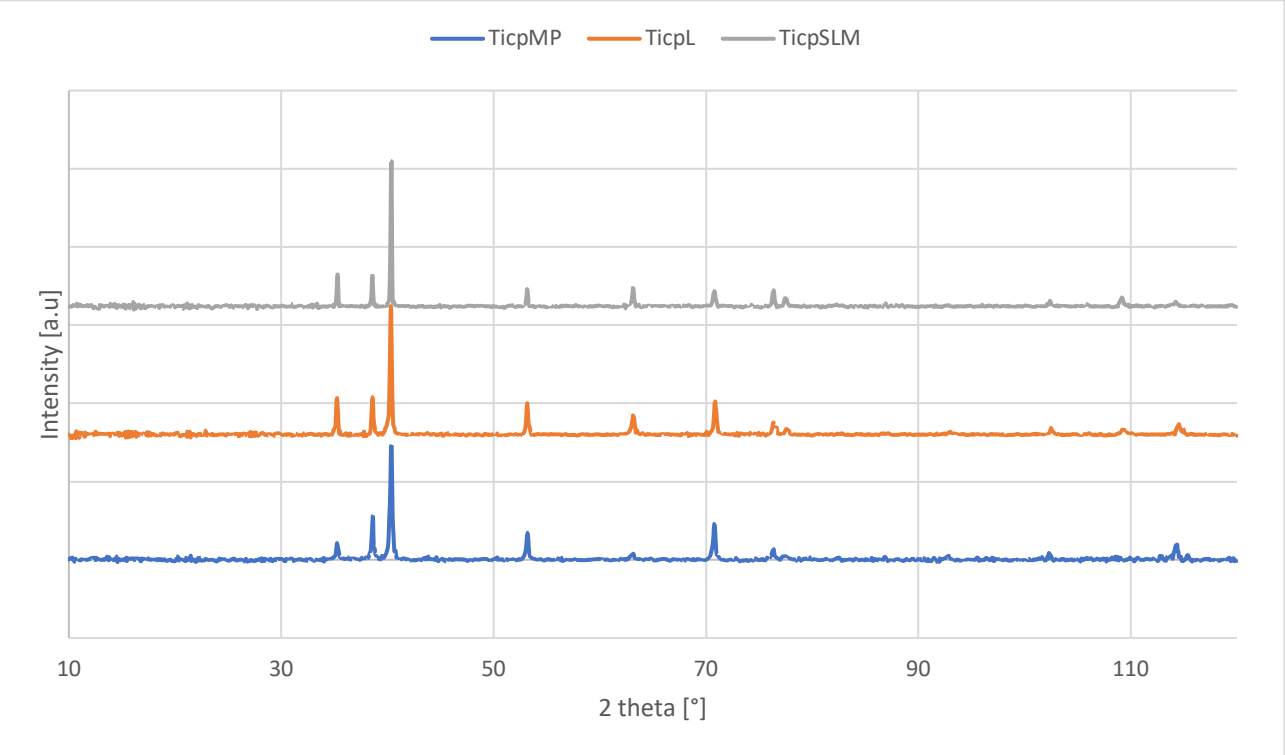

Figure 6-22. Comparison of pure titanium grade 2 spectrums, normalized to the main peak height of TicpMP.

As shown in *Fig. 6 – 22*, the spectrums of polished titanium TicpMP, titanium sample obtained by selective laser melting TicpSLM, and laser-treated titanium TicpL are equal, showing that the crystallographic structure is the same. Comparing the position of the main peaks in *Fig. 6 – 23*, no shift in the martensitic zone is evident.

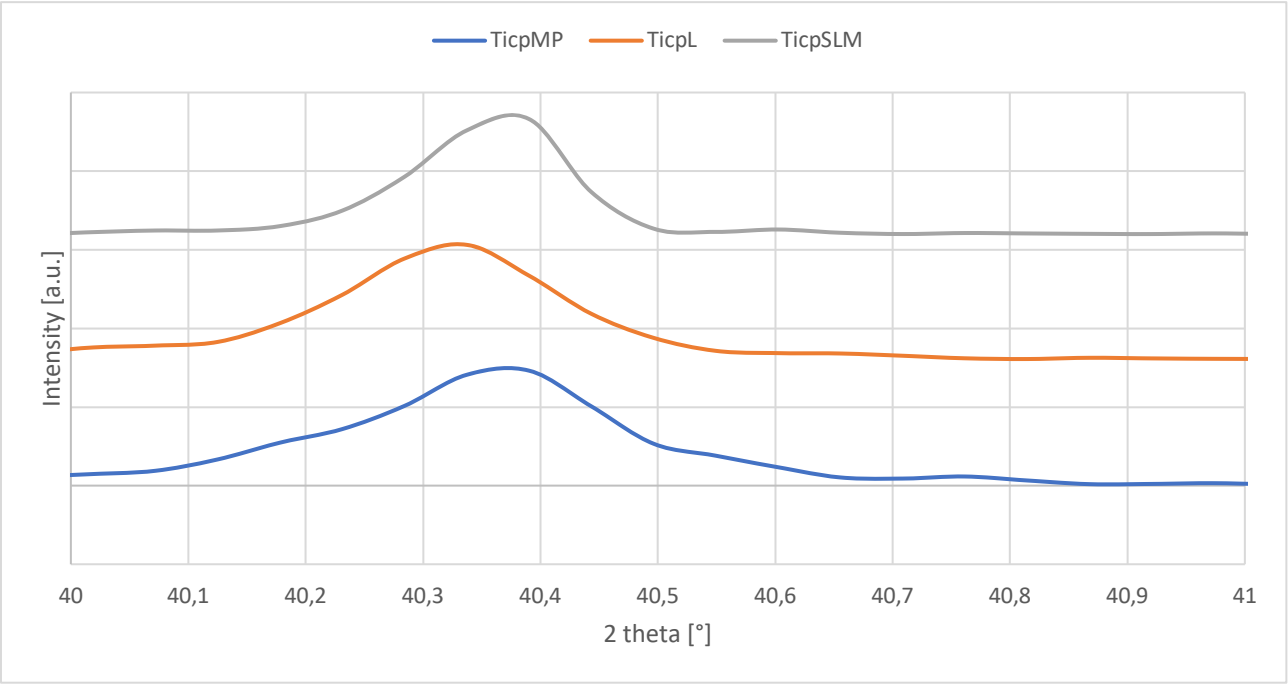

Figure 6-23. Comparison between the position of the main peaks.

As expected, peaks belong to the hexagonal titanium (alpha) for both TicpMP and TicpL (*Fig. 6 – 24*).

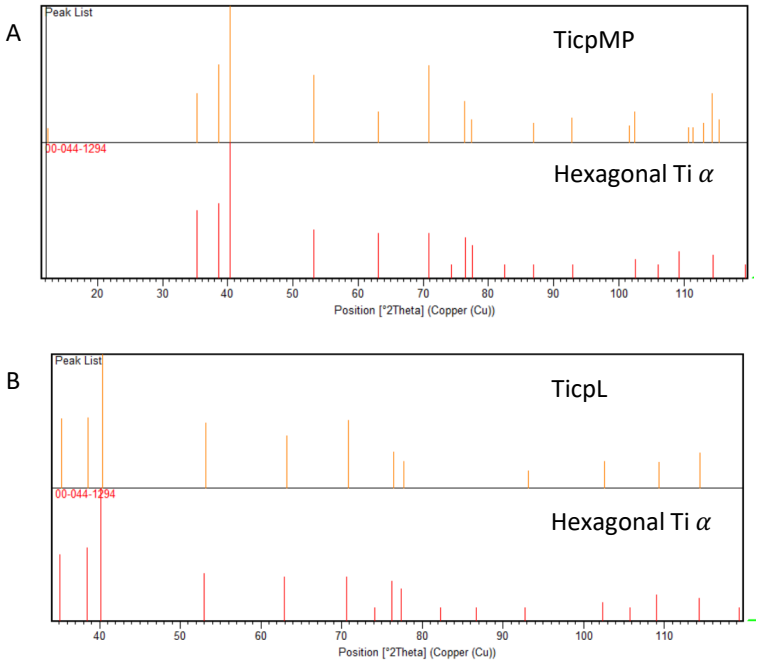

Figure 6-24. A) Comparison between peaks of TicpMP and hexagonal titanium alpha and B) Comparison between peaks of TicpL and hexagonal titanium alpha.

In *Fig. 6 – 25*, the very high peak at 80 for Ti64MP could be due to preferential orientation as consequence of polishing.

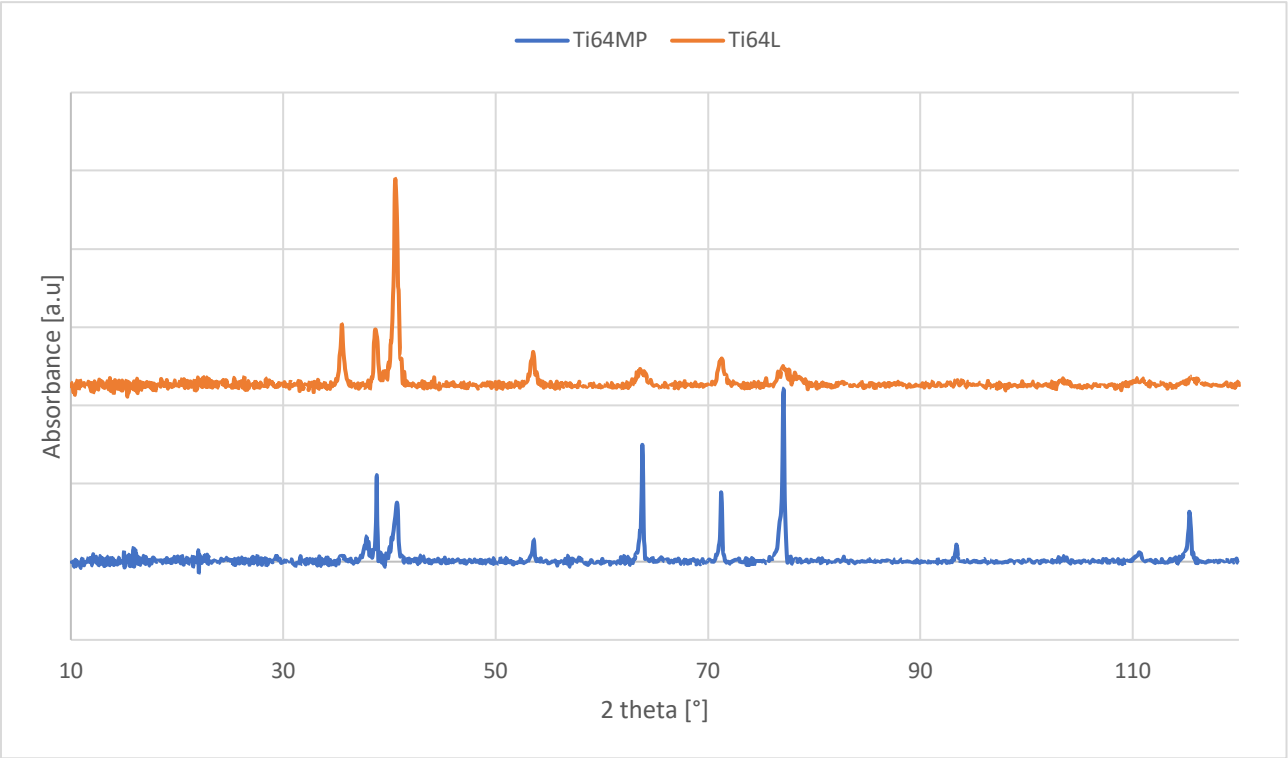

Figure 6-25. Comparison of pure titanium grade 2 spectrums not normalized.

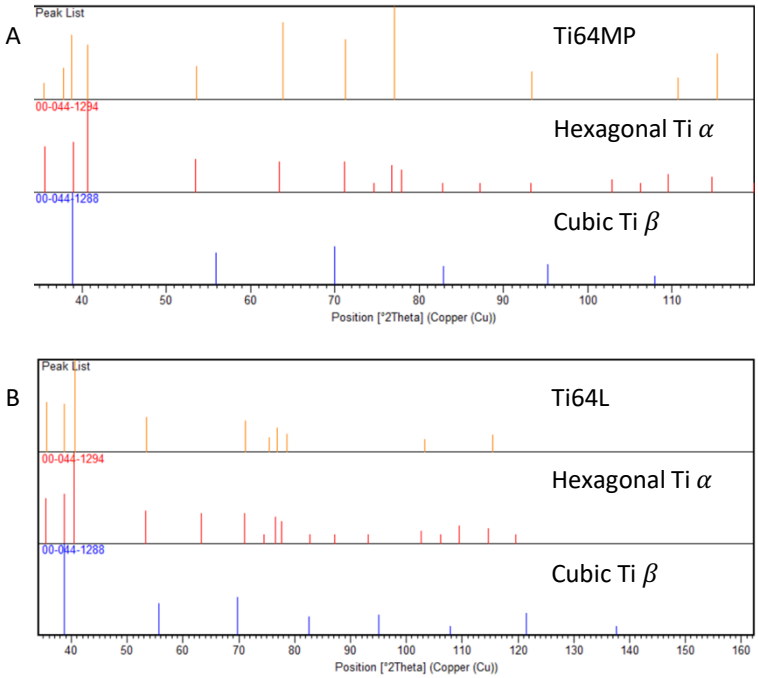

Figure 6-26. Comparison between peaks of Ti64MP, hexagonal titanium alpha and cubic titanium beta and B) Comparison between peaks of Ti64L, hexagonal titanium alpha and cubic titanium beta.

As *Fig. 6 – 26* shows, the peaks are all attributable to alpha titanium, the beta phase is usually seen after heat treatment.

6.3.3 Metallographic etching and microstructure – cross-section

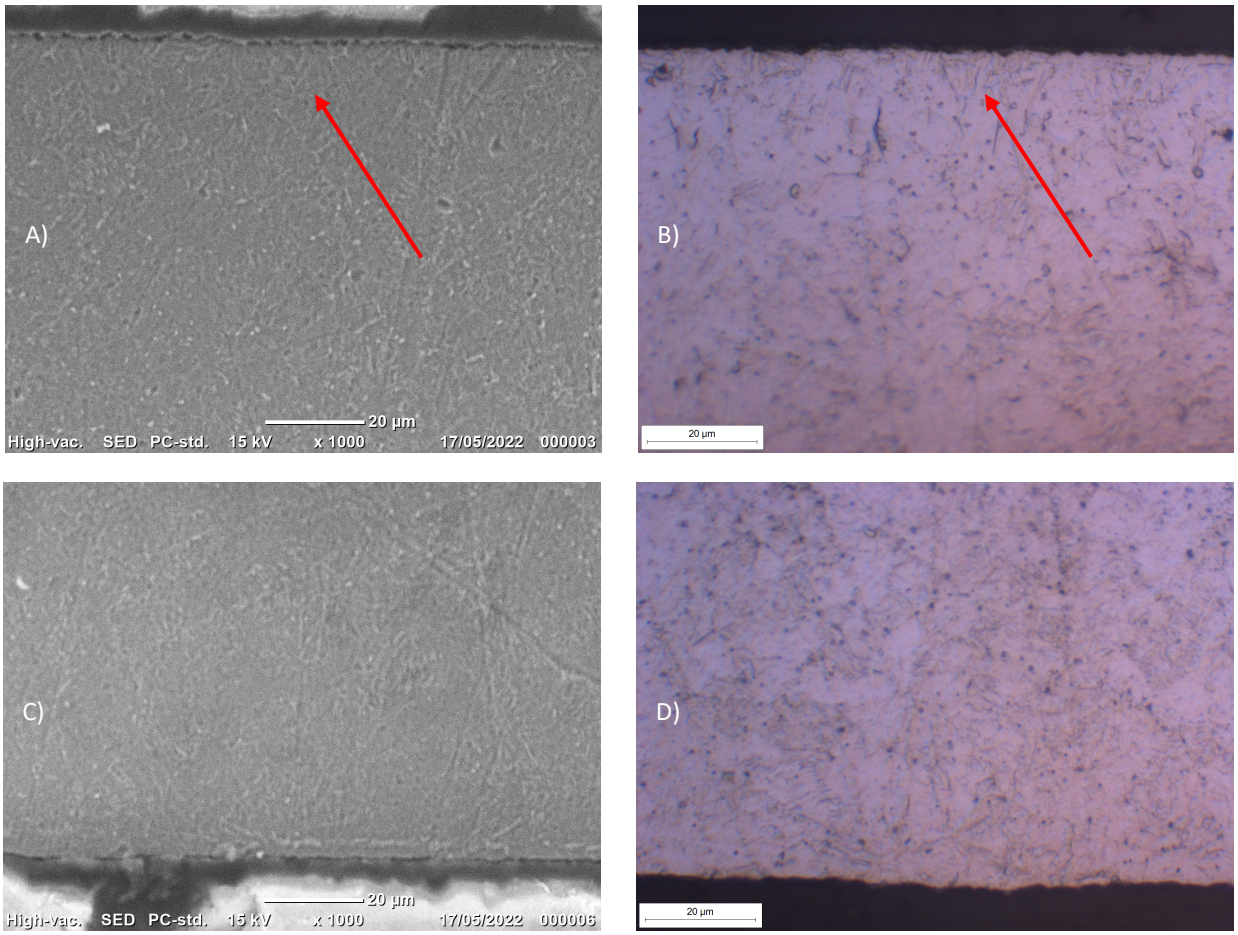

Figure 6-27. A) SEM image and B) optical microscope image of the cross section of TicpL sample in the laser-treated zone. C) SEM image and D) optical microscope image of the same sample in the non-treated zone.

After performing an acid etching with Kroll's solution on the cross-section of the samples, the surfaces were observed both under the optical microscope and at the SEM microscope.

As shown in *Fig. 6 – 27*, the pure titanium TicpL sample has a very thin layer (no more than 10 µm) of the lamellar structure near the treated surface, which seems to differ from the rest of the bulk material. This lamellar pattern is not evident near the untreated surface (at the bottom of images *Fig. 6 – 27 C) and D)*).

In the alloy sample Ti64L, *Fig. 6 – 28*, the difference between the area close to the untreated surface and the area on the opposite side is not so evident. However, after the metallographic etching, it is possible to see alpha and beta phases. Alpha phase predominates in the material, whereas beta phase is present in the form of grain boundaries. It would appear that there is less beta phase behind the treated surface than in the bulk of the material.

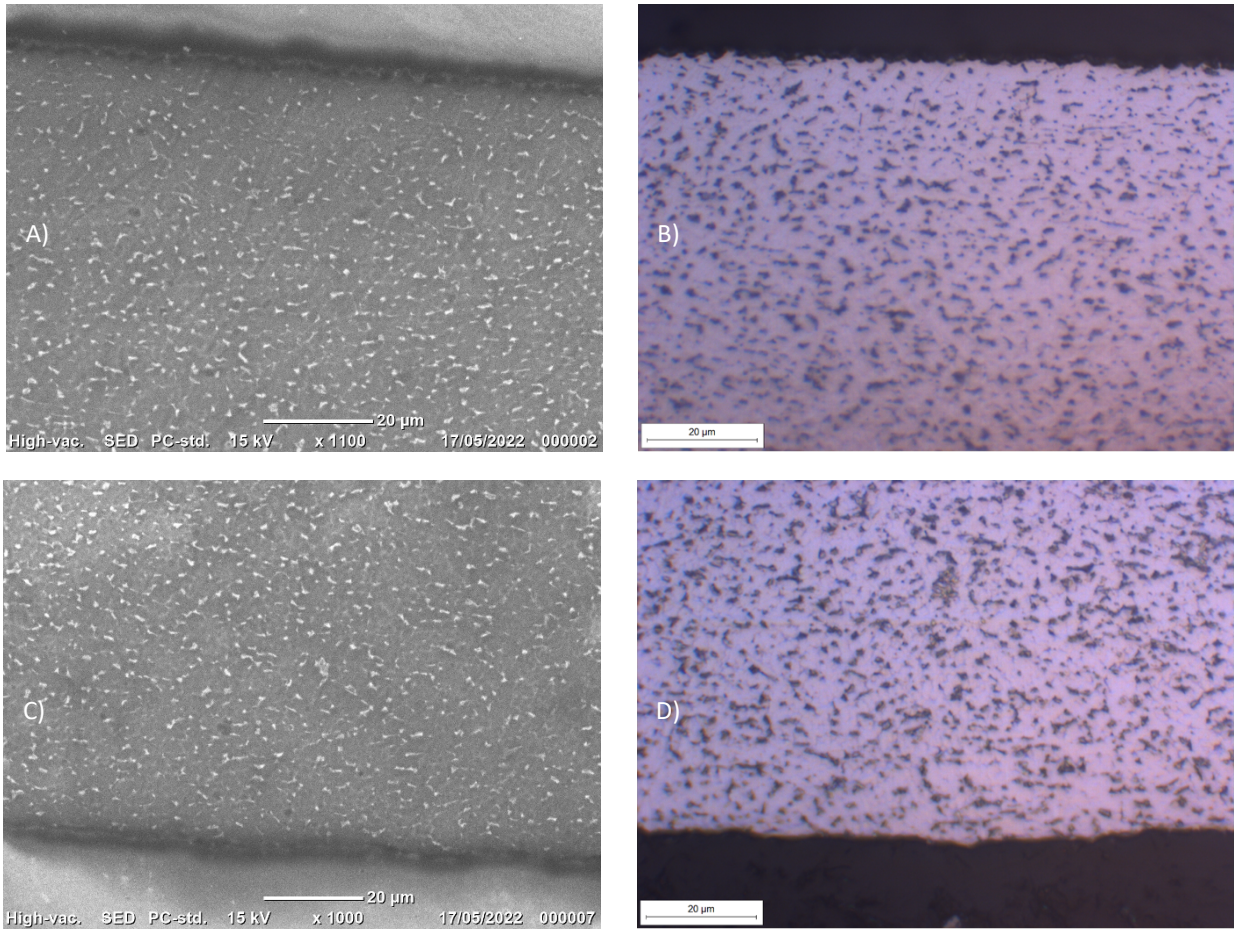

Figure 6-28. A) SEM image and B) optical microscope image of the lateral section of Ti64L sample in the laser-treated zone. C) SEM image and D) optical microscope image of the same sample in the non-treated zone.

6.4 Cell adhesion

6.4.1 Cytocompatibility

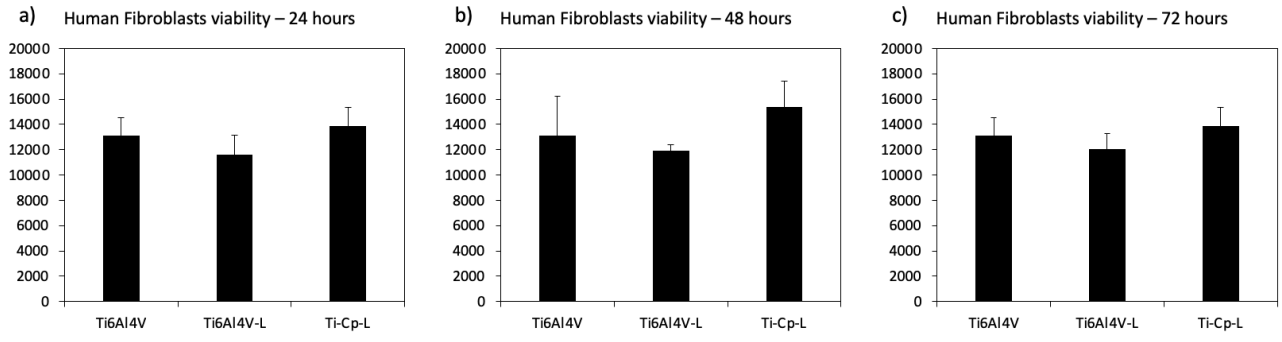

Figure 6-29. Fibroblasts' metabolic activity (Alamar blue assay) after 24 (a), 48 (b), and 72 (c) hours of direct seeding on specimens' surfaces. Ti6Al4V mirror-polished samples were used as controls, and the pure titanium samples were not considered for the viability analysis as they were probably contaminated since cells unexpectedly tended not to survive on the TicpMP surfaces.

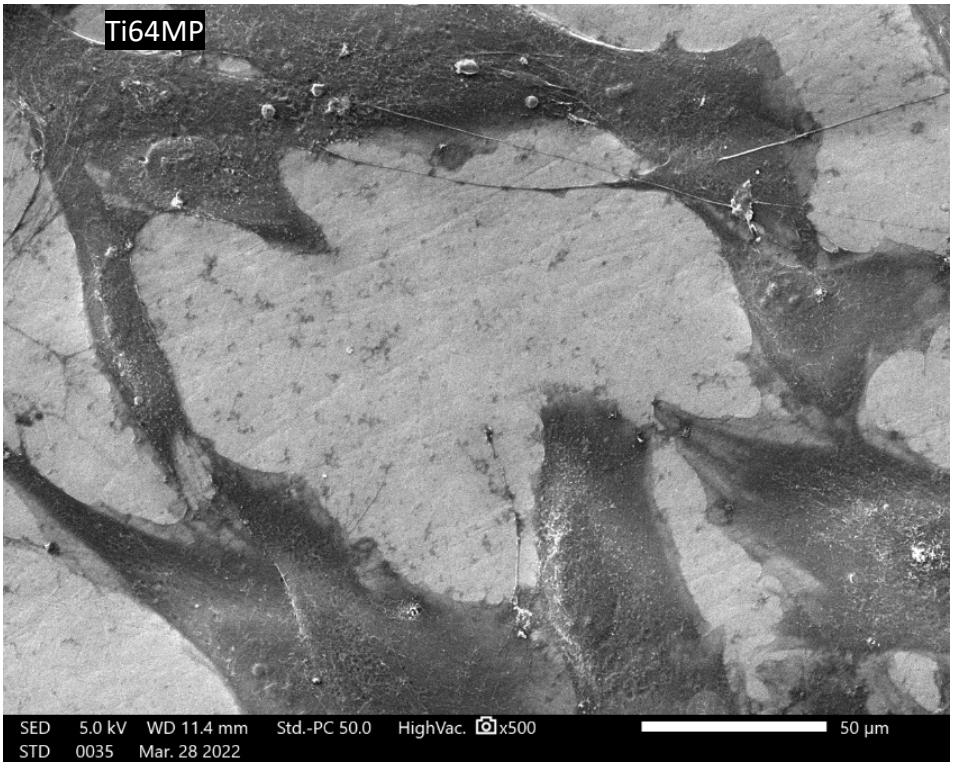

Figure 6-30. SEM image of adhered cells spread after 72 hours on Ti64MP sample. Fibroblast adhesion has a casual and unordered direction.

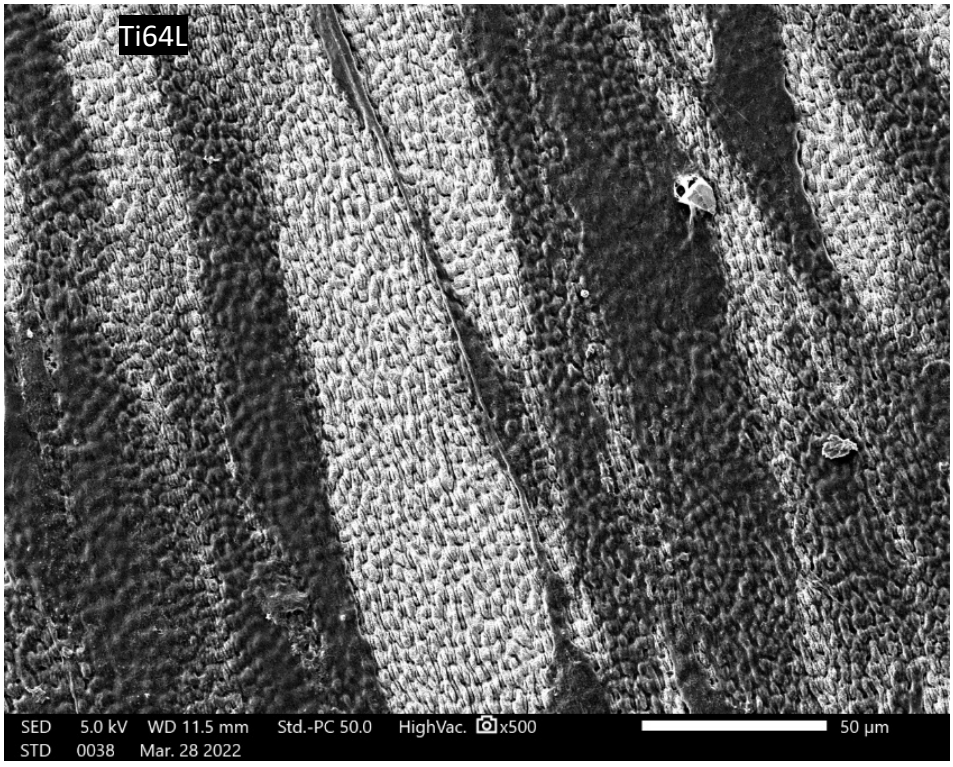

Figure 6-31. SEM image of adhered cells spread after 72 hours on Ti64L sample. A directional adhesion along the grooves is observable in the image. Laser induced periodic surface structures (LIPSS), which characterize laser-treated surface are also visible.

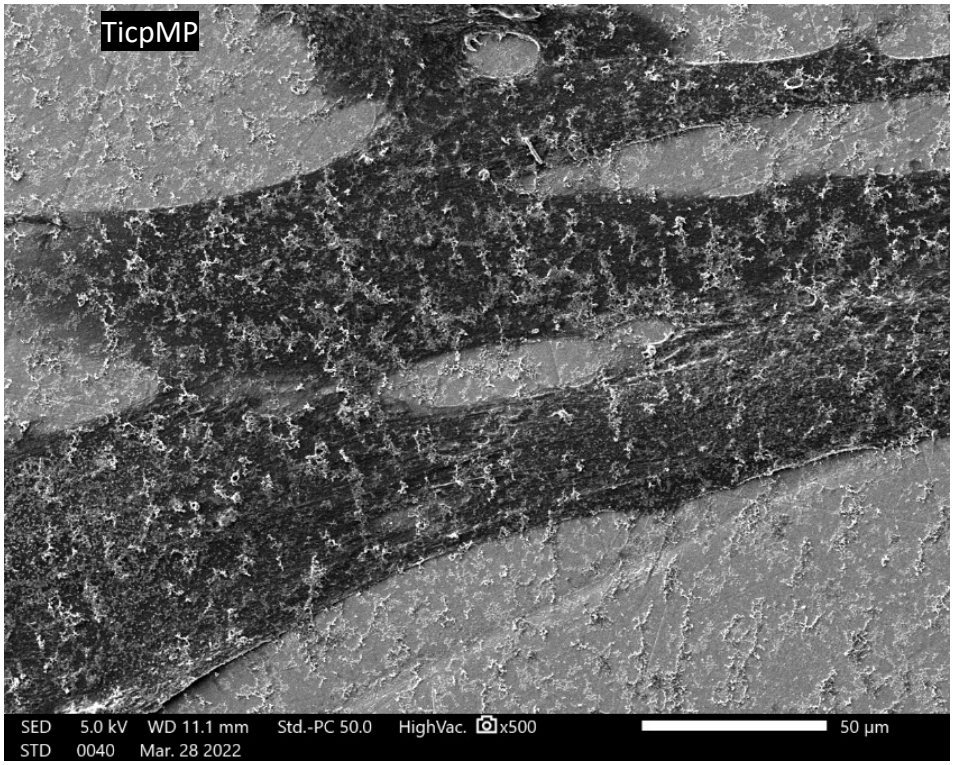

Figure 6-32. SEM image of adhered cells spread after 72 hours on TicpMP sample. Again, no directionality is observed in cell adhesion.

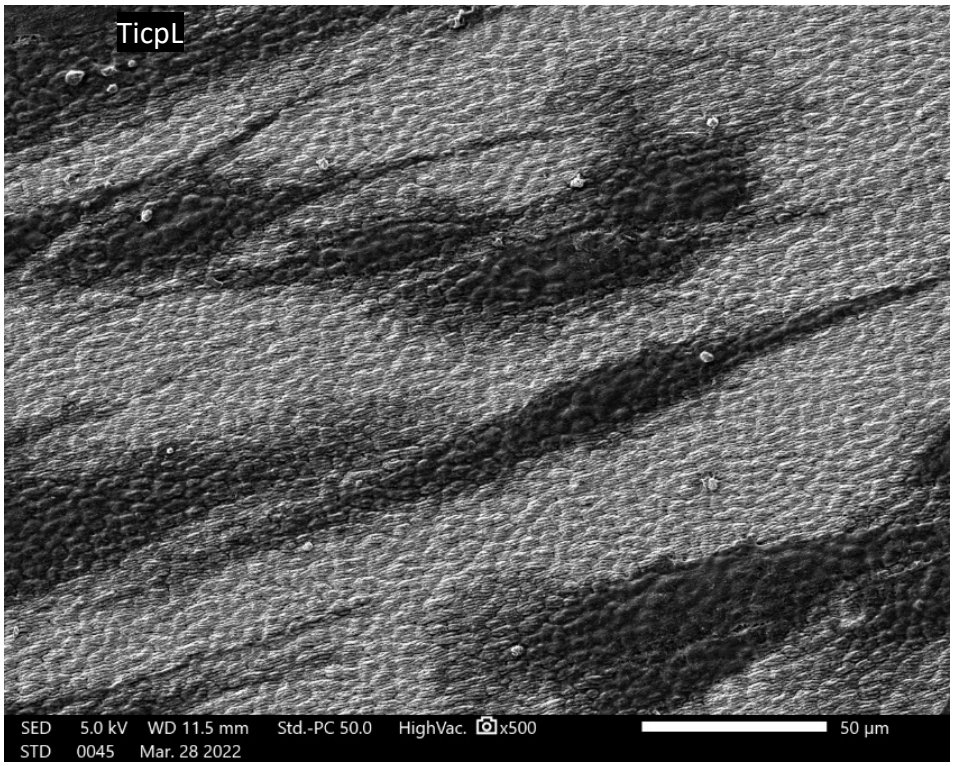

Figure 6-33. SEM image of adhered cells spread after 72 hours on TicpL sample. As in Fig. 6 – 31, fibroblasts align along the grooves visibly.

Results concerning cells' metabolic activity on surfaces of the samples and their morphology are summarized in *Fig. 6 – 29*. In general, the laser treatment (Ti64L and TicpL samples) did not

introduce any toxic elements reducing the metabolic activity of the seeded fibroblasts during the testes time-points (*Fig. 6 – 29 a-c*) and cell viability is comparable with the one of the Ti6Al4V polished control. The only group reporting toxicity is the pure titanium mirror-polished controls TicpMP probably due to some surface contamination. However, for a matter of time, it was not possible to investigate and possibly solve this problem.

SEM images (*Fig. 6 – 30, 6 – 31, 6 – 32 and 6 – 33*) obtained after 72 hours of cultivations provided a visual confirmation of the cells' correct adhesion and spread; moreover, it was evident how the spread was influenced by the surface topography as the cytoskeleton orientation was observed following the same orientation of the grooves (Ti64L and TicpL). On the opposite, when the grooves were not introduced (Ti64MP and TicpMP), cell orientation was random, thus not suggesting any influence due to the surface topography.

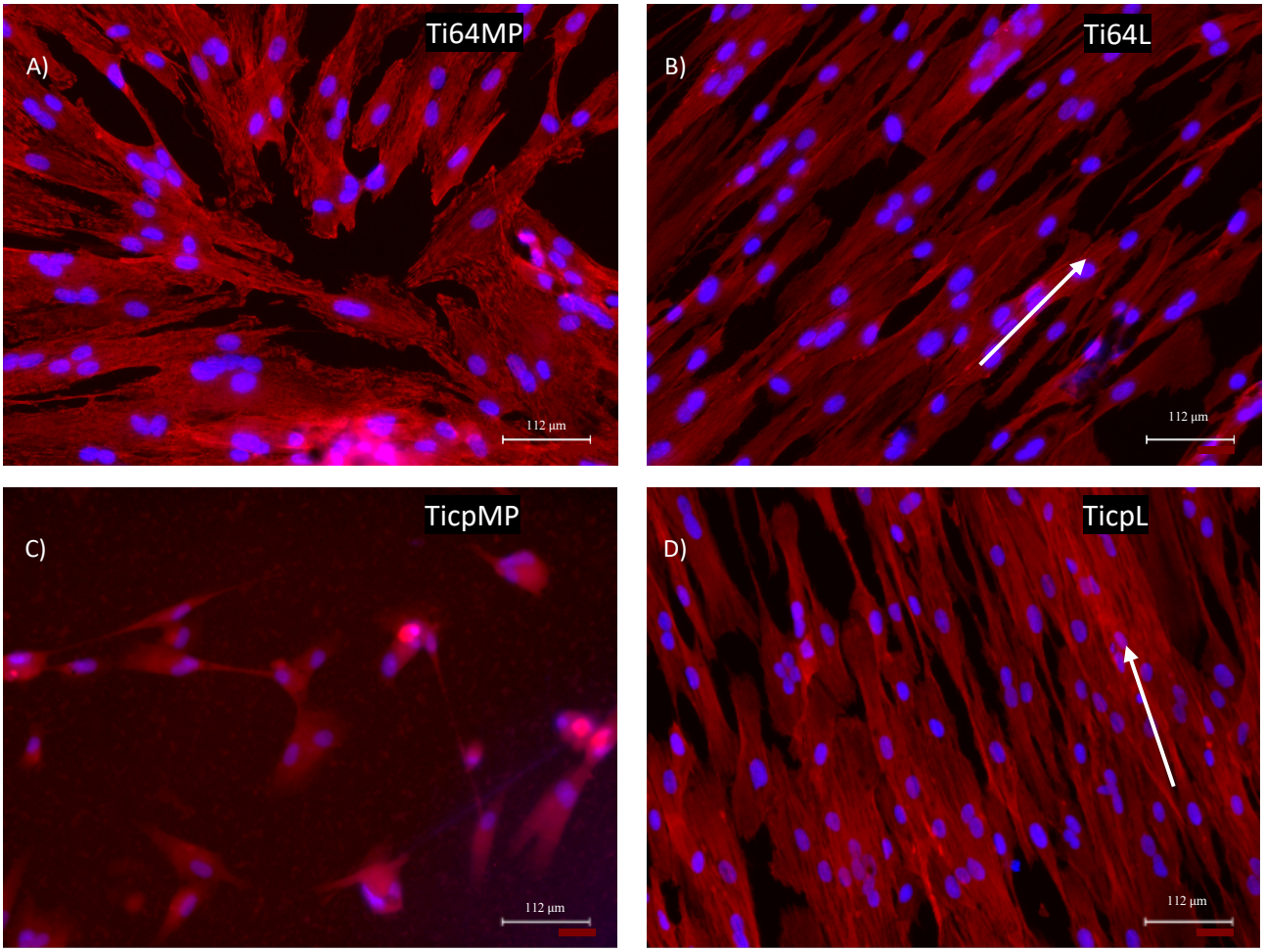

Figure 6-34. IF staining of cells' cytoskeleton (red by phalloidin) and nuclei (blue by DAPI) after 72 hours of direct cultivation. A) Ti6Al4V mirror-polished (Ti64MP), B) Ti6Al4V laser-treated (Ti64L), C) Pure titanium mirror-polished (TicpMP) and D) Pure titanium laser-treated (TicpL). White arrows show the direction of the grooves.

As a confirmation of the grooves-guided cell orientation, IF staining (*Fig. 6 – 34*) remarked the evidence that cells cultivated onto laser-treated samples aligned following the same orientation of the grooves, whose direction has been highlighted with white arrows in the figure *Fig. 6 – 34 B)* and *Fig. 6 – 34 D)*. By higher magnification SEM images (*Fig. 6 – 35*) this guiding role of the grooves was

particularly evident for both the Ti64L and TicpL substrates where the cells are aligned in parallel with the grooves while they grow randomly oriented on polished surfaces.

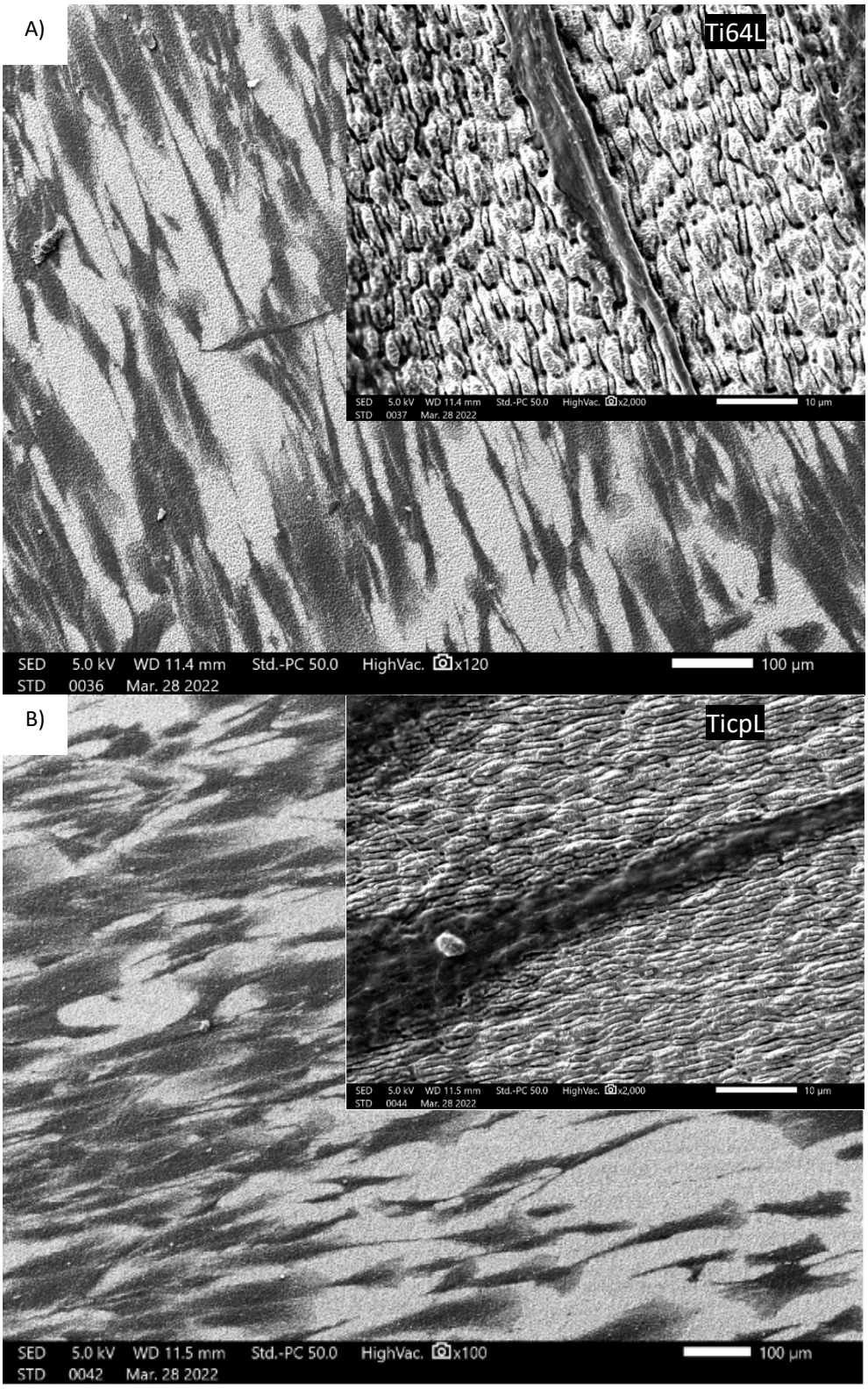

Figure 6-35. SEM high magnification images of cells aligned onto Ti6Al4V (A) and Ti-Cp (B) laser-treated substrates.

6.4.2 Antibacterial activity

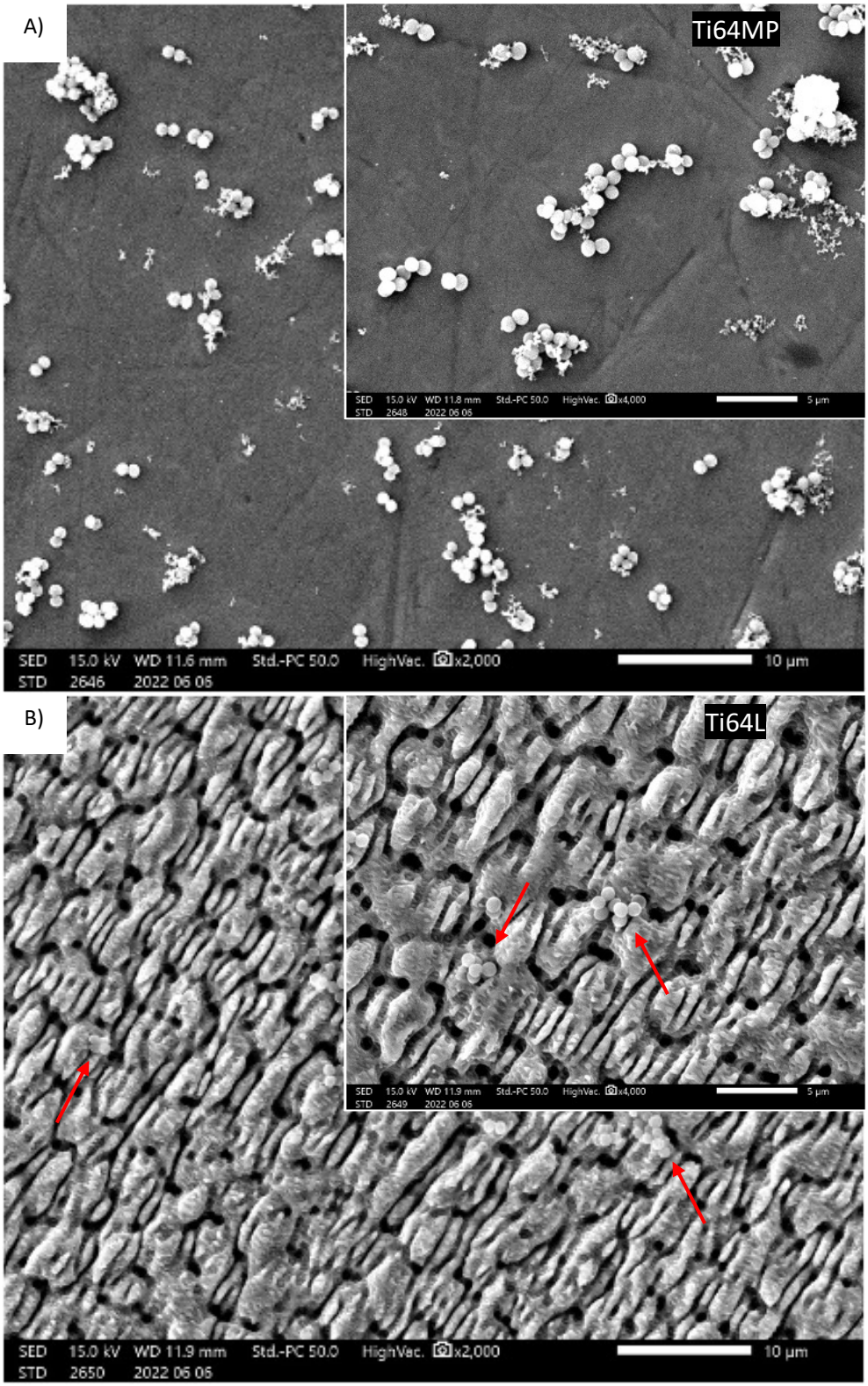

Figure 6-36. Low (2000x) and high (7000x) magnification SEM images of S. aureus colonies grown into Ti64MP (A) and Ti64L (B) samples' surfaces after 90 minutes of cultivation.

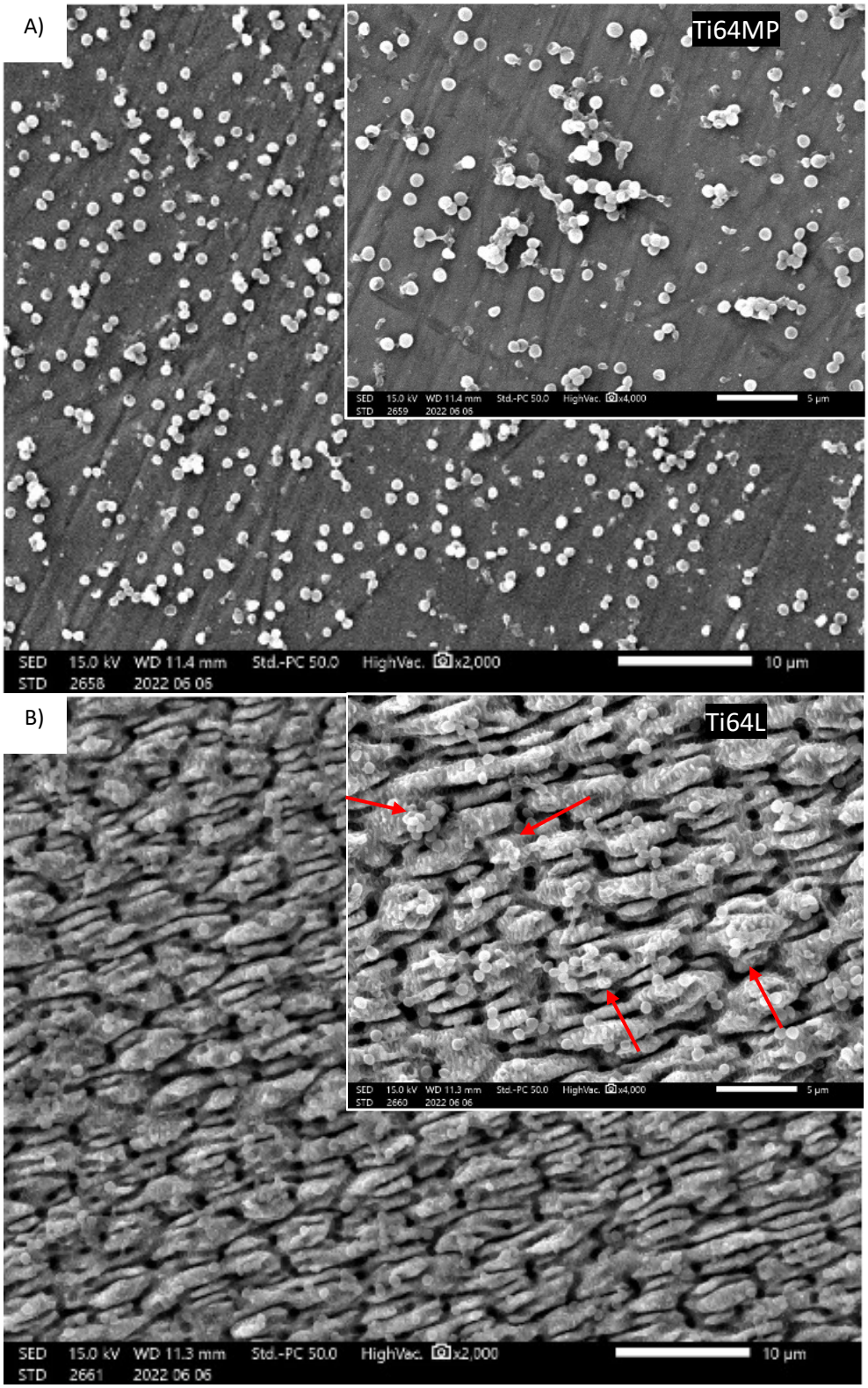

Figure 6-37. Low (2000x) and high (7000x) magnification SEM images of S. aureus colonies grown into Ti64MP (A) and Ti64L (B) samples' surfaces after 24 hours of cultivation.

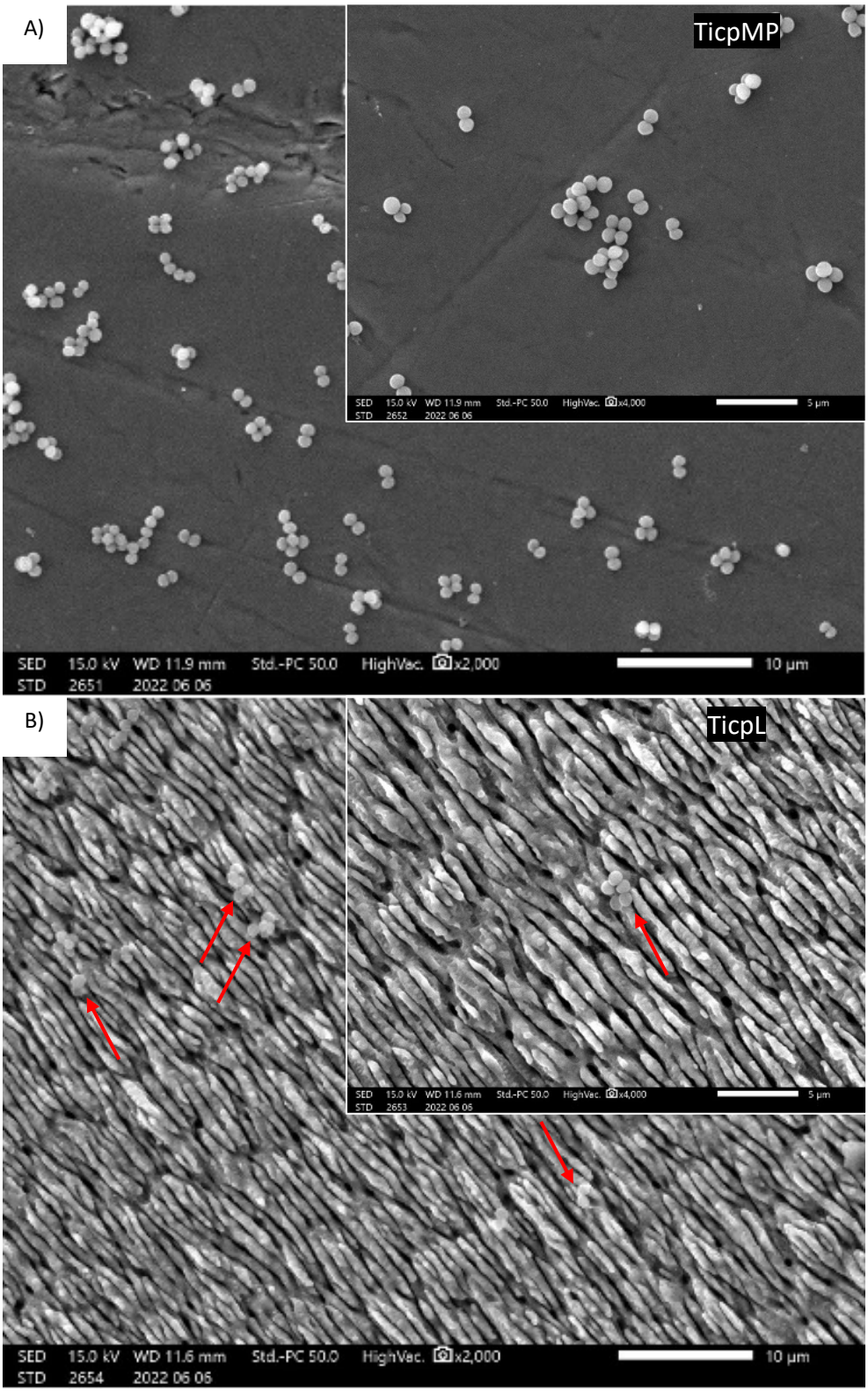

Figure 6-38. Low (2000x) and high (7000x) magnification SEM images of S. aureus colonies grown into TicpMP (A) and TicpL (B) samples' surfaces after 90 minutes of cultivation.

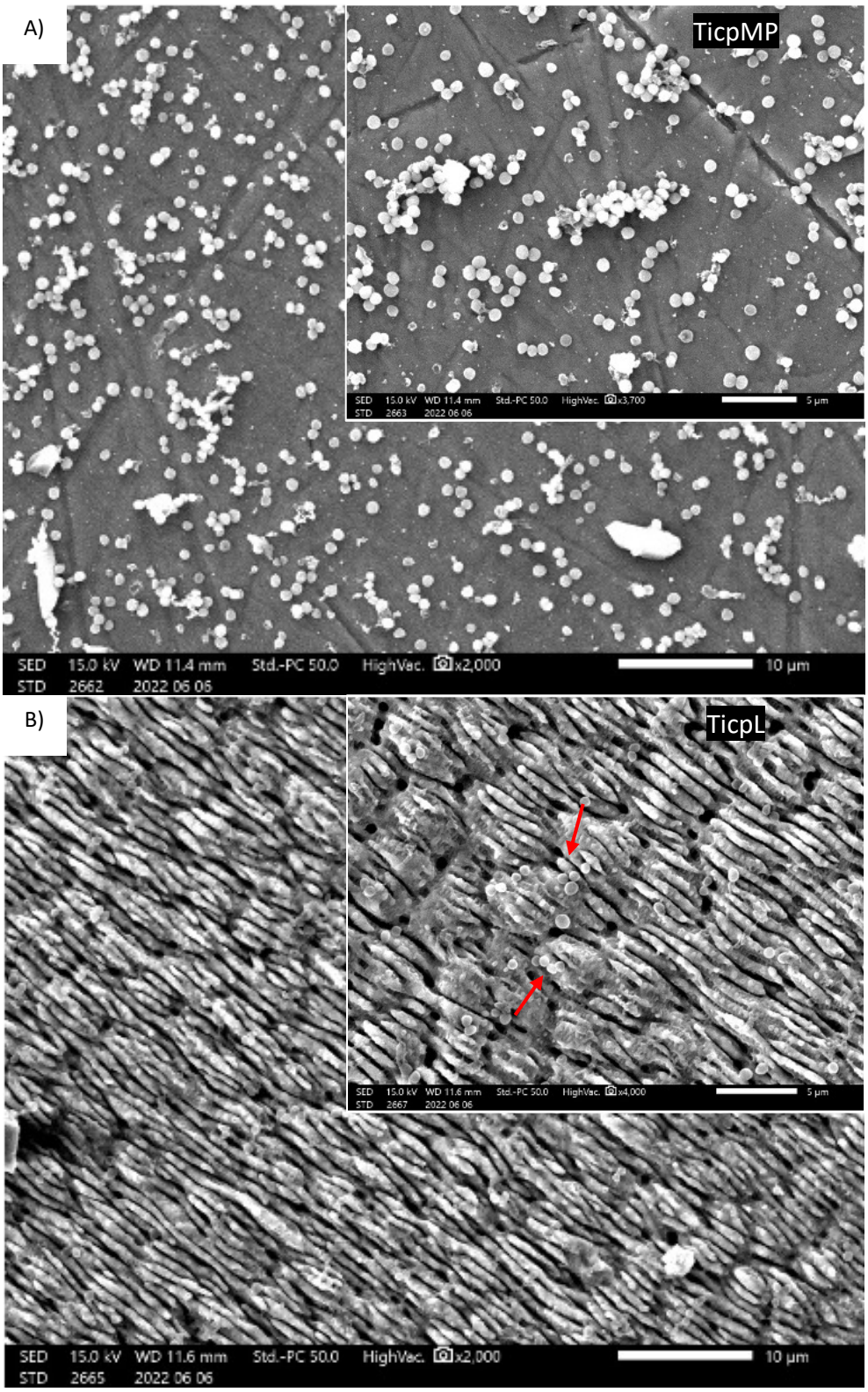

Figure 6-39. Low (2000x) and high (7000x) magnification SEM images of S. aureus colonies grown into TicpMP (A) and TicpL (B) samples' surfaces after 24 hours of cultivation.

Results concerning specimens' antibacterial activity are summarized in *Fig. 6 – 36, 37, 38 and 39*. As can be observed by the SEM images collected after 90 minutes and 24 hours of cultivation the presence of the grooves seems to reduce the number of adhered bacteria when low magnification

images were acquired. Moreover, when higher magnification images were operated it was appreciated a reduction of the 3D biofilm-like aggregates that were observed on the smooth surfaces of the control specimens. It can be observed that bacteria on laser-treated surfaces are less organized, and their biofilm-forming ability is reduced compared to the polished controls.

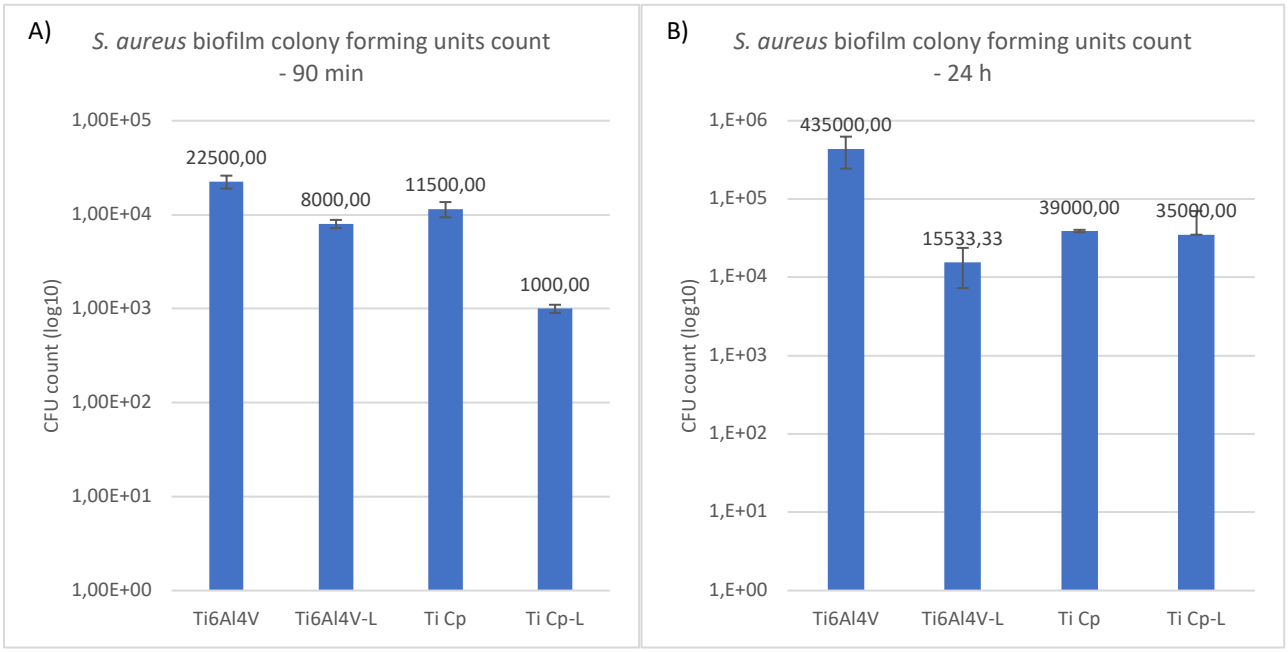

Figure 6-40. Number count of the viable colonies after 90 minutes (A) and 24 hours (B). The bars represent means and standard deviations.

In agreement with previous results, the CFU count (Fig. 6 – 40) after 90 minutes and 24 hours showed that a lower number of viable colonies adhered to the laser-treated surfaces, in comparison with the MP control samples. It can be observed that at both time points there is one logarithm of difference between controls and grooved samples, so these results confirm an antibacterial effect.

Considering that no element or compound with the ability of killing bacteria has been added to the surface, no active antibacterial action is expected by the treated surfaces. On the other side, a passive mechanism of anti-microfouling that means a reduction in the adhesion and/or proliferation of bacteria and biofilm formation can be expected because of the surface topography, and it was observed. This effect can be synergic to some active antibacterial strategy (surface functionalization with some antibacterial element or compound) with the final goal to reduce the risk of the implant infection.

The observed results agree with the literature [11],[12], which demonstrated that a nanoscale structured topography does not allow bacterial adhesion not because it causes their death (*direct contact killing* effect), but because surface patterns with feature sizes between approximately 500 nm and 1 µm possess bacterial anti-adhesion properties. The sharp nanotopography typical of laser-treated samples would in fact allow this event to occur, as illustrated in *Fig. 6 – 41*.

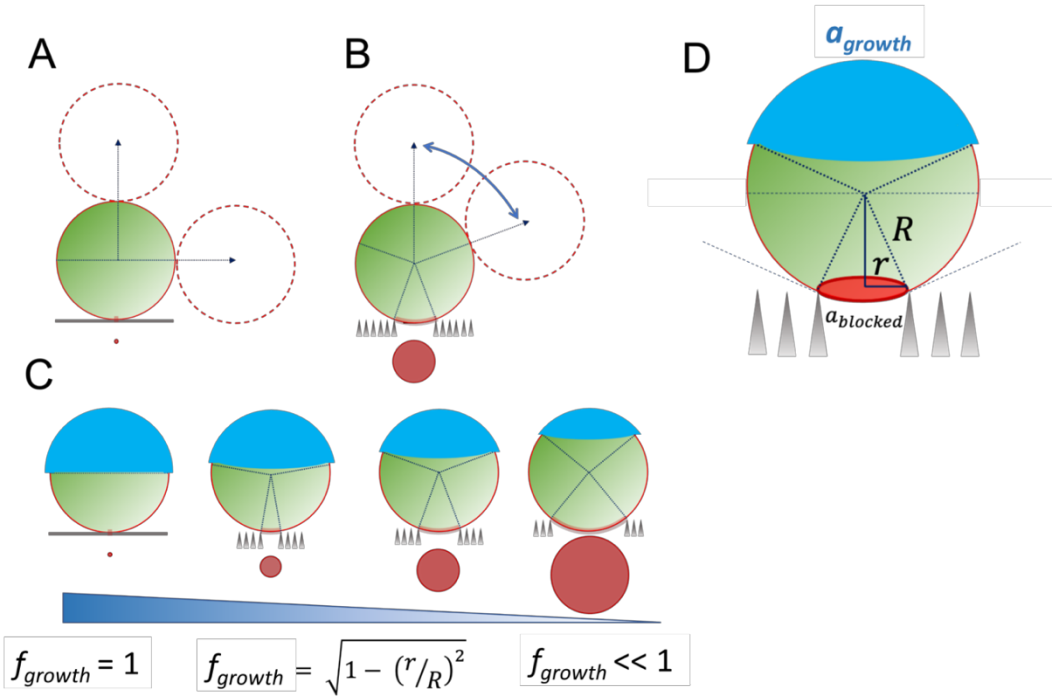

Figure 6-41. Effect of local nanotopography on bacteria growth and division: A) On a flat surface, the orientation angle for subsequent cell division is maximum, allowing three other cells to easily bind at 90° angles. B) The bacterium rests on a sharp nanotopography, and the allowed angles for subsequent cell division are restricted by the boundary of the cell that lies within the cavity as shown in red. C, D) Fraction of cell area (f_{growth}) where cell division is allowed decreases if the area of the cell that lies in the cavity ($a_{blocked}$) increases. Adapted from [11].

The topography obtained from the laser treatment carried out during the present work causes a bacteriostatic effect by decreasing the critical angle, defined as the angle a_{growth} that allows bacterial growth and division [11]. Thus, fraction of cell area f_{growth}, where bacteria division and proliferation are allowed, decrease.

Furthermore, surface roughness affects bacterial adhesion.

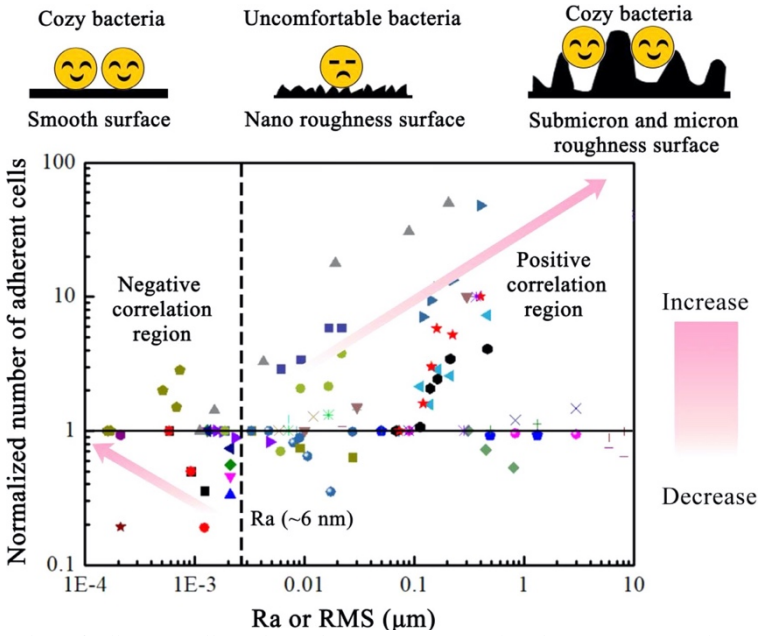

Figure 6-42. Normalized number of adherent cells and roughness parameters (used in average roughness Ra or root mean square roughness RMS). [12]

Fig. 6 – 42, in which each group of data is shown as different colors or symbols and adherent bacterial number on the minimum roughness surface is used for normalization [12], shows that at lower roughness regions and with roughness in the micron range bacterial adhesion tends to increase, whereas for roughness between a few nanometers and a few hundred nanometers bacterial adhesion appears to be diminished. The laser samples obtained from the experiment have an average roughness Ra of 0.2 μm, which should therefore give the surface bacteriostatic properties.

Reference

[1] Voisey K.T., Scotchford C.A., Martin L., Gill H.S. "Effect of Q-switched laser surface texturing of titanium on osteoblast cell response." *Physics Procedia*. Vol. 56, 2014, p. 1126-1135.

[2] Walboomers X.F., Croes H. J. E., Ginsel L. A., Jansen J. A. "Contact guidance of rat fibroblasts on various implant materials." *Journal of Biomedical Material Research*. Vol. 47(2), 1999, p.204-212.

[3] Ferraris S., Warchomicka F., Ramskogler C., Tortello M., Cochis A., Scalia A., Gautier di Confiengo G., Keckes J., Spriano S. "Surface structuring by Electron Beam for improved soft tissues adhesion and reduced bacterial contamination on Ti-grade 2." *Journal of Material Processing Tech*. Vol. 266, 2019, p.518-529.

[4] Ferraris S., Warchomicka F., Iranshahi F., Rimondini L., Cochis A., Spriano S. "Electron beam structuring of Ti6Al4V: new insight on the material surface properties influencing the bacterial adhesion." *Materials*. Vol.13(2), 2020, p. 409-420.

[5] Tamada Y., Ikada Q. "Effect of preadsorbed proteins on cell adhesion to polymer surfaces." *Journal of Colloid Interface Science*. Vol. 155(2), 1993, p. 334–339.

[6] Wei J., Igarashi T., Okumori N., Igarashi T., Maetani T., Liu B., Yoshinari M. "Influence of surface wettability on competitive protein adsorption and initial attachment of osteoblasts." *Biomedical Materials*. Vol. 4(4), 2009, 045002.

[7] Uskokovi´c V., Odsinada R., Djordjevic D., Habelitz S., "Dynamic light scattering and zeta potential of colloidal mixtures of amelogenin and hydroxyapatite in calcium and phosphate rich ionic milieus." *Arch. Oral Biol*. Vol. 56, 2011, 521–532.

[8] Altankov G., Richau K. Groth Th. "The role of surface zeta potential and substratum chemistry for regulation of dermal fibroblasts interaction." *Materialwissenschaft und Werkstofftechnik*. Vol. 34(12), 2004, p. 1120-1128.

[9] Frijd V., Linderback P., Wennerberg A., de Paz L.C., Svensater G., Davies J.R. "Effect of nanoporous TiO_2 coating and anodized Ca^{2+} modification of titanium surfaces on early microbial biofilm formation." *BMC Oral Health*. Vol. 11(8), 2011.

[10] Quiryen M., Bollen C.M.L., Papaioannou W., Van Eldere J., van Steenberghe D., "The influence of Titanium Abutment Surface Roughness on Plaque Accumulation and Gingivitis: Short Term Observations." *Int. J. Oral maxillofac. Implant*. Vol. 11, 1996, p. 69-178.

[11] Bellido I.S., Barbieri L., Beckett A.J., Prior I.A., Susarrey-Arce A., 4, Tiggelaar R.M., Fothergill J., Raval R., Diaz Fernandez Y.A. "Effect of local topography on cell division of *Staphylococci sp*." *Nanomaterials*. Vol. 11, 2021.

[12] Yang K., Shib J., Wang L., Chen Y., Liang C., Yang L., Wang L.N. "Bacterial anti-adhesion surface design: Surface patterning, roughness and wettability: A review." *Journal of Materials Science & Technology*. Vol. 99, 2022, p. 82-100.

7 Conclusion and Suggestions for Future Work

A potential method for enhancing the soft tissue adhesion while reducing the bacteria adhesion and biofilm formation on a dental implant is to change the surface topography of the abutment area at the nanoscale. The aim of this thesis was to investigate the relationship between cell and bacteria adhesion and surface features of laser-treated samples made of grade 2 pure titanium and Ti6Al4V alloy. Laser treatment led to groove-structured surfaces. The grooves obtained were on average 15 μm in width for both materials, observable by SEM microscopy. Following treatment, typical laser structures, known as LIPSS (laser-induced periodic surface structures), are formed on the surface. By means of FESEM microscopy, it was observed that each lamella has nano-bubbles and lamellae of one order of magnitude smaller on its surface, that characterize the surface at the nanoscale. Probably, this nano-topography plays an important role in cell and bacterial adhesion.

The average roughness values increased by an order of magnitude in treated samples compared to mirror-polished ones, although it promisingly remained below the threshold of 0.2 μm, a value above which bacterial adhesion is enhanced, as widely known from the literature. Confocal microscopy revealed that the skewness Ssk is slightly greater than 0 in both types of samples, which means that the height distribution is skewed on the mean plan and partially below it. The kurtosis value Sku is greater than 3 for TicpL and Ti64L, so peaks and valleys have a pointed shape, especially for TicpL, whose Sku is almost 7. This feature could decrease the bacteria's critical angle, reducing bacterial growth and biofilm formation, as will be discussed later in the chapter.

With regard to wettability, it was found that laser treatment increases the contact angle of both pure titanium and Ti6Al4V samples, but the values still remain in the range of hydrophilicity.

Furthermore, as resulted by XRD analysis, the crystallographic structure doesn't result altered after the treatment compared to the original one. There wasn't any shift in the martensitic zone, and in the case of both pure titanium and alloy specimens, the peaks were referable to those of alpha-titanium, as beta-titanium is usually seen after heat treatment.

The surface topography significantly affects the spreading and orientation of fibroblasts. The creation of grooves with a size comparable to that of fibroblasts induces their orientation along the grooves, a phenomenon that is not observed in untreated samples. The number of adhered cells is independent of the texture and comparable for both materials, hence the laser textured surface did not introduce any toxic elements reducing the metabolic activity of the seeded fibroblasts during the testes time-points. The orientation of fibroblasts along the grooves is critical as it would allow better growth of connective tissues on the surface [4] – [7].

With regard to bacterial adhesion of the surface, a reduction in the number of bacteria was observed, but also a reduction in biofilm aggregates, which are present in untreated samples. Bacteria on laser-treated surfaces are less organized and their ability to aggregate, and thus biofilm formation, is reduced. This phenomenon could be related to the effect of local topography on bacteria. These, in fact, especially the *staphylococci* family, tend to aggregate orthogonally to bacteria already positioned on the surface [2], forming the typical aggregations seen in the untreated samples in the *Fig. 6 – 36 A), 6 – 37 A), 6 – 38 A) and 6 – 39 A)*. Recent studies highlighted this bacteria's feature can be responsible for the bacteriostatic effect delivered by surface topography [1], [3]. Laser-treated

samples show, as seen above, periodic structures of a few micrometers in size alternating with cavities and equally large pores causing a bacteriostatic effect by decreasing the fraction of cell area f_{growth} where bacteria division and proliferation are allowed. Roughness Ra of 0.2 µm on average should also give the surface bacteriostatic properties and ensure that bacterial growth does not increase [8],[9],[10].

Future work can be performed to investigate other characteristics of this type of surface that were not covered during the course of this thesis, such as protein adhesion and the behavior of other cell groups such as osteoblasts. Furthermore, the laser treatment could be performed under different conditions.

Reference

[1] Bellido I.S., Barbieri L., Beckett A.J., Prior I.A., Susarrey-Arce A., 4, Tiggelaar R.M., Fothergill J., Raval R., Diaz Fernandez Y.A. "Effect of local topography on cell division of *Staphylococci sp*." *Nanomaterials*. Vol. 11, (2021).

[2] Monteiro, J., Fernandes, P., Vaz, F. et al. "Cell shape dynamics during the staphylococcal cell cycle." *Nature Communications*. Vol. 6, 2015, 8055.

[3] Jenkins, J., Mantell, J., Neal, C. et al. "Antibacterial effects of nanopillar surfaces are mediated by cell impedance, penetration 530 and induction of oxidative stress." *Nature Communications.* Vol. 11, 2020, 1626.

[4] Canullo L., Genova T., Trujillo E.G., Pradies G., Petrillo S., Muzzi M., Carossa S., Mussano F. "Fibroblast Interaction with Different Abutment Surfaces: In Vitro Study." *International Journals of Molecular Science*. Vol. 21, 2020, p. 1919-1937.

[5] Ferraris S., Warchomicka F., Iranshahi F., Rimondini L., Cochis A., Spriano S. "Electron beam structuring of Ti6Al4V: new insight on the material surface properties influencing the bacterial adhesion." *Materials*. Vol.13(2), 2020, p. 409-420.

[6] Teng F. Y., Ko C. L., Kuo,H. N., Hu J. J., Lin J. H., Lou C. W., Hung C. C., Wang Y. L., Cheng C. Y., Chen W. C. "A comparison of epithelial cells, fibroblasts, and osteoblasts in dental implant titanium topographies." *Bioinorganic chemistry and applications*. 2012:687291.

[7] Nevins M., Kim D.M., Jun S.H., Guze K., Schupbach P., Nevins M.L. "Histologic evidence of a connective tissue attachment to laser microgrooved abutments: a canine study." *The International Journal of Periodontics & Restorative Dentistry*. Vol. 30(3), 2010, p. 245-255.

[8] Yang K., Shib J., Wang L., Chen Y., Liang C., Yang L., Wang L.N. "Bacterial anti-adhesion surface design: Surface patterning, roughness and wettability: A review." *Journal of Materials Science & Technology*. Vol. 99, 2022, p. 82-100.

[9] Frijd V., Linderback P., Wennerberg A., de Paz L.C., Svensater G., Davies J.R. "Effect of nanoporous TiO_2 coating and anodized Ca^{2+} modification of titanium surfaces on early microbial biofilm formation." *BMC Oral Health*. Vol. 11(8), 2011.

[10] Quiryen M., Bollen C.M.L., Papaioannou W., Van Eldere J., van Steenberghe D. "The influence of Titanium Abutment Surface Roughness on Plaque Accumulation and Gingivitis: Short Term Observations." *Int. Journal of Oral & Maxillofacial Implant*. Vol. 11, 1996, p. 69-178.

8 Ringraziamenti

A conclusione della mia tesi desidero dedicare questo spazio alle persone che hanno contribuito, con il loro instancabile supporto, alla realizzazione della stessa.

Vorrei in primis ringraziare la professoressa Silvia Spriano e l'ingegner Sara Ferraris, rispettivamente relatrice e correlatrice di questo elaborato, per l'instancabile supporto che mi hanno fornito e per le conoscenze che hanno messo a mia disposizione, guidandomi con pazienza e passione in tutti gli argomenti trattati.

Ringrazio Alice Tori e Andrea Mazzalovo di Osai Automation Systems S.p.A. per aver permesso la collaborazione con l'azienda stessa e per avermi aiutata nella realizzazione del trattamento laser dandomi sempre la massima disponibilità.

Grazie ad Andrea Cochis ed a tutta la sua squadra del Biomedical Materials Lab dell'Università del Piemonte Orientale per aver eseguito le prove biologiche, ospitandomi nella loro divisione.

Un grazie particolare va a mia mamma Rosanna e a mio papà Paolo per essere sempre stati il mio punto di riferimento in ogni momento di sconforto e per avermi sempre appoggiata e sostenuta in tutte le mie scelte. Sono diventata la persona che sono oggi grazie a voi. Siete stati e sarete sempre la mia forza.

Grazie ai miei nonni Luciana, Andrea, Carolina e Angiu per tutta la dolcezza e i saggi consigli che mi avete dato, questa tesi la dedico a voi che mi avete insegnato cosa significa amare incondizionatamente senza desiderare nulla in cambio.

Grazie a tutta la mia famiglia, alle mie amiche e ai miei amici per tutti i sorrisi e le risate che ogni volta condividiamo insieme, grazie per tutto il supporto che mi avete sempre dato e per aver sempre creduto in me.

Un grazie va Stefano, per essermi stato sempre vicino anche a chilometri di distanza, per la determinazione e la tenacia che hai saputo trasmettermi. Credo che il resto tu lo sappia già.

Infine, vorrei ringraziare anche la Divisione Diabete di Medtronic e tutti i miei colleghi per avermi accolta come in una famiglia in questo nuovo viaggio.

Grazie per essere stati miei complici, ognuno a modo suo, in questo percorso universitario, che ormai è giunto al termine. Oggi sono orgogliosa di me stessa, ed un grazie lo devo anche a me, per aver sempre seguito le mie scelte con testardaggine ed energia.

Che un nuovo capitolo della mia vita abbia inizio!